Molecular Organic Materials Properties and Controlled Film Growth via Organic Vapor Jet Printing

by

Olga Shalev

A dissertation submitted in partial fulfillment
of the requirements for the degree of
Doctor of Philosophy
(Materials Science and Engineering)
in the University of Michigan
2016

Doctoral Committee:

Associate Professor Max Shtein, Chair
Professor Stephen R. Forrest
Professor Jinsang Kim
Professor Wei Lu

DEDICATION

This thesis is dedicated to my beloved grandparents, Buzya and Alexander Vaisman, who taught me to believe in myself.

ACKNOWLEDGEMENTS

Past five years have been the best time of my life so far. I would like to acknowledge people who made me feel that way. Firstly, my deepest gratitude is to my advisor, Max Shtein. Thank you for teaching me how to analyze complex scientific problems and giving me the freedom to realize new ideas. Thank you for understanding throughout these years and enabling me to combine research work and family life.

Secondly I would like to thank my laboratory coworkers for being always helpful and supportive. Despite the age difference, you made me feel comfortable and I enjoyed spending time with you inside and outside the lab. Shaurjo, we have become a true collaborators from the beginning, not only because both of us working on OVJP project, but because of sharing the same vision. Your encouragement and support helped me to overcome many difficulties. Matt, thank you for all your help, friendship and for teaching me so much. Steve, Adam, Kanika, Mark, thank you for your support from the very beginning of my PhD. Aaron, your technical and artistic talent tremendously helped in accomplishment of my projects and I am grateful for that. I would also like to thank to undergraduate students working with me throughout my PhD: Tareq, David, Nick, Chris, Doug, Samantha. Your dedication and work etiquette helped to complete all the projects I was working on.

Thirdly I would like to thank my collaborators - Professor Clarke, Yongsoo, Nancy and Christina for your work on XRD and many sleepless nights testing my samples. Professor Lu - for providing me with clear understanding of “nanolobes” phenomenon. Professor Mehta and Shreya - for all the help with biological tests. Professor Schwendeman and Max J.M. - for all the HPLC tests and your support of my ideas. Professor Amidon and Patrick, for teaching me about pharma world. Harald, thank you so much for all the glass work. I enjoyed our conversations and hopefully we will take a ride together in your Vikings boat.

Lastly and most importantly, I thank my amazing family. My husband, Michael, for being father, psychologist, guide, friend, and many other roles you fulfilled during this time. I am grateful for your unconditional love and support. Shani and Danny, you are the reason for everything I do. I try to make this world better for you.

Mom and dad, grandma and grandpa, for you it was the toughest period. I know we mean a world to you and us being across the ocean was not easy for you. Thank you for all your encouragement and help. You always said that you trust that I am doing my best, and these words accompanied me through my life.

TABLE OF CONTENTS

LIST OF TABLES

LIST OF FIGURES

ABSTRACT

This dissertation describes advances in printing small molecular organic compounds having important applications, including two with major societal impact: 1) the additive patterning of organic semiconductors, and 2) the continuous and cost-effective production of pharmaceutics.

Rapid progress in research and development of organic electronics has resulted in many exciting discoveries and applications, including OLEDs, OPVs and OTFTs. Small molecular organic optoelectronic devices are usually multilayer films and patterns comprised of sharp interfaces and highly pure materials. Solvent-based deposition and patterning methods compromise the purity and interface sharpness, calling for solvent-free methods. Vacuum thermal evaporation is a common technique used currently, with inherent limits for scale-up. Instead, organic vapor jet printing (OVJP) is proposed, to enable additive, solvent-free patterning of molecular semiconductors at scale. In OVJP, a carrier gas is used to drive collimated flow, enabling additive patterning, while preserving advantages of vacuum thermal evaporation.

For process and equipment design and scale-up, knowing the evaporation properties (e.g. sublimation enthalpy, vapor pressure) of organic semiconductors used in devices is crucial. It is also important to predict pattern and film morphology formation for a range of process conditions. To address these technology needs, we studied the thermophysical properties of small molecular organic compounds and demonstrated a new predictive relationship between material

density and sublimation enthalpy. We then applied this knowledge to simultaneously enhance patterning resolution and materials utilization, using compressible flow simulation to design new evaporation systems that achieve micrometer-scale patterning resolution.

The gas-to-solid phase transition in organic vapor jetting was studied, identifying process conditions that yield novel and unique surface morphologies, with potentially useful properties. A phase diagram was developed that predicts surface morphology as a function of molecular properties and deposition conditions. These discoveries were then used to produce films of organic compounds with enhanced dissolution kinetics, which are found to be beneficial for many medical applications. In particular, the OVJP technique is shown to break fundamental barriers for the deployment of some drug candidates by enhancing their dissolution kinetics by orders of magnitude, while enabling novel drug delivery systems, such as medicines deposited onto microneedles, patches, biodegradable polymers. Direct *in vitro* treatment of breast and ovarian cancer cell cultures in aqueous media, by tamoxifen films shows significantly improved bioavailability as compared to powders.

Chapter 1
Introduction

1.1 Background and Motivation

Conjugated molecular organic compounds have received increasing amounts of attention in the scientific and engineering communities for their applications in solar energy conversion, efficient solid-state lighting, flexible electronics, and other areas. From the earliest reports of the photovoltaic effect in organic thin films (*1, 2*) to the recent commercialization of organic light-emitting devices (OLEDs) for flat-panel displays, progress in the field of organic optoelectronics has been rapid. OLED external quantum efficiency (EQE) exceeding 20% (*3*) and luminous power efficiency of more than 100 lm/W (*4*) were shown, organic photovoltaic power conversion efficiency of over 10% (*5*) was achieved, and field-effect mobility in organic transistors was improved beyond 5 cm^2/V-s (*6*). The simultaneous development of materials and device structures enabled precise control over charge injection, transport, and recombination; exciton transport; and light in- or out-coupling. Meanwhile, to transform the organic semiconductor compounds from their initial state (typically, purified crystalline powder) into multilayered device structures over large areas, a remarkably small set of processing techniques have been deployed (mostly vacuum thermal evaporation (VTE)). A review of these techniques has been published by Biswas, Shalev and Shtein (*7*).

The focus of this thesis is on van der Waals bonded, small molecular weight (e.g., smaller than 900 g mol^{-1}) organic compounds, some of which are shown in **Fig. 1-1**. The relatively weak intermolecular forces (*8*) enable the nonepitaxial deposition (*9*) of high quality thin films on a range of substrates, including glass and flexible plastics. However, the nature of bonding in these materials typically restricts processing to nonreactive and dry techniques. For example, sputtering finds limited application due to the fragility of the organic thin films under ion bombardment, whereas use of conventional photolithography is restricted by the films high permeability by common solvents. Furthermore, solvent-based deposition methods face the difficulty of adjusting the solubility of individual components independent of their optoelectronic properties.

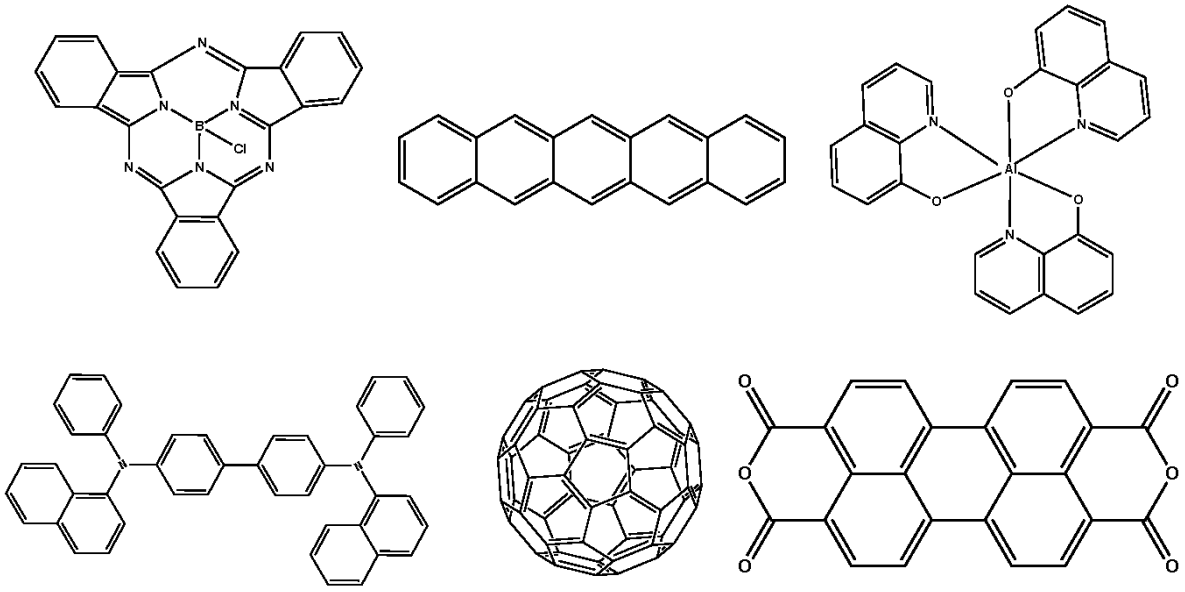

Figure 1-1 Small molecular organic semiconductor materials
Small molecular organic semiconductor materials: chemical structures of the conjugated organic and organometallic compounds of interest in optoelectronic device applications: archetypal electron- and hole-transport materials, wide bandgap hosts, dopants, electron donors, acceptors, and sensitizers.

A variety of techniques have been developed to enable the precise deposition and patterning of molecular organic thin films, geared toward device fabrication. These techniques include vacuum thermal evaporation (VTE), organic vapor phase deposition (OVPD), organic vapor jet printing (OVJP), laser-induced thermal imaging (LITI), and active-layer patterning by shadow masking and transfer methods.

Industrial application of these deposition methods brings up special engineering challenges concerning material utilization efficiency, pixel crosstalk, apparatus contamination, takt time, and many other factors, which are also relevant to the art of thin-film growth in a research setting. Of particular interest are methods that enable additive patterning of active layers involved in charge and exciton transport, light absorption or emission, and other important functions in devices. OVJP enables direct patterning of the active organic layers, and is the focus of this thesis. Briefly, an inert carrier gas (e.g., nitrogen, helium, argon, etc.) picks up organic vapor and impinges as a collimated jet onto a substrate, where the heavier organic molecules selectively condense (*10*). However, in order to realize OVJP as a fully developed manufacturing tool and to fulfill all the potential in OVJP deposition principle, a full understanding of technique physical picture a depositing materials behavior is required. This thesis attempts to address this requirement and introduces new applications fields for OVJP.

The following introduction will briefly overview small organic materials and films properties, devices comprising from these materials, and devices manufacturing techniques. Special attention will be given to OVJP system, which is the focus of this thesis. Last part of the overview includes introduction to small molecular pharmaceuticals properties and challenges in pharmaceutical industry which will be addressed in last part of thesis.

1.2 Properties of small molecular organic materials

There are four general categories of solids distinguished by the levels of bonding: ionic, covalent, metallic, and molecular (i.e. van der Waals). Organic compounds are materials that consist of carbon and hydrogen structural elements and can contain other elements such as S, N, O or metal atoms. This classification of organic materials includes polymers, hydrocarbons, alkanes, and specifically excludes materials such as C_{60} and carbon nanotubes which belong to the broader category of molecular solids (or small molecule compounds - **Fig. 1-1**). Both organic and molecular compounds exhibit aspects of both covalent- (intramolecular) and molecular- (intermolecular) bonding. An even more important subsection of molecular compounds, and the focus of major part of this thesis, is conjugated small molecule compounds, which are characterized by highly conjugated p-electron systems. These materials are of particular interest due the delocalization of the p-p electron system that results in electronic excitation energies in the range of a few eV (or visible electromagnetic spectrum).

Carbon (6 electrons) has a ground state that is $1s^2 2s^2 2p^2$. There are four electrons in the outer shell that may be mixed to form four degenerate hybrid sp^3 bonds to ligands: methane is example of this bonding scheme. Alternatively, it is possible to form three degenerate hybrid sp^2 orbitals (called the double bond); ethylene is a good example. These three orbitals (one s and three p) form coplanar chemical bonds, the fourth orbital, a p-orbital, remains unchanged and perpendicular the sp^2 plane. Because these p-orbitals overlap with neighboring atoms, an additional bond called a π-bond is formed. These electrons are delocalized above and below the plane of the molecule, creating a “sea of electrons”. Most of the physical (optical and electronic) characteristics of organic semiconductors are imparted by the nature of this π-bond. The effect of extended conjugation is demonstrated in **Fig. 1-2**.

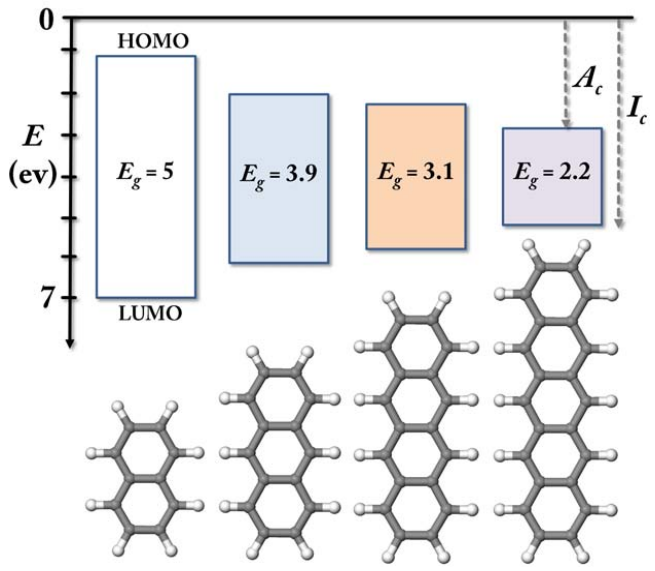

Figure 1-2 Effect of π- π conjugation on bandgap in organic materials
Band diagram of from left: naphthalene, anthracene, tetracene and pentacene with corresponding ionization potential (I_c), electron affinity (A_c) and bandgap (E_g). The important feature to note is that by extending the π- π conjugation, the bandgap decreases (*11*).

One of the main advantages of organic materials is the tunability of their optical/electronic properties through functional group substitution. Such variability is shown in **Fig. 1-3**, where the photoluminescent properties of cyclo-metalated platinum complexes can be varied across the visible spectrum. Another advantage is the lack of necessity for lattice-matching characteristic of inorganic thin film growth. This has led to speculation that organic electronics can reduce the processing costs by allowing for low-temperature processing and large-area deposition on light-weight flexible substrates such as plastic, however this cost advantage has yet to be realized.

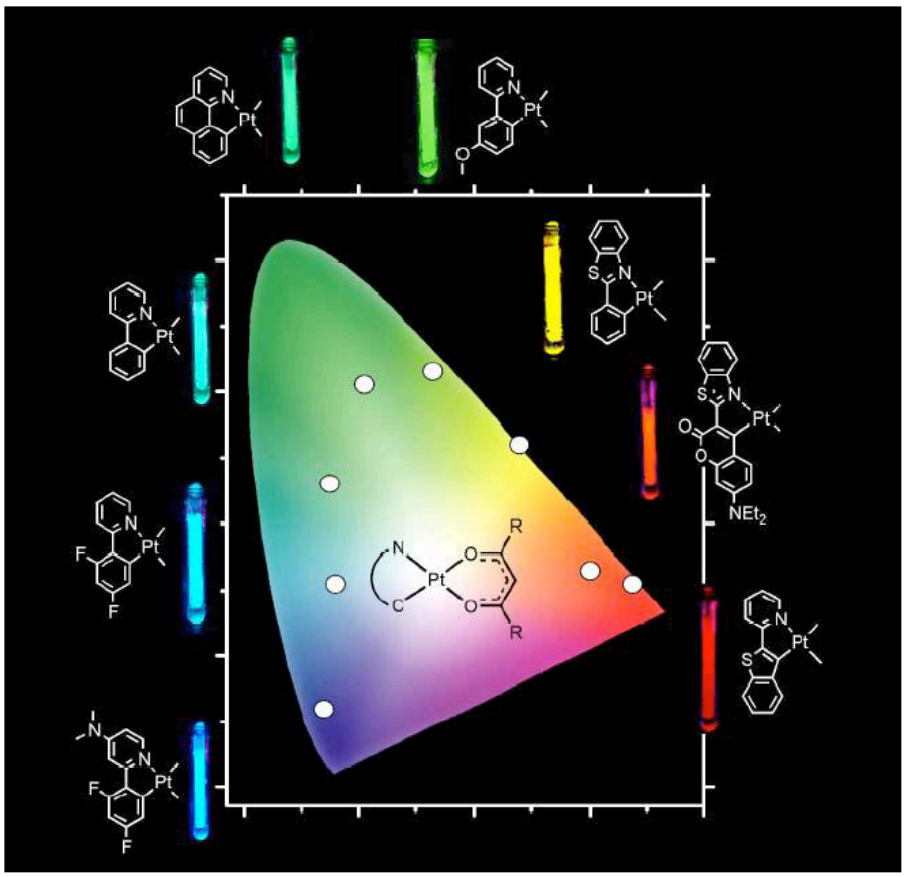

Figure 1-3 Example of emission color tuning in cyclo-metalated platinum complexes
Example of emission color tuning in cyclo-metalated platinum complexes via functional group substitutions. Reproduced from (***12***).

To guide the design of deposition apparatus, establish adequate process control, and estimate fundamental limits of production throughput and fabrication energy budget, particularly for commercial-scale fabrication of organic-based devices, evaporation properties of the compounds should be known or predictable. Since small molecular conjugated organic materials exhibit van der Waals bonding in the condensed state, these materials are stable up to relatively high temperatures (e.g., copper phthalocyanine is stable in air above 350 °C). Following the synthesis of the compounds and prior to depositing thin films for devices, the materials are usually purified by using a combination of crystallization precipitation out of solution, column purification, and vacuum-train sublimation (*13*). To obtain device-quality thin films with precisely controlled

thickness (down to <1 nm), the starting materials must be either thermally evaporated or precipitated out of a solvent while process conditions are carefully controlled (e.g., in spin-coating, concentration, temperature, and substrate rotation speed must be controlled). To minimize the incorporation of unintentional stoichiometric/electronic defects during processing, stringent solvent purification and/or vacuum maintenance must be observed. The evaporation temperature window for conjugated polyaromatic compounds (with molecular weight typically ranging between 200 and 900 g mol^{-1}) is framed by the need to achieve sufficiently high evaporation rates to meet production throughput requirements and the need to avoid thermal degradation.

The evaporation temperature is also set by considerations of desired film morphology—faster deposition rates (and colder substrate) generally lead to amorphous deposits, whereas slower deposition rates (and warmer substrate) generally increase intermolecular ordering in the films (*14, 15*), which is potentially advantageous in optimizing charge and exciton transport.

In contrast to traditional hydrocarbons encountered in fossil-fuel refining, the thermodynamic properties of polyaromatic compounds comprising the class of organic semiconductor materials are less well known.

1.3 Small Molecular Organic Semiconductor Devices

Interest in organic electronics stems from a combination of intriguing electronic and optical properties of the materials, coupled with the ability to deposit organic films on a variety of low-cost substrates, such as glass, plastic, or metal foils, as mentioned in the introduction. OLEDs for flat-panel, information-display applications have enjoyed the most rapid improvements (*16*), propelled by the value-added nature of the application, for which the rich color gamut and energy efficiency afforded by organic emitters are highly desirable. High-efficiency, very bright and

colorful thin displays based on OLEDs are in commercial production by several manufacturers. Advances in organic electroluminescence for display applications are paving the way for OLED-based solid-state lighting, where the new technology must compete with multiple established paradigms (e.g., incandescent, fluorescent, and inorganic LED-based lighting).

Significant progress is also being made in the realization of organic thin-film transistors (OTFTs) (*17*) and thin-film organic photovoltaic cells (OPVs) (*18*) for cost-effective and ubiquitous electronics and solar electricity generation. The cost of semiconductor layers used in most thin-film solar cells is low, therefore the ultimate success of organic semiconductors in these applications depends on leveraging the ability to integrate devices on inexpensive, large-area substrates using very low-cost, low-energy-intensity (*19*), high-throughput production techniques. To provide context for the discussion of OLED, OTFT, and OPV device-fabrication methods, the structure, operating principles, and performance characteristics of the devices themselves are briefly discussed below.

1.3.1 Organic Light-Emitting Devices

Although basic electroluminescence in an organic compound was demonstrated as early as 1953 (*20*) and 1965 (*21*), it wasn't until Tang & VanSlyke's (*22*) 1987 demonstration of the first heterojunction OLED that the science and technology of OLEDs began to gain momentum. High efficiency, archetypal heterojunction OLEDs (*22, 23*) typically comprise organic layers sandwiched between two thin film electrodes, as shown in **Fig. 1-4**. Electrons and holes injected under electrical bias from the cathode and anode, respectively, undergo drift diffusion through the respective transport layers and recombine at the interface, emitting heat and light. To first order, the thicknesses and composition of the individual layers dictate the amount of injected charge for a given voltage as well as the overall efficiency of the OLED. The color of emitted

light is controlled primarily by choosing an appropriate HOMO-LUMO energy gap of the dopant molecules placed at the interface between the electron- and hole-transporting layers. Confinement of excited states (excitons) is a key consideration, accomplished through the use of large-energy-gap, exciton-blocking layers that can increase the probability of radiative recombination of excitons away from the quenching electrodes.

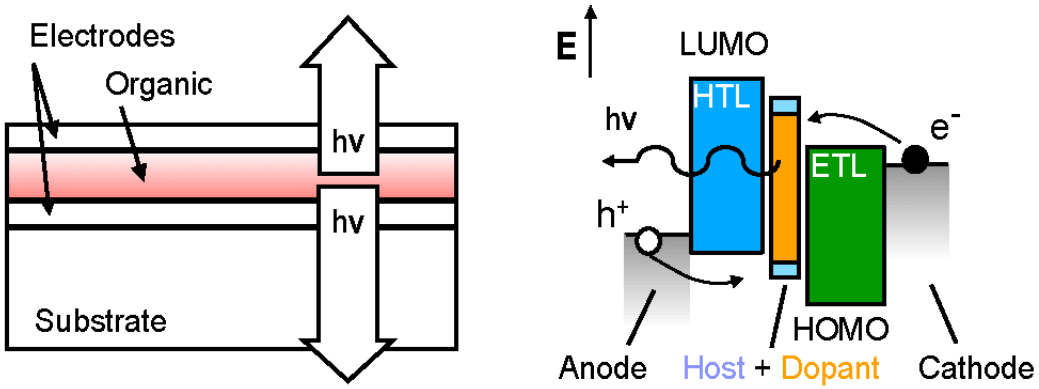

Figure 1-4 Schematic of an organic light-emitting device (OLED) structure
Schematic of an organic light-emitting device (OLED) structure, showing organic layers sandwiched between two electrodes, at least one of which is transparent. Also shown is an energy-level diagram for a device consisting of anode, hole- and electron- transport layers (HTL and ETL), doped emissive layer (i.e., consisting of two or more components), and cathode. Holes and electrons are injected and recombine in the emissive layer. Interfaces and doping are important in this structure for balancing current injection, localizing recombination, and increasing emission efficiency. (*7*)

Two primary architectures have emerged for realizing full-color information displays based on OLEDs. In one approach, the basic RGB pixel triad (or pentile pattern) is achieved by patterning the red-, green-, and blue-emitting OLEDs side by side, which requires at the very least the in-plane patterning of each emitter with edge definition on the order of 20 micrometers or better, depending on the type of display. In another approach, the OLED component takes the place of a conventional backlight coupled with switched liquid crystal-based red, green, and blue filters. In the latter configuration, the patterning requirements for the organic emitters can be relaxed,

although the energy efficiency and color gamut are in principle inferior to the first approach. In either case, the active organic layers are usually deposited by VTE, and pixilation is achieved by using a shadow mask. It has emerged that shadow masking severely limits the scalability of OLEDs, increasing the urgency for low-cost, scalable, direct patterning, which is covered in a subsequent section.

1.3.2 Organic Photovoltaic Cells

As an intrinsically large-area and cost-driven application, solar cells benefit from the strong light absorption of organic dyes and the ability to rapidly deposit device-quality organic semiconductor thin films at ambient conditions on a variety of substrates without the need for lattice matching. The photovoltaic effect in organic films was observed as early as 1958 (*1*) and was followed by reports on Schottky junction-based organic photovoltaics (*24*). The efficiency of these early devices was extremely low, in part due to suboptimal absorption and the inability to dissociate strongly bound electron-hole pairs by the weak built-in field of Schottky junctions. A breakthrough by Ching Tang (*2*) was to design a heterojunction, in which two different organic materials were used to create a functional analog to the classical semiconductor p-n junction. To address an inherent tradeoff between light absorption and exciton diffusion in organic thin films, bulk heterojunction architectures were developed (*25*). Currently, the power conversion efficiency of organic solar cells exceeds 11%, and several efforts worldwide are directed toward scale-up and commercialization for a range of applications where flexibility and light weight are advantageous (*26*). Compared with many other (inorganic) solar cell technologies, organic based PV cells potentially offer some of the shortest energy payback times (*19*). However, in order to reduce solar photovoltaic module installation costs, efficiency must be maximized, and the methods used for large-scale production of solar cells must result in stable,

efficient device structures. Nearly identical to the structure of heterojunction OLEDs, a typical heterojunction OPV cell consists of organic thin films sandwiched between two electrodes, one of which is transparent. Typically, the substrate is glass or plastic, precoated with a transparent conducting metal-oxide anode or thin conductive metal, and the cathode is a thick metal reflective layer. The thin (<200-nm) active organic layer comprises at least two materials with different LUMO (and/or HOMO) energy levels, which form a planar or inter-digitated heterojunction. As noted above, light absorbed in these layers forms excitons, which diffuse randomly inside the organic layers. Parasitic quenching of excitons can occur in the bulk, at the electrodes, and by energy transfer to other moieties inside the material. Upon encountering the donor- acceptor heterojunction, excitons can dissociate into interfacially bound polaron pair states, which precede the generation of more spatially separated electrons and holes that can be subsequently collected at the electrodes (**Fig. 1-5**). Increased molecular order affects the thermodynamics and kinetics of these processes and can thereby improve energy and charge transport considerably, which boosts the overall power conversion efficiency (*27-29*).

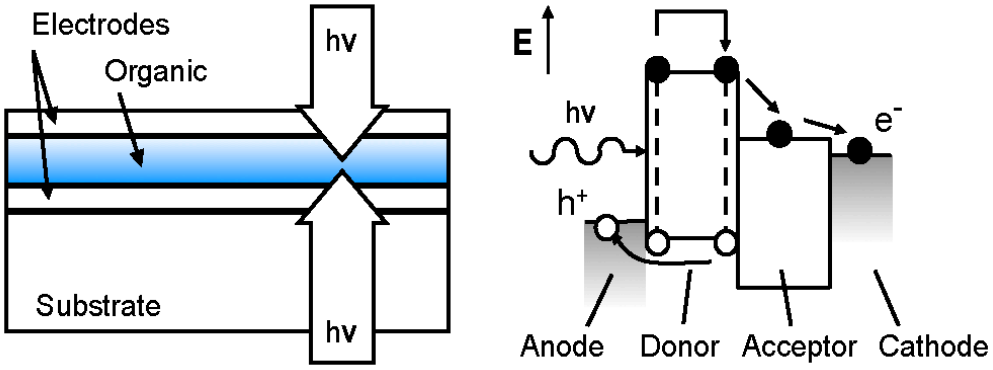

Figure 1-5 Schematic of an organic photovoltaic (OPV) cell structure
Schematic of an organic photovoltaic (OPV) cell structure. Absorption of photons generates bound excited states (excitons), which upon diffusion to the donor-acceptor interface dissociate into electrons and holes. The light-absorbing layers are often structured to contain partially mixed donor and acceptor components, which are phase separated and crystalline at the nanoscale. (*7*)

1.3.3 Organic Thin-Film Transistors

Field-effect/thin-film transistors (FETs and TFTs) are the foundational elements of integrated circuits used in computing and information display, where millions of transistors are needed to enable pixel switching across the entire display area. Most transistors are made of single-crystal, polycrystalline, or amorphous silicon. Metal oxides have gained market share recently in display applications; however, OTFTs have attracted considerable attention in the past decade owing to the potential to realize large-area, mechanically flexible, lightweight devices, as well as to reduce the cost of materials and processing over large areas on glass and plastic substrates at room temperature. Over time, organic compounds have been developed with field-effect charge mobilities comparable with or higher than those of amorphous silicon TFTs (e.g., 1-10 cm^2/V-s), enabled by improvements in molecular structure and film morphology control that reduce degradation and act to maximize electronic coupling between the π electron systems of adjacent molecules (*30*).

Examples of OTFT configurations are shown in **Fig. 1-6**; the top-contact/bottom gate architecture is the most commonly used in research. The source and gate electrodes are biased (VDS & VG) relative to the drain. The charges, electrons or holes, are injected from the source and accumulate in the organic layer adjacent to the gate dielectric, forming a conducting path. Many organic materials, both small molecular and polymeric, have been used as channel materials for OTFTs (*30-32*). Pentacene is one widely explored material, which exhibited a relatively high field-effect hole mobility in the early years of OTFT work.

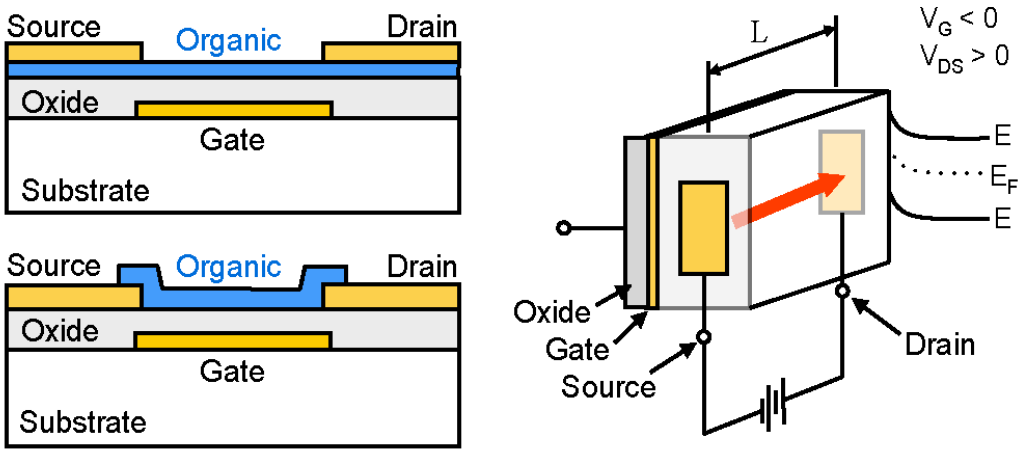

Figure 1-6 Schematic of an organic thin-film transistor (OTFT)
Schematic of an organic thin-film transistor (OTFT) with top-electrode and bottom-electrode configurations. On the right is an energy-level diagram showing band bending as a result of applied gate bias, which causes hole or electron accumulation (or depletion) in the region of the semiconductor adjacent to the gate oxide. Bias on the source and drain electrodes causes electrical current (red arrow) to flow between source and drain, in the semiconductor region adjacent to the gate oxide. (*7*)

1.3.4 Other Organic Electronic Devices

Organic semiconductor lasers:

A number of reviews have been published on lasing in organic semiconductors (*33-35*), although electrically pumped lasing has not been achieved. Optically pumped lasing has steadily gained in efficiency (*33*); state-of-the-art distributed feedback polymer lasers operate with lasing thresholds as low as 3.6 W/cm^2, which allows pumping with cheap inorganic diode lasers or even commercially available LEDs. Recent work has exploited the large, two-photon absorption cross-section of polymers to demonstrate nonlinear pumping of a blue-wavelength laser. This may mark a path to the pumping of blue lasers with low-cost red diode lasers to create hybrid, electrically pumped polymer lasers. The replacement of expensive, bulky laser pump sources with small, solid-state diode lasers, which are commercially available and extremely cheap,

holds the promise of compact, cheap, organic sources operating at visible wavelengths. Applications, however, still require further reductions in lasing thresholds as well as the demonstration of longer lifetimes and continuous-wave operation before widespread deployment becomes possible.

Organic photodetectors:

Key parameters for photodetectors include efficiency and speed of response. Organic photodetectors based on standard organic materials can sense light in the visible, infrared, and even X-ray portions of the electromagnetic spectrum and can operate well into the megahertz regime (*36, 37*), with the speed being limited by the size of the device, the lifetime and transport rate of excitons, and the charge carrier mobility. Organic photodetectors are well suited to applications requiring large-area and nonplanar devices, including X-ray imagers for biomedical applications (*38*) and human-eye-mimicking vision systems (*39, 40*). Miniaturization of organic photodetectors (e.g., by placing them directly on the cantilever of a near-field scanning microscope (*41*)) can open new applications in materials characterization and metrology. The low-cost nature of organics also allows them to be used for disposable on-chip sensors (*14, 15, 42*) or data communications, and their chemical tunability allows tunable photo-action spectra to be obtained, which may be useful in colorimetry (*43*).

1.4 Deposition Techniques

As noted above, device performance requirements and fundamental materials properties dictate the deposition methods, which must be capable of producing multilayered thin films, with layer thicknesses defined with subnanometer precision. Degradation of materials must be minimized by processing in an inert environment. Ionization of impurities in organic semiconductor devices is much more limited than in their inorganic analogs, and it can be difficult to ascertain precisely

the total concentration of dopants in these materials.

The deposition rate should be fast enough to minimize the incorporation of dust and impurities in the growth ambient but slow enough (e.g., <1 nm/s) to allow for precise control over layer thickness and stoichiometry when the layers are doped. (Commercial device fabrication calls for short takt times and consequently may require considerably faster film growth rates than deposition for laboratory-scale research.) OLEDs typically tolerate (and indeed can benefit from) amorphous films, stacked with sharply defined interfaces to help control the injection and recombination of charge, to localize excitons and facilitate light extraction. Efficient photovoltaic cells have been demonstrated with sharp, blended, and interdigitated interfaces (*2, 28, 44-46*) that maximize the electron donor-acceptor interfacial area to counteract the typical exciton-diffusion bottleneck in organic materials. The light-absorbing layers in OPV cells also support charge transport and are often processed to achieve nanoscale crystallinity by slow deposition (e.g., <0.1 nm/s) or post deposition annealing. With the basic considerations outlined above, the most common methods of small molecular thin-film growth are reviewed below.

1.4.1 Organic Molecular Beam Deposition

Organic molecular beam deposition (OMBD), comprehensively reviewed by Forrest (*9*), was derived from conventional solid-source molecular beam epitaxy, wherein the material to be deposited is placed into Knudsen effusion cells, baked, and subsequently deposited in an ultra-high-vacuum ($<10^{-10}$ Torr) chamber at relatively slow rates (e.g., <0.1 nm/s). The schematic of the OMBD technique is shown in **Fig. 1-7**. The evaporated molecules adsorb onto the substrate through van der Waals forces and can sustain quasiepitaxial growth for several monolayers, after which strain relaxation results in pronounced stacking defects. The very pure growth environment permits controlled studies of the role of dopants (*47*), properties of heterogeneous

organic-inorganic interfaces (*9, 48*), interfacial bonding (*49-51*), and surface energetics (*52, 53*). Due to the considerable capital expense and process intricacy, OMBD has remained a relatively specialized technique geared toward fundamental science, where materials purity and interface cleanliness are paramount. A simpler variant, VTE, became more common for device fabrication and material development.

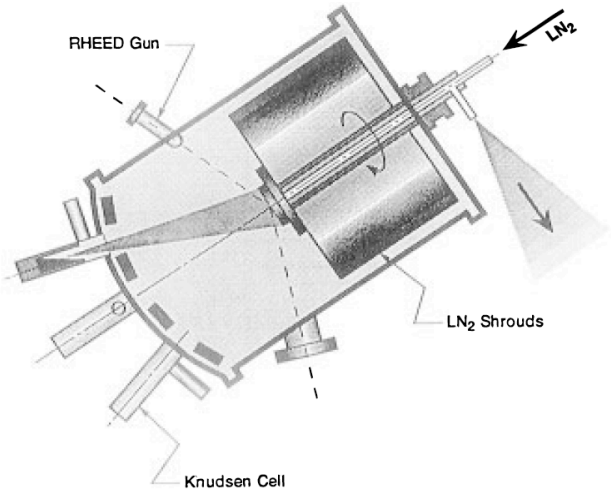

Figure 1-7 Schematic of organic molecular beam deposition apparatus
Simplified schematic of organic molecular beam deposition apparatus. (*9*)

1.4.2 Vacuum Thermal Evaporation

VTE is similar to OMBD but relaxes the vacuum requirements to ~10^{-7} Torr, where the molecular mean free path, λ, is on the order of 100 m (modulated by the size of the evaporant molecule). Resistively heated evaporation containers are used (**Fig. 1-8**), which permits the deposition of organic compounds, nonrefractory metals, and some inorganic compounds in a line-of-sight fashion. The film deposition rate, r_{dep}, is linear with the source material vaporization (sublimation) rate, r_v, which itself is exponential with temperature:

$$r_{dep} = \eta \cdot r_v = \eta_{mu} \cdot A \cdot \exp(-\Delta H^{vap} / R \cdot T) \quad (1.1)$$

where η_{mu} is the material utilization efficiency, A is a material- and apparatus-specific

coefficient, *ΔHvap* is the vaporization enthalpy, *R* is the ideal gas constant, and *T* is the source-material temperature. In the simplest case of a noncollimated, point-like evaporation source, film deposition rate, and hence the deposited film thickness, at any point on the substrate has a cosine squared shape:

$$h = H \cdot \cos^2 \theta \quad (1.2)$$

as illustrated in **Fig. 1-8**.

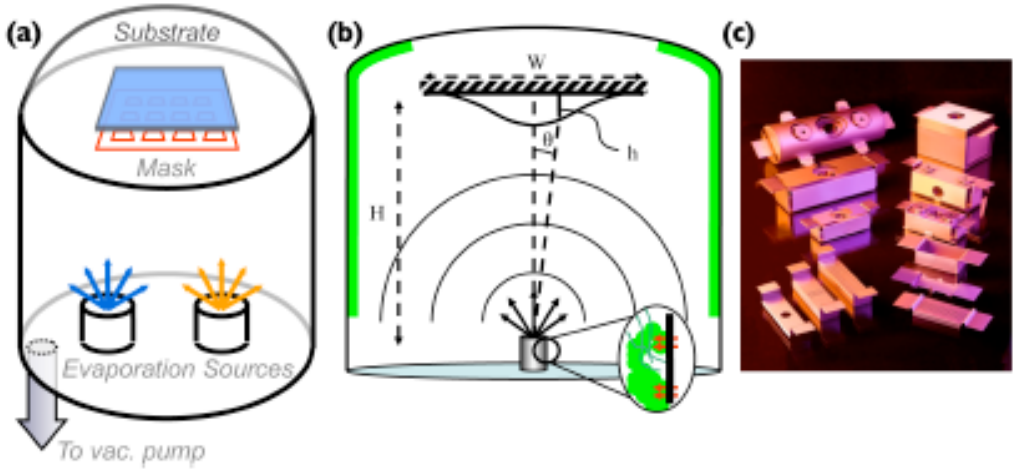

Figure 1-8 Vacuum thermal evaporation (VTE)
Vacuum thermal evaporation: (a) Simplified schematic of a vacuum thermal evaporation (VTE) chamber, shown with two sources and a shadow mask. Coevaporation of the materials permits doping with reliable control over stoichiometry down to 0.1% concentration levels. (b) An illustration of film nonuniformity inherent in point-source deposition, as well as unevenness of heating inside the evaporation source due to the poor thermal conductivity of crystalline organic powders. (c) Typical evaporation containers used in VTE. Note that industrial applications typically entail larger, linear or multiple point-sources designed to achieve uniform deposition of >1-m-wide substrates. (*7*)

Thus, to achieve a thickness variation smaller than a fraction *f* over a span of substrate *b*, the throw (distance from source to substrate) *H* should be $H \geq b/f$. Practically, longer throws result in substantially increased pumping requirements (because chamber volume scales roughly as H^3), while leaks and outflaming scale as H^m with $1 \leq m \leq 2$. To mitigate the trade-off between thickness uniformity and pumping costs, one can arrange a series of point sources (**Fig. 1-8c**)

such that the $cos^2\theta$ profiles from each one overlap, leading to a flatter deposit. From Eq. 1.1, it is also clear that achieving tight control over dopant concentration in VTE requires very close control over the evaporation source temperature, because a minute deviation in temperature from set-point of either of the sources can result in a large swing in the deposition rate and, hence, the deposited host-to-dopant ratio.

As indicated in **Fig. 1-8b** (inset), non-uniform packing of the source material in the evaporation container can lead to fluctuations in the evaporation rate. The thermal conductivity of purified organic powder is low (*54, 55*), such that evaporation is fastest at the hot container wall. Non-uniform heat and material distribution work to create empty pockets that collapse and can potentially perturb the evaporation rate. Finally, to accelerate deposition, source temperature must be increased; however, for a given source-to substrate area ratio, an intrinsic limit to the deposition rate arises due to the limited thermal stability of the organic compounds (typically, <500◦C).

1.4.3 Organic Vapor Phase Deposition

OVPD was developed to address some of the limitations of VTE. Based on hydride vapor phase epitaxy, OVPD proceeds by thermally evaporating source material into a carrier gas that transports it toward a cooled substrate, where the organic material selectively condenses. With appropriate temperature and flow profiles (*56*), material utilization efficiency can exceed 40% - orders of magnitude greater than that for typical VTE, especially in laboratory-scale apparatus. Two in- depth studies of the transport mechanisms governing OVPD have been published (*56, 57*); here, a brief discussion suffices to contextualize the additive patterning method of OVJP.

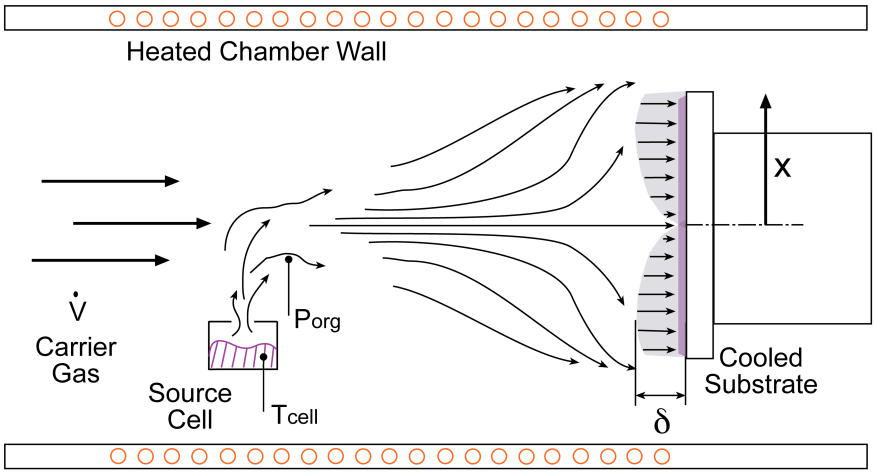

Figure 1-9 Illustration of organic vapor phase deposition (OVPD)
Illustration of organic vapor phase deposition (OVPD), where organic source material is evaporated into a stream of hot carrier gas. The vapor and carrier gas flow toward a cooled substrate, where selective condensation of organic material occurs (*56*).

Flow and boundary-layer uniformity contribute to growth of films of uniform thickness across the substrate; δ denotes the boundary-layer thickness (*56*). By separating the evaporation, transport, and deposition processes in space (**Fig. 1-9**), OVPD improves control over the deposition rate and coating uniformity. The rate at which organic vapor is extracted from the source is proportional to the vapor pressure, which is still exponential with temperature via the Clausius-Clapeyron equation. However, a self-contained evaporation source can comprise a larger thermal mass and allows for the grouping of several materials with similar vapor pressures into fewer heating zones or furnaces, whereas the hot carrier gas can flow through the packed bed of organic source material- factors that minimize spatial and temporal temperature fluctuations within the organic powder. Make-up flow can be used to dilute the vapor as needed; to reduce counter- diffusion of organic molecules upstream, toward the sources; and to help shape the distribution of the material over the substrate. Maintaining the flow path and deposition chamber at temperatures above the condensation point of the organic material nearly

eliminates parasitic condensation on the deposition chamber walls, which dramatically improves apparatus cleanliness and reduces downtime for cleaning. Reduced material buildup on the chamber walls and continuous flow of carrier gas help reduce dust accumulation on the substrate. Typical operating temperatures range from 200◦ C to 500◦ C, mass flow rates are 10-1,000 sccm, and pressures are in the range of 0.1-10 Torr (corresponding to $100 < \lambda < 1\mu m$). Continuum-based (i.e., Navier-Stokes) models of transport are valid (*56*), except for patterning, as discussed later. The low pressure limit arises from the need to generate sufficient flux of carrier gas molecules to transport organic vapor at a rate that overcomes transport by random diffusion and thermal convection (i.e., to ensure Péclet numbers >10), and the high limit arises from the need to maintain sufficiently low pressures near the substrate to maximize diffusion-limited condensation. Typical Reynolds numbers are <100, well below the turbulent threshold, although momentum transfer due to free diffusion between flow lamina can be substantial. Carrier flow around the cooled substrate gives rise to hydrodynamic and thermal boundary layers. The cold-substrate boundary condition means that organic vapor concentration falls to zero near the substrate surface, which gives rise to a concentration boundary layer as well. Film deposition occurs by diffusion of material across this boundary layer. The flow pattern can be engineered to achieve uniform distribution of the vapor above the substrate, in turn achieving uniform film thickness. In this fashion, film thickness uniformity is decoupled from the geometry of the source.

Analysis of the physical processes governing evaporation, transport, and deposition shows that the net rate of film deposition can be expressed by

$$\frac{r_{dep,i}}{A_{sub}} = J_i = \eta_{dep} \cdot \frac{D_i}{\delta} \frac{P_{0,i} \exp\left(\frac{-\Delta H_i^{vap}}{RT_{cell}}\right)}{\left(\frac{\sqrt{2\pi Mw_i RT_{cell,i}}}{\alpha_i \cdot A_{org,i} + \frac{RT_{std}}{\dot{V}_{i,sccm}} \times \frac{P_{cell,i}}{P_{std}}}\right) \times \left(\Sigma \dot{V} + \dot{V}_{dil}\right)} \quad (1.3)$$

where $r_{dep,i}$ is the deposition rate (usually expressed in units of film thickness per unit time); A_{sub} is the substrate area; and η_{dep} is the deposition efficiency, which depends on the gas distributor design and the resulting flow pattern around the substrate. The variables (indexed by each component, *i*, being deposited) are as follows: η_{dep} is deposition efficiency (subject to the flow pattern and apparatus geometry), D_i is organic vapor diffusivity of molecule *i* in the carrier gas, δ is boundary-layer thickness, $P_{0,i} \exp\left(\frac{-\Delta H_i^{vap}}{RT_{cell}}\right)$ is equilibrium organic vapor pressure, Mw_i is molecular weight of *i*, T_{cell} is evaporation cell temperature, $A_{org,i}$ is surface area of the evaporating material *i,* T_{std} is standard temperature, R is universal gas constant, $V_{i,sccm}$ is volumetric flowrate in sccm of the carrier gas, V_{dil} is volumetric flow rate of the diluting make-up flow, $P_{cell,i}$ is the total pressure inside the evaporation cell of component *i,* and P_{std} is standard pressure. To predict the deposition rate for a given reactor geometry, the flow equations must be solved to provide information about δ, whereas more precise values for D_i can be either obtained experimentally or estimated from correlations such as the Chapman-Enskog equation (*58-60*). The relationship between process parameters and deposition rate embodied by Eq. 1.3 was shown experimentally to be valid (*61*) and also forms the foundation for OVJP, described later. Note also that flash evaporation (*62*) and related methods (*63*) have been demonstrated. In these techniques, the material to be deposited is fed into a flash evaporation chamber, where solid-to-vapor conversion is nearly instantaneous. The vapor exits the elongated evaporation chamber in

the form of a uniform sheet of material directed at a substrate moving perpendicular to the flux. Kodak claimed material utilization efficiency in excess of 50%, although this number is likely to be reduced substantially when patterning (by shadow masking) is taken into account (*64*).

1.5 Patterning of small molecular semiconducting devices

The above descriptions of VTE and OVPD assume that the objective is uniform deposition of thin films over the entire substrate area. Both techniques allow for nanometer scale control over film thickness, although OVPD generally offers better control over film composition. Commercial production of devices most often requires the in-plane patterning of electronically active features, which is an essential consideration in the development of organic thin-film deposition technology. Because organic semiconductors are typically van der Waals bonded in the thin films, they are not easily amenable to conventional photolithography-based film patterning approaches.

1.5.1 Vacuum Thermal Evaporation and Shadow Masking

In conventional VTE, organic thin films are typically patterned by depositing through a shadow mask, a thin stencil placed in (near) contact with the substrate during deposition. For a mask aperture with straight walls and thickness, t, and using a source of width, l, centered on the aperture axis, the shape of the deposit is approximately trapezoidal, with the width of the edge taper and, hence, the resolution limit, ρ, approximated by

$$\rho \approx (s + 2t)l / 2h \quad (1.4)$$

here, s is the mask-substrate separation, and h is the source-to-mask distance, as defined in Fig. 1-10.

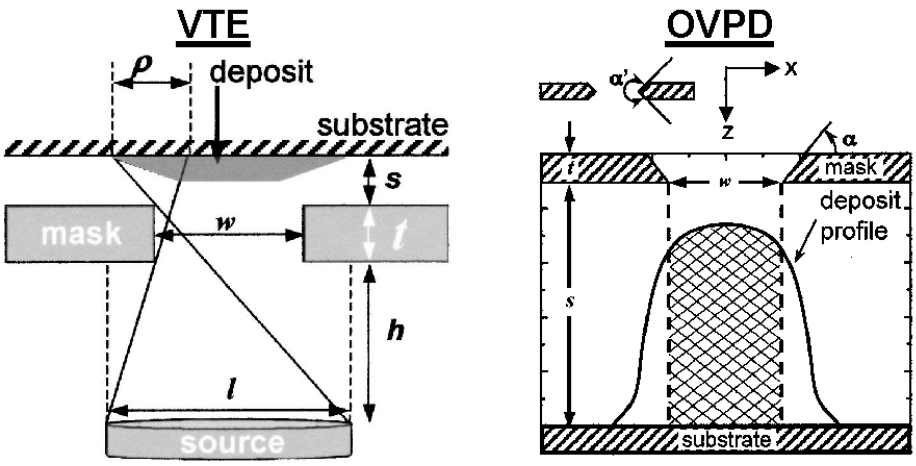

Figure 1-10 Schematic of pattern formation by shadow masking in VTE and OVPD
Schematic of pattern formation by shadow masking in vacuum thermal evaporation (VTE) (left) and OVPD (right). The deposit shapes are slightly different for the two methods; VTE typically results in trapezoidal profiles, and OVPD yields bell-shaped profiles, due to molecular collisions in the vapor phase above the substrate and in the aperture gap. (*65*)

The design guidelines suggested by Eq. 1.4 are intuitive: the mask should be as thin as possible, and s should be small, to produce the sharpest edges. However, the mask also should not bend under its own weight, and it should withstand multiple mount-remount and cleaning cycles. Thus, practical mask dimensions represent a compromise between the pattern resolution and hardware robustness requirements, with typical values for *s*, *t*, and aperture width of approximately 10 μm, 70 μm, and 100 μm, respectively. In research- laboratory-scale apparatus, the typical source diameter is $l \approx 1$ cm, and source-tosubstrate distance is $h \approx 50$ cm, which yields $\rho \approx 2$ μm, which is adequate for full-color OLED displays. Note, however, that dimensional run-out owing to thermal expansion is a critical consideration for large-area patterning. The aperture profile can be designed with a bevel or double lip, such that the edge is thin despite the rest of the mask being thick for mechanical robustness, as shown in **Fig. 1-10**. In some instances, it may be advantageous to integrate the mask with the substrate, as demonstrated

by several researchers (*66, 67*), or even to exploit the parallax owing to the gap between mask and substrate to control the placement of the evaporated components (*68*).

1.5.2 Organic Vapor Phase Deposition and Shadow Masking

Shtein et al. (*65*) studied shadow masking in combination with OVPD to pattern active organic layers. Depending on the process pressure, the molecular mean free path can be short enough (i.e., 1-1,000 micrometers) to cause numerous collisions in the vicinity of the mask and, indeed, in the space between the mask and the substrate. In this regime, where the Knudsen number (*Kn*) is $0.1 < Kn < 10$, the edge dispersion of the patterned deposit is expected to be larger and of a different shape than that in VTE, and the walls of the aperture itself are expected to be coated as well, as shown in **Fig. 1-10**. Defining a pixel shape factor as the ratio of aperture width, *w*, to the total deposit width, Shtein et al. (*65*) studied the effects of deposition pressure, mask-substrate separation, mask thickness, and aperture shape on pattern resolution. The best shape factors were seen for tapered apertures (narrowest near the substrate) that were in contact with the substrate. Higher pressures resulted in more diffuse pattern edges, as well as more parasitic coating of the aperture walls. To address the issue of parasitic coating of the mask walls, the mask can be heated (*65*), but as noted above, simple heating of the mask could result in undesired transfer of heat to the substrate, which could potentially reduce the molecular sticking coefficient or evaporate the deposited layers. Instead of relying on diffusion through apertures to form the patterns, vapor jets could be used (*10, 65*). The method of OVJP for efficient, rapid, additive patterning of organic active and passive layers is discussed below in Organic Vapor Jet Printing.

1.5.3 Molecular Jet Printing

Integration of the shadow mask with the evaporation sources has been shown in the form of

molecular jet printing (MoJet), which enables direct evaporative patterning of low-molecular-weight organics and metals at high resolution (*69*). In principle, the technique combines the advantages of the film purity of thermally evaporated films with the speed of direct patterning, leveraging the precision and scalability of microelectromechanical system (MEMS) technology for the actively controlled apertures. Deposition of active organic devices (e.g., OLEDs and OFETs) has been shown with pattern definition on the order of 5 μm (*70*). A MoJet printing system is schematically shown in **Fig. 1-11**.

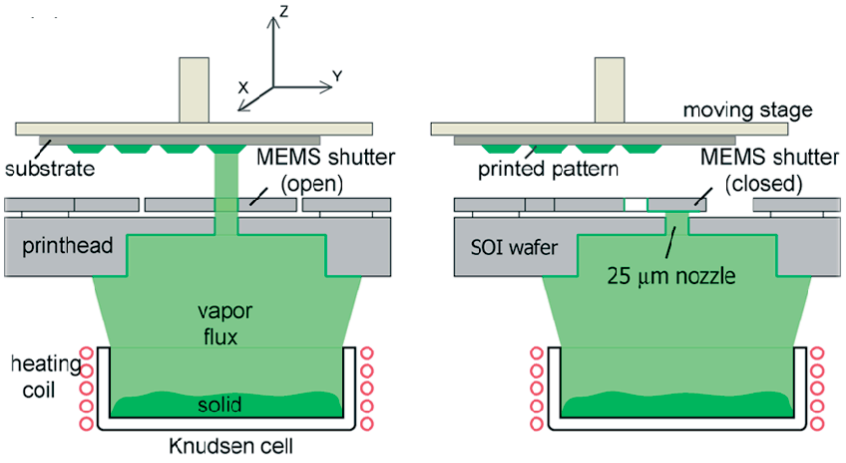

Figure 1-11 Illustration of the molecular jet printing apparatus and process (*70*)

The entire printing system is housed inside a vacuum chamber at a base pressure of 10^{-7} Torr, with the substrate mounted on a precision motion stage above the printhead. The printhead is composed of a membrane aperture (nozzle) and an integrated combdrive- actuated microshutter, which modulates the flux of evaporated materials through the nozzle (*69*). The Knudsen cell is used to generate evaporated material flux from underneath the print- head. The materials to be deposited are loaded in an aluminum or quartz crucible and heated above the sublimation/boiling temperatures. The printing system operates as a single-nozzle printer. The technique is reconfigurable for digital fabrication of arbitrary patterns with multiple material sets and is

potentially scalable to coating large area substrates. The printed pixel size and profile are strongly dependent on the geometry of the printer system and follow geometric considerations similar to those of shadow masking in VTE (*70, 71*), with pattern resolution given by

$$\rho = (s+t)(D-w)/2h + s(D+w)/[2(h+t)] \quad (1.5)$$

Courcimault & Allen (*72*) reported a microelectromechanical system (MEMS)- based masking system, integrated with the substrate for submicrometer patterning of metal contacts, which achieved patterning, for example, of metal lines 1.1 μm by 10 μm, spaced by 0.3 μm. They also reported a self-aligned masking configuration in which a sequence of processing steps (photoresist + mobile mask + laser ablation) resulted in a tapered mask directly on the substrate. Deposition of metal through this mask, followed by liftoff, can result in a high-resolution patterned metal contact. This approach, however, is likely suboptimal for patterning active organic films, or even metal contacts directly onto the organic film, because liftoff requires the use of a solvent bath that could dissolve the organic layers.

A desirable feature of MoJet is the ability to additively pattern high-melting temperature metals to form contacts. However, the MEMS printhead is hot, requiring baffles that can reduce material utilization efficiency, and is susceptible to clogging after prolonged use due to accumulation of a thick film of material on the backside of the shutter and aperture.

1.5.4 Inkjet Printing and Laser-Induced Thermal Imaging

Processing of polymer-based organic semiconductors most often entails the use of solvents, because the polymeric semiconductors are typically more soluble than small molecular semiconductors in common process solvents. Traditionally, uniform application across the entire substrate by spin-on or spray-on methods was employed, but it required additional and relatively costly steps to pattern electronically active layers. This shortcoming was addressed by inkjet

printing (*73, 74*). Note, however, that due to droplet drying energetics and dynamics, microscale features must be prepatterned on the substrate to generate individual wells that maintain a flat pixel profile upon drying (*75, 76*). Commercial use of inkjet printing has so far been successful in depositing transistor channels, and to a more limited extent OLEDs, in part due to the efficiency limitations of polymeric emitters relative to the small molecular electrophosphorescent and fluorescent compounds.

Additional methods for active-layer patterning include a variety of stamping/transfer techniques (*77-81*) and LITI (*82*). In LITI, a donor substrate is first coated with the material to be deposited. The donor substrate is then brought into physical contact with the receiver substrate and is illuminated by a short, powerful laser pulse from the back, which causes the transfer of material. High-resolution OLEDs and OTFTs have been made by using this technique (*83*).

Advantages of LITI include its applicability to a broad spectrum of organic materials, patterning accuracy (±2-5 μm compared with ±15-20 μm for shadow-masking and inkjet-printing techniques), ability to pattern multilayer structures in a single step, scalability of the process to large substrates, and ability to reach production-scale takt time requirements (*84*). However, LITI introduces thermal defects in the organics materials during patterning due to the ablation process. The process is extremely sensitive to particulates and similar contamination of substrate and donor surfaces, which places stringent requirements on processing-atmosphere cleanliness. Furthermore, LITI requires a primary deposition process to create the (multilayered) films on the donor substrate in the first place, which potentially adds cost and complexity. Material transfer from a donor stamp prepatterned with a relief structure can be useful (provided the stamp can be cleaned and reused) and potentially mitigates the thermal damage but remains sensitive to particulate contamination.

1.6 Organic Vapor Jet Printing

To address the limitations of shadow masking in combination with VTE or OVPD, and to enable direct, additive patterning for small molecular organic semiconductors, a new technique was developed in the early 2000s: OVJP (*10*). As illustrated in **Fig. 1-12**, similar to the process in OVPD, the organic material is evaporated into a carrier gas, which, upon picking up the vapor, is ejected at high velocity through a collimating nozzle directed at the cooled substrate.

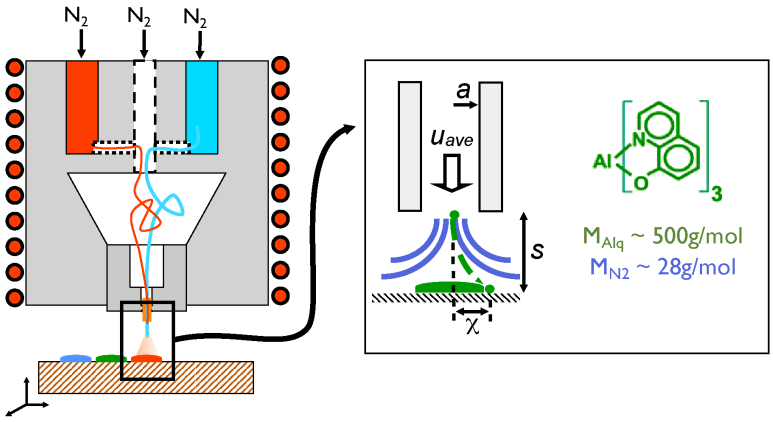

Figure 1-12 Illustration of Organic Vapor Jet Printing (OVJP)
Organics vapor jet printing: left - Schematic of the organic vapor jet printing (OVJP) apparatus, shown with two source cells (as an example), a center dilution channel, and a modular collimating nozzle, all heated from the outside. A hot inert carrier gas enters the apparatus, picks up the organic vapor, and ejects the gas mixture through the nozzle. The collimated vapor jet impinges onto a cooled substrate where the organic molecules selectively physisorb, forming a well-defined deposit. right - diagram defining the geometry relevant to pattern formation, also depicting the diverging carrier gas (N_2) flow streamlines and the collimated trajectories of heavier organic molecules. (*85*)

Mass conservation principles suggest that the master equation (Eq. 1.3) developed for OVPD should still hold true in describing the net rate of material delivery via the nozzle in OVJP, with the main difference being the pressure inside the evaporation cell and the gas (fluid) dynamics in the region between the nozzle and the substrate. A pressure drop is required across the nozzle to achieve flow collimation, which implies that the net gas overpressure experienced by the organic material in the source cell is generally larger than that in OVPD. Consequently, the effective

vapor pressure of the organic material is lowered, which requires the source temperature or total evaporative area to be increased to compensate for the drop in effective vapor pressure. (Note that the drop in vapor pressure is roughly linear with overpressure, whereas net evaporation rate is exponential with temperature.)

After the organic vapor is entrained in the carrier gas being driven through the collimating nozzle, the jet rapidly expands due to a combination of pressure drop and proximity of the substrate. The carrier gas does not condense on the substrate, flowing outward from the axis of the nozzle at a rate that is inversely proportional to the nozzle- to substrate distance. Owing to the symmetry of the apparatus, flow in the region directly downstream of the nozzle and above the substrate is stagnant, with a boundary layer that can have a nontrivial dependence on process variables. Transport of organic molecules across this stagnation zone determines the printed feature size, deposition rate, and material utilization efficiency. As **Fig. 1-12** illustrates, the organic molecules have a mass lower than that of the carrier gas and thus follow trajectories different from those of the latter, determined by the temperature, pressure, and geometry of the apparatus. In case when OVJP is performed under vacuum, typical downstream vacuum levels on the order of 0.1-10 Torr (similar to those in OVPD), achieved using cost-effective roughing pumps, are sufficient to reduce λ to the 10-100 μm range, although the dynamic pressure in the region between the nozzle and the substrate can easily exceed 10 Torr. Nevertheless, λ can fall within an order of magnitude of critical apparatus dimensions- namely, nozzle diameter and nozzle-to-substrate separation distance and operation within this intermediate regime (i.e., where the *Kn* ranges between 0.1 and 10) can complicate process modeling.

A simple scaling analysis reveals how patterning resolution depends on the major process variables. The analysis assumes that organic molecular dispersion is driven principally by

isotropic diffusion and by the outward flow of the carrier gas. Because of the heterogeneous and partially molecular nature of the flow in the deposition region, the number of molecular collisions and the mass differential between the carrier gas and organic molecules provide a rough guide to the net amount of sideways deflection an organic molecule will experience during its transit from the nozzle exit toward the substrate:

$$\frac{\chi}{a} = \frac{s}{\lambda}\frac{m_{CG}}{m_{org}} + \sqrt{\frac{D \cdot s}{u_{ave} \cdot a^2}} \quad (1.6)$$

where χ is pattern dispersion, a is nozzle diameter, s is nozzle-substrate separation, λ is molecular mean free path at the working pressure, m_{cg} and m_{org} are the carrier gas and organic molecular weights, D is organic molecular diffusivity in the carrier gas at the working pressure, and u_{ave} is average flow velocity through the nozzle. The left-hand side of the equation is a scaled amount of pattern dispersion, the first term on the right-hand side of the equation denotes the scaled amount of deflection experienced by the organic molecules via the outflowing carrier gas, and the second term on the right-hand side denotes the contribution of isotropic molecular diffusion. Experiments that vary s, m_{cg}, and λ via the chamber pressure confirm the trend predicted by Eq. 1.8. Moreover, direct-simulation Monte Carlo models (*10, 85, 86*) that track molecular trajectories and deposit shapes confirm these predictions. Shtein et al. (*10, 85*) initially demonstrated the OVJP process by using single glass capillaries and also single 20-μm-diameter, laser-drilled, stainless-steel nozzles to print patterns of neat organic material. Feature sizes of 30 μm were obtained, which translated to printing resolutions of over 500 dots per inch. An example of a printed pattern and the system geometry are shown in **Fig. 1-12**. The OVJP tool was used to draw continuous films of pentacene and make organic TFTs with hole mobilities of 0.2 cm^2/V-s, comparable with those achieved by VTE-grown films (*9*). Fluorescent emission α-NPD-Alq3 OLEDs with EQE = 0.84% were also grown by this method. The efficiency of the fluorescent

OLEDs grown by OVJP was comparable with that of conventionally processed devices (*87*). Very high local deposition rates (e.g., well over 100 nm/s) were achieved. Subsequent work by Arnold, McGraw, and colleagues (*87, 88*) showed that high efficiency, doped electrophosphorescent OLEDs can be realized by OVJP on a common substrate by using a MEMS-fabricated multinozzle array. In-plane patterning resolution on the order of a micrometer has been shown (*89*). Furthermore, the overall material utilization efficiency, particularly in laboratory-scale apparatus, is found to be orders of magnitude greater than that in VTE or OVPD. These capabilities in principle enable the use of OVJP for both non- patterned and patterned film deposition over a wide range of applications and production volumes.

As mentioned previously, the ability to create discrete patterns is often required in the fabrication of organic devices (e.g., in typical subpixel layouts in the emissive components or backplane electronics for OLED displays). To enable pixilation of the deposit at high deposition rates, Yun and coworkers (*90*) developed digital-mode OVJP, wherein the vapor jet can be vented through a digitally controlled valve (**Fig. 1-13**) before reaching the nozzle exit.

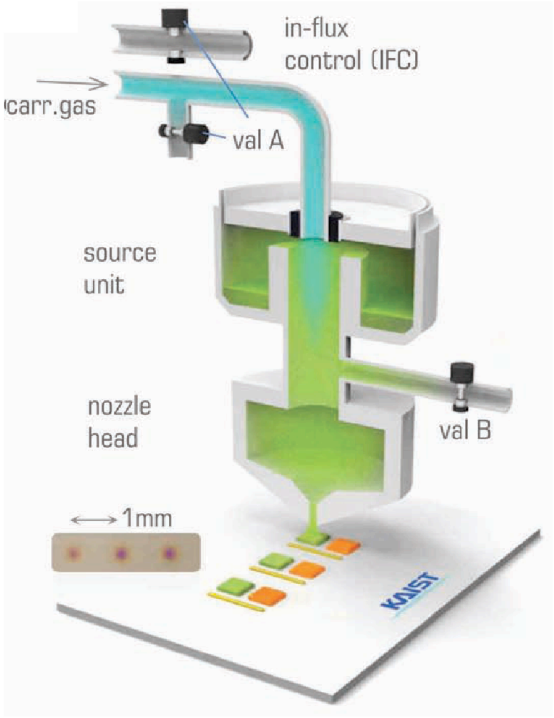

Figure 1-13 Schematic of D-OVJP system (*90*)

Guard Flow-enhanced Organic Vapor Jet Printing (GF-OVJP), developed by Biswas et. al. potentially enables to deposit and pattern device-quality organic thin films in air. In this system a guard flow is added to original OVJP set up. When depositing at ambient conditions, the downstream pressure is 1 bar, and the hot organic vapor can mix with the surrounding oxygen and moisture en route to the substrate, potentially causing oxidation at elevated temperatures and compromising device performance. Degradation is mitigated by concentrically surrounding the primary jet with a secondary jet of inert gas. The experimental apparatus shown in **Fig. 1-14** consists of two glass tubes pulled to form coaxial nozzles. The evaporant organic powder is placed inside the inner tube and heated above the sublimation temperature (T_{Source}) of the compounds at the upstream pressure (P_0), and the nozzle walls were maintained at a temperature higher than T_{Source} to prevent parasitic condensation. The nozzle-substrate separation (s) in the initial GF-OVJP experiments was maintained between 0.5 - 1 mm, while the substrate was

mounted on a three-axis linear motion stage, with the substrate holder chilled to maintain its temperature below 40◦C ($T_{Substrate}$) in the ambient. Because the mole fraction of organic molecules entrained in the jet is less than 10^{-3} in all of these experiments, the thermal conductivity (κ) and viscosity (μ) for both the primary and guard jet can be approximated by those of the carrier gas. The carrier gas flow rate (Q_{CG}) of the main jet and the guard jet mass-flow rate (Q_{GF}) were controlled by using mass-flow controllers. The process therefore entailed more than six independently controllable parameters, Q_{CG}, Q_{GF}, T_{Source}, $T_{Substrate}$, translation speed of the substrate (v_x), and nozzle geometry (d and d_{GF}), apart from the choice of inert gas used for the carrier gas and guard flow- considerably more parameters than those used in VTE or OVPD. This wider choice of process parameters potentially enables access to a wider range of deposition regimes, which in turn enables formation of films with new morphologies that are not easily accessible by using traditional growth techniques (*91-93*). On one hand, greater number of controllable parameters result in better ability to control the process. On the other hand, mapping the parameters in such a system is a complicated task, which is not always achievable through analytical solutions. In a following chapters we will demonstrate how deposition parameters in OVJP and GF OVJP can be mapped and describe an approach to full modeling of such a system.

Figure 1-14 demonstrates schematic of the GF-OVJP dual-nozzle apparatus, along with the independently controllable process parameters. The nozzle provides for an annular inert guard jet to shield and hydrodynamically focus the organic vapor-containing primary jet when printing in air. The inset shows the side view and cross-section images of the nozzle.

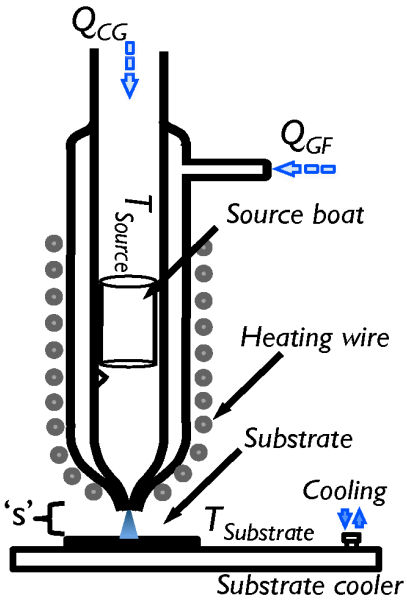

Figure 1-14 Schematic of Guard Flow OVJP
Schematic of the guard flow-enhanced OVJP dual-nozzle apparatus, along with the independently controllable process parameters. The nozzle provides an annular inert guard jet to shield and hydrodynamically focus the organic vapor-containing primary jet when printing in ambient.

Biswas et al. (*91*) demonstrated the ability to deposit electron donor and acceptor layers as well as full heterojunctions using GF-OVJP. In depositing donor films, it was shown that optimizing guard flow rate can improve molecular ordering while also reducing film roughness, which results in an overall enhancement to the power conversion efficiency of the OPV cell. Since the GF-OVJP apparatus is compact and enables deposition of device-quality films in air, factors that potentially enable an even broader range of in situ characterization techniques that can be used to study the growth process. Biswas et. al. (*93*) used GF-OVJP for in-situ growth study of pentacene-based OTFTs. Synchrotron X-ray diffraction was employed, complemented by measurement of electronic properties of GF-OVJP deposited films in a TFT to reveal how the morphology and electronic properties of the films depend on thickness, location within the printed pattern, nozzle translation velocity, and other process parameters. The hole field-effect mobility of the printed pentacene film was linked quantitatively with its crystallinity, as well as

with extent of exposure to ambient air during deposition. In a following chapters we will describe how same approach was used to study unique growth and morphology in OVJP.

1.7 Controlling Morphology via Process Conditions

Film morphology, crystalline ordering, phase, orientation, roughness and purity can strongly impact the properties of organic semiconductors including absorption, carrier mobility, exciton diffusion, energy levels (HOMO/LUMO), and luminescence properties. It is therefore important to understand the mechanisms for growth of these materials to better engineer and optimize structures for useful applications.

For instance, increased molecular order can result in better charge mobility and improved exciton-diffusion efficiency (*94, 95*). However, use of amorphous films at the donor-acceptor interface in OPVs decreases the interaction between donor and acceptor molecules and minimizes the parasitic polaron-pair recombination rate (*95*). Morphology of deposited films can also affect the total junction area as well as contact continuity. All these factors must be taken into account when choosing a deposition technique. During film formation, the driving forces that induce nucleation, growth, and crystallization of organic semiconductors strongly depend on the kinetic and thermal properties of the arriving admolecules. In VTE, for instance, the molecular motion is ballistic with relatively high kinetic and low thermal energies; therefore, the film is usually smooth with an amorphous structure. Note that increasing substrate temperature to promote crystallization can dramatically lower the sticking coefficient. In contrast to VTE, in OVPD the spatially averaged molecular kinetic energy is low due to randomizing collisions, whereas the thermal energy imparted to the topmost layers of the film is high as a result of the much larger frequency of carrier gas molecule collisions with the substrate. Furthermore, a blanket of carrier gas above the substrate can redirect desorbing molecules back toward the

substrate. As a result, polycrystalline films can be more readily obtained (*92, 96*) for a given rate of deposition that would result in amorphous films by VTE. In OVJP, molecular velocity and temperature can be adjusted, and therefore molecular orientation and morphology can be controlled more closely. For example, when films are deposited by GF-OVJP, guard flow affects crystallinity, morphology, and device performance in OPV devices, and Kang et al. (*97*) showed how carrier gas temperature effects pentacene thin-film formation in OTFTs.

The differences between conventional inorganic and organic semiconductor growth modes has been summarized by Forrest (*9*). Covalent and ionic bonding characterize inorganic structures while organic molecules interact primarily via polarization forces, collectively referred to as van der Waals forces. The van der Waals forces of individual atoms are relatively weak (~10^{-3}-10^{-1} eV/bond), but summed over many atoms in a molecule add up to a significant total energy. These forces can be described by the Buckingham or Lennard-Jones potentials:

$$\varphi(r) = A\left[\left(\frac{B}{r}\right)^{12} - \left(\frac{B}{r}\right)^{6}\right] \quad (1.7)$$

A and B are atomic potential constants fit to experimental data and r is the molecular separation. The first term stems from core repulsion (and is an approximation to an exponential) and the second term derives from the London attractive forces (induced-dipole - induced-dipole interaction).

Inorganic thin films (<100 nm thickness) commensurate growth, or epitaxy, is achieved for lattice-matched materials and near-equilibrium growth conditions. Because of this requirement, a significant limitation exists to possible material combinations. Epitaxy can occur for both chemisorbed materials (conventional epitaxy) and weakly binding physisorbing materials (van der Waals epitaxy (vdWE)). Depending on the strength of the substrate-adsorbate interactions,

chemisorption vs. physisorption, three growth modes are commonly observed: layer-by-layer (Frank-van-der-Merwe), layer-plus-islanding (Stranski-Krastinov), and islanding (Vollmer-Weber) (*98*). These growth modes are diagrammed in **Fig. 1-15**.

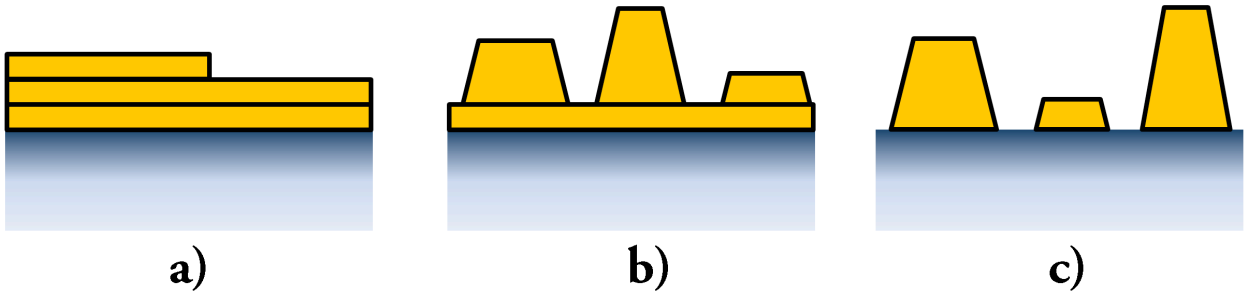

Figure 1-15 Common epitaxy growth modes
Common epitaxy growth modes: (a) layer-by-layer (Frank-van-der-Merwe), (b) layer-plus-islanding (Stranski-Krastinov), (c) islanding (Vollmer-Weber) (*98*)

Both Stranski-Krastinov and Volmer-Weber growth modes arise from an accumulation of lattice strain. Systems exhibiting vdWE typically build up strain very quickly, resulting in amorphous or polycrystalline growth after only a few monolayers (*99-101*). In contrast, organic materials can be grown with long-range order and well-defined orientations despite incommensurate lattices between substrate and adsorbate. This form of growth has been termed quasi-epitaxy (QE) and is primarily achieved for non-equilibrium conditions, unlike vdWE, even though the bulk bonding of many organics is van der Waals in nature.

Due to relatively low elastic modulus, strain relaxation in organic films growth can happen at substantial films thicknesses (hundreds of nanometers), and result in various interesting micro- and nano- structures. These features have many promising applications: in optoelectronic devices with unique charge and light transfer properties, in sensors, and in the pharmaceutical and food industries. Despite the potential in the field, the number of studies that was performed to understand micro-scale evolution of small molecular films is scarce. One of the reasons for this

lies in complexity involved with thick film growth. Due to many growth parameters and complex surface geometry of the films, no analytical models exist to predict surface evolution. Existing molecular dynamic modeling techniques, typically used for thin films growth of several nanometers are not feasible since they are computationally expensive. For instance, to simulate thick, 100 nm organic film with area of $1mm^2$, the number of molecules that need to be simulated would be on the order of 10^{14}. Therefore, a more "coarse-grained" microstructure evolution modeling approach would be needed. In this case film growth and evolution is described as a motion of a microscopic surface (*105*). The evolution is then governed by material properties, such as surface energy, thermal and mechanical properties, as well as driving forces arising due a certain deposition method, such as temperature gradients, electrical and magnetic fields, etc. In **Chapter 4** we will show how this approach can be applied to simulation of various thick film (>100 nm) morphologies grown in OVJP and how the approach can generally be applicable to different materials and deposition systems.

1.8 Summary

Since the early discoveries of photovoltaic effects and electroluminescence in conjugated organic compounds and the pioneering work of Tang on heterojunctions, the performance of organic semiconductor materials and device architectures has steadily improved. Small molecular compounds comprise a large fraction of commercially viable materials at the heart of the devices in question (e.g., organic LEDs, solar cells, transistors, sensors). They are generally incompatible with processing approaches deployed in traditional microelectronic manufacturing. Consequently, there is considerable room (and, indeed, urgency) to develop scalable deposition and patterning methods for this class of materials.

The success of commercial-scale, organic-based optoelectronics is contingent upon the ability to scale up thin-film deposition methods to large (e.g., >4 m^2) substrates and the ability to achieve rapid deposition and patterning with fine control over pixel dimensions (e.g., < ±1 nm in thickness and < ±5 μm in size). Future development is anticipated to also include refinement of additive patterning capabilities, improvements in deposition speed and morphology control, and minimization of the energy budget for processing. OVJP is a technique that enables mask-free, solvent-free, direct, additive patterning and deposition of small molecular materials in a variety of ambient conditions, with control of morphology and electronic properties via the processing parameters. Since OVJP approach enables printing of thick organic deposits, it can be incorporated as a research and manufacturing tool in a variety of new applications such as cosmetics, food and pharmaceutical industries.

1.9 References

1. D. Kearns, M. Calvin, Photovoltaic Effect and Photoconductivity in Laminated Organic Systems. *The Journal of Chemical Physics* **29**, 950 (1958).
2. C. W. Tang, Two‐layer organic photovoltaic cell. *Applied Physics Letters* **48**, 183 (1986).
3. K. S. Yook, J. Y. Lee, Organic Materials for Deep Blue Phosphorescent Organic Light-Emitting Diodes. *Advanced Materials* **24**, 3169 (2012).
4. B. W. D'Andrade *et al*., Realizing white phosphorescent 100 lm/W OLED efficacy. *Proceedings SPIE 7051, Organic Light Emitting Materials and Devices XII*, 70510Q (2008).
5. M. A. Green, K. Emery, Y. Hishikawa, W. Warta, E. D. Dunlop, Solar cell efficiency tables (Version 45). *Progress in Photovoltaics: Research and Applications* **23**, 1 (2015).
6. J. Smith *et al*., Solution-Processed Small Molecule-Polymer Blend Organic Thin-Film Transistors with Hole Mobility Greater than 5 cm2/Vs. *Advanced Materials* **24**, 2441 (2012).
7. S. Biswas, O. Shalev, M. Shtein, Thin-Film Growth and Patterning Techniques for Small Molecular Organic Compounds Used in Optoelectronic Device Applications. *Annual Review of Chemical and Biomolecular Engineering* **4**, 289 (2013).
8. J. N. Israelachvili, *Intermolecular and surface forces: revised third edition*. Academic press (2011).
9. S. R. Forrest, Ultrathin Organic Films Grown by Organic Molecular Beam Deposition and Related Techniques. *Chemical Reviews* **97**, 1793 (1997).

10. M. Shtein, P. Peumans, J. B. Benziger, S. R. Forrest, Direct, Mask- and Solvent-Free Printing of Molecular Organic Semiconductors. *Advanced Materials* **16**, 1615 (2004).
11. M. Shtein, Organic vapor phase deposition and vapor jet printing for electronic and optoelectronic device applications, Thesis, Princeton University (2004).
12. R. R. Lunt III, The growth, characterization, and application of highly ordered small molecule semiconducting thin films, Thesis, University of Michigan (2010).
13. H. J. Wagner, R. O. Loutfy, C.-K. Hsiao, Purification and characterization of phthalocyanines. *Journal of Materials Science* **17**, 2781 (1982).
14. J. R. Wojciechowski *et al*., Organic Photodiodes for Biosensor Miniaturization. *Analytical Chemistry* **81**, 3455 (2009).
15. E. L. Ratcliff *et al*., A Planar, Chip-Based, Dual-Beam Refractometer Using an Integrated Organic Light-Emitting Diode (OLED) Light Source and Organic Photovoltaic (OPV) Detectors. *Analytical Chemistry* **82**, 2734 (2010).
16. Y.-S. Tyan, Organic light-emitting-diode lighting overview. *Journal of Photonics for Energy* **1**, 011009 (2011).
17. G. Horowitz, Organic thin film transistors: From theory to real devices. *Journal of Materials Research* **19**, 1946 (2004).
18. B. P. Rand, J. Genoe, P. Heremans, J. Poortmans, Solar cells utilizing small molecular weight organic semiconductors. *Progress in Photovoltaics: Research and Applications* **15**, 659 (2007).
19. D. Yue, P. Khatav, F. You, S. B. Darling, Deciphering the uncertainties in life cycle energy and environmental analysis of organic photovoltaics. *Energy & Environmental Science* **5**, 9163 (2012).
20. A. Bernanose, M. Comte, P. Vouaux, A new method of emission of light by certain organic compounds. *The Journal of Chemical Physics* **50**, 64 (1953).
21. W. Helfrich, W. G. Schneider, Recombination Radiation in Anthracene Crystals. *Physical Review Letters* **14**, 229 (1965).
22. C. W. Tang, S. A. VanSlyke, Organic electroluminescent diodes. *Applied Physics Letters* **51**, 913 (1987).
23. M. A. Baldo *et al*., Highly efficient phosphorescent emission from organic electroluminescent devices. *Nature* **395**, 151 (1998).
24. A. Yadav, Y. Jin, P. K. L. Chan, M. Shtein, K. P. Pipe, Intermolecular electronic coupling in organic molecular thin films measured by temperature modulation spectroscopy. *Applied Physics Letters* **97**, 203307 (2010).
25. C. D. Dimitrakopoulos, P. R. L. Malenfant, Organic Thin Film Transistors for Large Area Electronics. *Advanced Materials* **14**, 99 (2002).
26. H. E. Katz, Recent Advances in Semiconductor Performance and Printing Processes for Organic Transistor-Based Electronics. *Chemistry of Materials* **16**, 4748 (2004).
27. C. W. Tang, A. C. Albrecht, Chlorophyll-a photovoltaic cells. *Nature* **254**, 507 (1975).
28. G. Yu, J. Gao, J. C. Hummelen, F. Wudl, A. J. Heeger, Polymer photovoltiac cells: Enhanced efficiencies via a network of internal donor-acceptor heterojunctions. *Science* **270**, 1789 (1995).
29. E. Tekin, P. J. Smith, U. S. Schubert, Inkjet printing as a deposition and patterning tool for polymers and inorganic particles. *Soft Matter* **4**, 703 (2008).
30. A. W. Hains, Z. Liang, M. A. Woodhouse, B. A. Gregg, Molecular Semiconductors in Organic Photovoltaic Cells. *Chemical Reviews* **110**, 6689 (2010).

31. H. Hoppe, N. S. Sariciftci, Organic solar cells: An overview. *Journal of Materials Research* **19**, 1924 (2004).
32. M. D. Perez, C. Borek, S. R. Forrest, M. E. Thompson, Molecular and Morphological Influences on the Open Circuit Voltages of Organic Photovoltaic Devices. *Journal of the American Chemical Society* **131**, 9281 (2009).
33. J. Clark, G. Lanzani, Organic photonics for communications. *Nature Photonics* **4**, 438 (2010).
34. S. Chénais, S. Forget, Recent advances in solid-state organic lasers. *Polymer International* **61**, 390 (2012).
35. I. D. W. Samuel, G. A. Turnbull, Organic Semiconductor Lasers. *Chemical Reviews* **107**, 1272 (2007).
36. P. Peumans, V. Bulović, S. R. Forrest, Efficient, high-bandwidth organic multilayer photodetectors. *Applied Physics Letters* **76**, 3855 (2000).
37. T. Morimune, H. Kajii, Y. Ohmori, Photoresponse Properties of a High-Speed Organic Photodetector Based on Copper–Phthalocyanine Under Red Light Illumination. *IEEE Photonics Technology Letters* **18**, 2662 (2006).
38. J. C. Blakesley *et al*., Organic semiconductor devices for X-ray imaging. *Nuclear Instruments and Methods in Physics Research Section A: Accelerators, Spectrometers, Detectors and Associated Equipment* **580**, 774 (2007).
39. X. Xu, M. Davanco, X. Qi, S. R. Forrest, Direct transfer patterning on three dimensionally deformed surfaces at micrometer resolutions and its application to hemispherical focal plane detector arrays. *Organic Electronics* **9**, 1122 (2008).
40. X. Xu, M. Mihnev, A. Taylor, S. R. Forrest, Organic photodetector arrays with indium tin oxide electrodes patterned using directly transferred metal masks. *Applied Physics Letters* **94**, 043313 (2009).
41. K. H. An, B. O'Connor, K. P. Pipe, Y. Zhao, M. Shtein, Scanning optical probe microscopy with submicrometer resolution using an organic photodetector. *Applied Physics Letters* **93**, 033311 (2008).
42. A. Pais, A. Banerjee, D. Klotzkin, I. Papautsky, High-sensitivity, disposable lab-on-a-chip with thin-film organic electronics for fluorescence detection. *Lab on a Chip* **8**, 794 (2008).
43. M. R. Antognazza, U. Scherf, P. Monti, G. Lanzani, Organic-based tristimuli colorimeter. *Applied Physics Letters* **90**, 163509 (2007).
44. J. Xue, S. Uchida, B. P. Rand, S. R. Forrest, Asymmetric tandem organic photovoltaic cells with hybrid planar-mixed molecular heterojunctions. *Applied Physics Letters* **85**, 5757 (2004).
45. P. Peumans, S. Uchida, S. R. Forrest, Efficient bulk heterojunction photovoltaic cells using small-molecular-weight organic thin films. *Nature* **425**, 158 (2003).
46. R. Pandey, A. A. Gunawan, K. A. Mkhoyan, R. J. Holmes, Efficient Organic Photovoltaic Cells Based on Nanocrystalline Mixtures of Boron Subphthalocyanine Chloride and C60. *Advanced Functional Materials* **22**, 617 (2012).
47. W. Gao, A. Kahn, Electrical doping: the impact on interfaces of π -conjugated molecular films. *Journal of Physics: Condensed Matter* **15**, S2757 (2003).
48. Q. Zhang *et al*., Highly efficient resonant coupling of optical excitations in hybrid organic/inorganic semiconductor nanostructures. *Nature Nanotechnology* **2**, 555 (2007).

49. S. Blumstengel, S. Sadofev, J. Puls, F. Henneberger, An Inorganic/Organic Semiconductor "Sandwich" Structure Grown by Molecular Beam Epitaxy. *Advanced Materials* **21**, 4850 (2009).
50. L. Kilian, E. Umbach, M. Sokolowski, Molecular beam epitaxy of organic films investigated by high resolution low energy electron diffraction (SPA-LEED): 3,4,9,10-perylenetetracarboxylicacid-dianhydride (PTCDA) on Ag(1 1 1). *Surface Science* **573**, 359 (2004).
51. L. Kilian *et al*., Role of Intermolecular Interactions on the Electronic and Geometric Structure of a Large π -Conjugated Molecule Adsorbed on a Metal Surface. *Physical Review Letters* **100**, 136103 (2008).
52. N. Koch, Organic Electronic Devices and Their Functional Interfaces. *ChemPhysChem* **8**, 1438 (2007).
53. I. G. Hill, D. Milliron, J. Schwartz, A. Kahn, Organic semiconductor interfaces: electronic structure and transport properties. *Applied Surface Science* **166**, 354 (2000).
54. A. Kitaigorodsky, *Molecular crystals and molecules*. Elsevier (2012), vol. 29.
55. E. Silinš̆, V. Capek, *Organic molecular crystals: interaction, localization, and transport phenomena*. American Institute of Physics (1994).
56. M. Shtein, H. F. Gossenberger, J. B. Benziger, S. R. Forrest, Material transport regimes and mechanisms for growth of molecular organic thin films using low-pressure organic vapor phase deposition. *Journal of Applied Physics* **89**, 1470 (2001).
57. M. Shtein, Organic Vapor-Phase Deposition in *Organic Electronics: Materials, Processing, Devices and Applications*, F. So, Ed., CRC Press, 27 (2009).
58. R. B. Bird, W. E. Stewart, E. N. Lightfoot, *Transport phenomena*. JohnWiley & Sons, New York (2002).
59. J. C. Slattery, R. B. Bird, Calculation of the diffusion coefficient of dilute gases and of the self-diffusion coefficient of dense gases. *AIChE Journal* **4**, 137 (1958).
60. T. R. Marrero, E. A. Mason, Gaseous Diffusion Coefficients. *Journal of Physical and Chemical Reference Data* **1**, 3 (1972).
61. T. X. Zhou, T. Ngo, J. J. Brown, M. Shtein, S. R. Forrest, Stable and efficient electrophosphorescent organic light-emitting devices grown by organic vapor phase deposition. *Applied Physics Letters* **86**, 021107 (2005).
62. C. Cali, V. Daneu, A. Orioli, S. Riva-Sanseverino, Flash evaporation of compounds with a pulsed-discharge CO2 laser. *Applied Optics* **15**, 1327 (1976).
63. Y. S. Tyan, M. Long, G. Phelan, T. Cushman, Vapor deposition apparatus and method, Patent, US20070098891 (2007).
64. M. Long *et al*., Enabling High-Throughput, Low-Cost Manufacturing of OLED Display and Lighting Panels. *MRS Online Proceedings Library Archive* **1212**, 1212 (2009).
65. M. Shtein, P. Peumans, J. B. Benziger, S. R. Forrest, Micropatterning of small molecular weight organic semiconductor thin films using organic vapor phase deposition. *Journal of Applied Physics* **93**, 4005 (2003).
66. C. Py, D. Roth, I. Lévesque, J. Stapledon, A. Donat-Bouillud, An integrated shadow-mask based on a stack of inorganic insulators for high-resolution OLEDs using evaporated or spun-on materials. *Synthetic Metals* **122**, 225 (2001).
67. C. W. Tang, K. C. Pan, Full color active matrix organic electroluminescent display panel having an integrated shadow mask, Patent, US6384529 (2002).

68. M. A. Haase, P. F. Baude, R. C. Williams, Method of making full color display panels, Patent, EP1399967 B1 (2007).
69. J. Chen *et al*., Direct Patterning of Molecular Organic Materials and Metals Using a Micromachined Printhead. *MRS Online Proceedings Library Archive* **870**, H1.8 (2005).
70. J. Chen *et al*., High Definition Digital Fabrication of Active Organic Devices by Molecular Jet Printing. *Advanced Functional Materials* **17**, 2722 (2007).
71. V. Leblanc, J. Chen, S. H. Kang, V. Bulovic, M. A. Schmidt, Micromachined Printheads for the Evaporative Patterning of Organic Materials and Metals. *Journal of Microelectromechanical Systems* **16**, 394 (2007).
72. C. G. Courcimault, M. G. Allen, Reconfigurable shadow mask technology: a microsystem for metal nanoline deposition. *Nanotechnology* **15**, S528 (2004).
73. H. Sirringhaus *et al*., High-Resolution Inkjet Printing of All-Polymer Transistor Circuits. *Science* **290**, 2123 (2000).
74. C. J. Drury, C. M. J. Mutsaers, C. M. Hart, M. Matters, D. M. de Leeuw, Low-cost all-polymer integrated circuits. *Applied Physics Letters* **73**, 108 (1998).
75. T. R. Hebner, C. C. Wu, D. Marcy, M. H. Lu, J. C. Sturm, Ink-jet printing of doped polymers for organic light emitting devices. *Applied Physics Letters* **72**, 519 (1998).
76. M. Singh, H. M. Haverinen, P. Dhagat, G. E. Jabbour, Inkjet Printing—Process and Its Applications. *Advanced Materials* **22**, 673 (2010).
77. J. A. Rogers *et al*., Paper-like electronic displays: Large-area rubber-stamped plastic sheets of electronics and microencapsulated electrophoretic inks. *Proceedings of the National Academy of Sciences* **98**, 4835 (2001).
78. J. Zaumseil *et al*., Nanoscale organic transistors that use source/drain electrodes supported by high resolution rubber stamps. *Applied Physics Letters* **82**, 793 (2003).
79. C. Kim, P. E. Burrows, S. R. Forrest, Micropatterning of Organic Electronic Devices by Cold-Welding. *Science* **288**, 831 (2000).
80. C. Kim, M. Shtein, S. R. Forrest, Nanolithography based on patterned metal transfer and its application to organic electronic devices. *Applied Physics Letters* **80**, 4051 (2002).
81. C.-C. Wu, C.-C. Yang, H.-H. Chang, C.-W. Chen, C.-C. Lee, Finite-source dye-diffusion thermal transfer for doping and color integration of organic light-emitting devices. *Applied Physics Letters* **77**, 794 (2000).
82. G. B. Blanchet, Y.-L. Loo, J. A. Rogers, F. Gao, C. R. Fincher, Large area, high resolution, dry printing of conducting polymers for organic electronics. *Applied Physics Letters* **82**, 463 (2003).
83. J. Y. Lee, S. T. Lee, Laser-Induced Thermal Imaging of Polymer Light-Emitting Materials on Poly(3,4-ethylenedioxythiophene): Silane Hole-Transport Layer. *Advanced Materials* **16**, 51 (2004).
84. S. Lamansky *et al*., Laser induced thermal imaging of vacuum-coated OLED materials. *Proceedings SPIE 5937, Organic Light-Emitting Materials and Devices IX*, 593702 (2005).
85. M. Shtein, P. Peumans, J. B. Benziger, S. R. Forrest, Direct mask-free patterning of molecular organic semiconductors using organic vapor jet printing. *Journal of Applied Physics* **96**, 4500 (2004).
86. G. Bird, Monte Carlo simulation of gas flows. *Annual Review of Fluid Mechanics* **10**, 11 (1978).

87. M. S. Arnold, G. J. McGraw, S. R. Forrest, R. R. Lunt, Direct vapor jet printing of three color segment organic light emitting devices for white light illumination. *Applied Physics Letters* **92**, 053301 (2008).
88. G. J. McGraw, D. L. Peters, S. R. Forrest, Organic vapor jet printing at micrometer resolution using microfluidic nozzle arrays. *Applied Physics Letters* **98**, 013302 (2011).
89. G. J. McGraw, S. R. Forrest, Fluid dynamics and mass transport in organic vapor jet printing. *Journal of Applied Physics* **111**, 043501 (2012).
90. C. Yun *et al*., Digital-Mode Organic Vapor-Jet Printing (D-OVJP): Advanced Jet-on-Demand Control of Organic Thin-Film Deposition. *Advanced Materials* **24**, 2857 (2012).
91. S. Biswas, K. P. Pipe, M. Shtein, Solvent-free, direct printing of organic semiconductors in atmosphere. *Applied Physics Letters* **96**, 263301 (2010).
92. F. Yang, S. R. Forrest, Photocurrent Generation in Nanostructured Organic Solar Cells. *ACS Nano* **2**, 1022 (2008).
93. S. Biswas *et al*., Spatial Mapping of Morphology and Electronic Properties of Air-Printed Pentacene Thin Films. *Advanced Functional Materials* **24**, 3907 (2014).
94. J. D. Zimmerman *et al*., Independent Control of Bulk and Interfacial Morphologies of Small Molecular Weight Organic Heterojunction Solar Cells. *Nano Letters* **12**, 4366 (2012).
95. D. Yokoyama, Molecular orientation in small-molecule organic light-emitting diodes. *Journal of Materials Chemistry* **21**, 19187 (2011).
96. M. Shtein, J. Mapel, J. B. Benziger, S. R. Forrest, Effects of film morphology and gate dielectric surface preparation on the electrical characteristics of organic-vapor-phase-deposited pentacene thin-film transistors. *Applied Physics Letters* **81**, 268 (2002).
97. H. W. Kang, C. Yun, S. Yoo, S. H. Ko, H. J. Sung, Effect of carrier gas temperature on pentacene thin film formation by organic vapor-jet printing techniques. *Thermochimica Acta* **542**, 74 (2012).
98. N. Karl, C. Guenther, Structure and Ordering Principles of Ultrathin Organic Molecular Films on Surfaces of Layered Semiconductors Organic-on-Inorganic MBE. *Crystal Research and Technology* **34**, 243 (1999).
99. J. A. Venables, G. D. T. Spiller, M. Hanbucken, Nucleation and growth of thin films. *Reports on Progress in Physics* **47**, 399 (1984).
100. M. Möbus, N. Karl, The growth of organic thin films on silicon substrates studied by X-ray reflectometry. *Thin Solid Films* **215**, 213 (1992).
101. M. Eremtchenko, J. A. Schaefer, F. S. Tautz, Understanding and tuning the epitaxy of large aromatic adsorbates by molecular design. *Nature* **425**, 602 (2003).
102. C. Seidel, C. Awater, X. D. Liu, R. Ellerbrake, H. Fuchs, A combined STM, LEED and molecular modelling study of PTCDA grown on Ag(110). *Surface Science* **371**, 123 (1997).
103. S. R. Forrest, Y. Zhang, Ultrahigh-vacuum quasiepitaxial growth of model van der Waals thin films. I. Theory. *Physical Review B* **49**, 11297 (1994).
104. P. Fenter, F. Schreiber, L. Zhou, P. Eisenberger, S. R. Forrest, In situ studies of morphology, strain, and growth modes of a molecular organic thin film. *Physical Review B* **56**, 3046 (1997).
105. Z. Suo, Motions of Microscopic Surfaces. *Solid Mechanics* **33**, 193 (1997).

Chapter 2
Thermophysical Properties of Small Organic Molecules

2.1 Overview

As the production of organic-based semiconductor devices scales up, knowing the precise sublimation characteristics of these materials is crucial for designing deposition apparatus and controlling the deposition processes, calculating fundamental limits of production throughput, estimating the fabrication energy budget, as well as for developing new film growth and patterning techniques. However, despite the growing industrial importance of this class of materials and their processing science, published studies of their sublimation behavior and thermodynamic properties are scarce. We show how thermogravimetry can be used to determine the vapor pressure (P_{vap}) and sublimation enthalpy (ΔH) values of various archetypal compounds, including: phthalocyanines - boron subphthalocyanine chloride (SubPc), iron phthalocyanine (FePc), copper phthalocyanine (CuPc), zinc phthalocyanine (ZnPc) , metal-free phthalocyanine (H_2Pc), as well as pentacene, tris(8-hydroxyquinolino)aluminum (Alq_3), 3,4,9,10-perylenetetracarboxylic dianhydride (PTCDA). This approach is simple, convenient, and provides consistent and reliable thermophysical property values. The following chapter is based on reference (*1*), published by O. Shalev and M. Shein.

2.2 Kinetic theory of gases

The average velocity of gas molecules as described by Maxwell velocity distribution theory, is given by (*2*):

$$\Omega = \sqrt{\frac{8RT}{\pi M}} \quad (2.1)$$

where: *R*- Universal Gas Constant, *T*- temperature, *M*- molecular weight. In any given direction the average component of velocity is $1/2\Omega$ and since half of molecules are moving toward the solid and half away from it, the gas mass striking given surface area per unit time is given by:

$$\frac{dm}{dt}\frac{1}{A} = \frac{1}{4}\rho\Omega \quad (2.2)$$

where: *A*- evaporating surface area, ρ- gas density (*3*). Assuming ideal gas, gas density can be rewritten as:

$$\rho = \frac{PM}{RT} \quad (2.3)$$

where *P*- gas vapor pressure. Substituting (3) into (2), relationship between evaporation rate and vapor pressure at given temperature is given by:

$$-\frac{dm}{dt}\frac{1}{A} = \alpha P\sqrt{\frac{M}{2\pi RT}} \quad (2.4)$$

where α- vaporization coefficient. For evaporation in vacuum $\alpha=1$. In case of vaporization of material into flowing gas stream, α can no longer be assumed as unity. Rearranging Eq. 2.4 and assuming constant sample surface area:

$$P = k\nu \quad (2.5)$$

$$k = \alpha^{-1}\frac{1}{A}(2\pi R)^{1/2} \quad (2.6)$$

$$\nu = \left[\left(\frac{T}{M} \right)^{1/2} \left(\frac{dm}{dt} \right) \right] (2.7)$$

A plot of P vs. ν for standard material with known vapor pressure- temperature dependence allows calibration system constant k to be determined and thus the vapor pressures of unknown materials to be found. The temperature dependence of the vapor pressure can be described by the Clausius-Clapeyron equation (*3*):

$$\ln P = A - \frac{B}{T} \quad (2.8)$$

$$B = \frac{\Delta H}{R} \quad (2.9)$$

where ΔH is the molar enthalpy of sublimation in the case of a solid. Thus the enthalpies of sublimation of the samples can be found from the slope of a plot of *ln(P)* vs. reciprocal absolute temperature.

2.3 Experimental techniques for studying of thermophysical materials properties

Generally, vapor-liquid or vapor-solid equilibrium can be studied by static and kinetic methods. An example of the former is the direct detection by a pressure gauge of an evaporating substance in a closed vessel. Examples of kinetic measurements include Knudsen effusion, the Langmuir method, and flow-based techniques (*4-6*). These are applied depending on the range of P_{vap} and evaporation temperature involved; e.g. static methods are simple and reliable, but are typically limited to pressures above 1 Torr. One of the most reliable methods for the investigation of materials with vapor pressure in the range of 10^{-7} Torr < P_{vap} < 10^{-1} Torr and evaporation temperature ranging between 350°C and 600°C is the Knudsen effusion method, based on the measurement of the rate of effusion of equilibrated vapor through a small orifice. The main

drawback of the Knudsen method is a need for specially designed equipment. For flow-based techniques, Price (*4*) has shown that it is possible to obtain accurate and meaningful thermodynamic data using a standard thermobalance. The testing equipment is calibrated using pure reference materials of known vapor pressure and exploiting the relationship between sublimation rate and vapor pressure based on the Langmuir equation for free evaporation. This approach is used here.

It has been shown before (*5*) that crystal structure has an influence on P_{vap} of volatile phthalocyanines. Planar molecules exhibit tighter packing in crystals than non-planar molecules, and consequently stronger intermolecular interaction. This results in relatively larger values of sublimation enthalpy, ΔH, and relatively low saturated vapor pressures (e.g.: unsubstituted phthalocyanines usually exhibit enthalpies of about 200 kj/mole and vapor pressures on the order of 1^{-4} Torr at 350 °C). Molecular weight also influences ΔH and P_{vap} (*7*); e.g. for sublimation, heavier molecules will usually exhibit higher ΔH and lower P_{vap} (*7*). In the present study, a strong correlation between mass density ρ, ΔH and P_{vap} was revealed, consistent with the Van Der Waals and electrostatic bonding character of the tested compounds and potentially useful for estimating the evaporation behavior of yet uncharacterized compounds. The correlation was validated using several well-characterized small molecular organic materials, and is shown to predict ΔH of other compounds.

2.4 Experimental Setup and System Calibration

All measurements were performed using a TA Instruments thermogravimetric analyzer (TGA) Q500 system (99.99% accuracy) with nitrogen sample purge flow rate 60 ml/min and balance purge flow rate of 40 ml/min. Samples were placed in tared, 7 mm diameter aluminum pans. For

system calibration, benzoic acid was used (Sigma - Aldrich, purity > 99.5%). Schematic drawing of experimental setup is shown in **Fig. 2-1**.

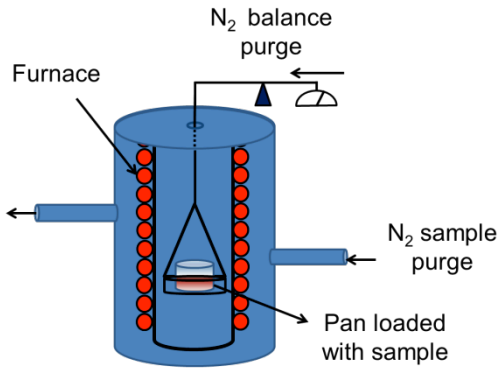

Figure 2-1 Schematic drawing of TGA Q500 system

All tested materials were in the form of crystalline powders prepurified by vacuum sublimation: pentacene- Sigma-Aldrich, > 99.9%; Alq_3, PTCDA, CuPc, ZnPc- Luminescence Technology Corporation, sublimed grade; H_2Pc- Acros Organics, > 99%; FePc- TCI America, > 95%. Temperature set points during the tests were determined by first heating each sample at 5°C/min until sufficient sublimation was observed. A new sample was then heated to the desired temperature and held at each temperature for 30 minutes. The rate of mass loss at each temperature was then calculated and converted to pressure using the Langmuir relation (*2*) and the system constant determined as described above. The obtained pressure-temperature relation was then plotted and Clausius- Clapeyron constants were calculated using the least-squares method.

A typical calibration curve was obtained using benzoic acid. Reference values for the vapor pressure were taken from the literature (*8*); a plot of P vs. ν was linear ($R^2 = 0.995$), as was expected by Langmuir theory.

An example of the testing procedure is presented for PTCDA. **Figure 2-2** shows the relative mass loss of PTCDA under 5°C/min heating rate, as well as isotherms for each temperature

setpoint between 420-500°C. Since sublimation rate is zeroth-order in time, the plot of mass loss vs. time in the inset of **Fig. 2-2** is linear ($R^2 > 0.999$). This also indicates that the free surface area of the sample did not change appreciably during the experiment. Extracting the slope for each temperature, the vapor pressure can be calculated using Eq. 2.8.

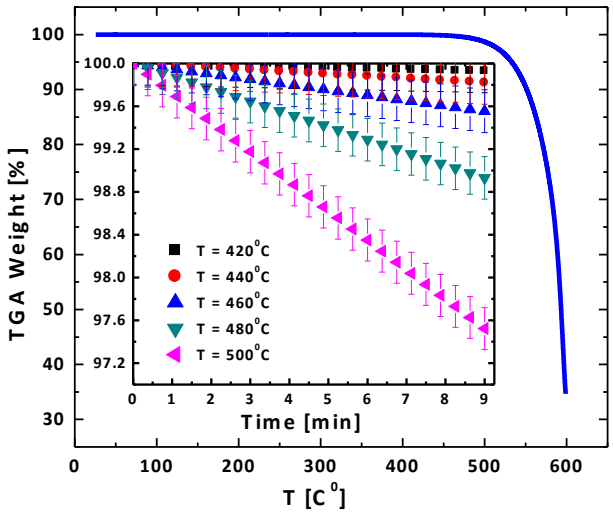

Figure 2-2 Weight loss thermogram of PTCDA ($C_{24}H_8O_6$) at heating rate 5°C/min
Weight loss thermogram of PTCDA ($C_{24}H_8O_6$) at heating rate 5°C/min. Inset - mass percent change of PTCDA under isothermal heating (*1*).

2.5 Effect of crystal density on sublimation properties of molecular organic semiconductors

The vapor pressures for the tested materials are presented in **Fig. 2-3**. Among the phthalocyanines, ZnPc shows the lowest vapor pressure and SubPc the highest. The differences in volatilities among the phthalocyanines are attributed to the molecular structural factors and bonding. For example, SubPc has a non-planar structure (**Fig. 2-3a**), causing less effective stacking with a lower degree of intermolecular interaction compared with the planar phthalocyanines. The lower number of moieties responsible for bonding - e.g. phenyl rings, and lower molecular weight - can also contribute to this effect. The rest of the unsubstituted

phthalocyanines have planar structures with herringbone packing. H_2Pc has slightly higher vapor pressure than the unsubstituted phthalocyanines due to a lack of central metal ion, which increases intermolecular forces (*5*). The introduction of the central metal (e.g., in CuPc) into the phthalocyanine macrocycle leads to the additional intermolecular interaction due to overlapping of the antibinding orbitals of nitrogen atoms of overlying and underlying phthalocyanine molecules with the 3d-orbitals of the central metal ion (*5*).

Among the rest of the tested materials (**Fig. 2-3b)**, pentacene and Alq_3 have significantly higher vapor pressures than PTCDA. For pentacene this result can be explained by a lower molecular weight than that of Alq_3, PTCDA and SubPc. Alq_3 and SubPc are non-planar molecules with poorer stacking, as compared to PTCDA (known for its high planarity (*9*)), and the weaker lower intermolecular interaction leads to lower sublimation enthalpy and higher vapor pressure than PTCDA.

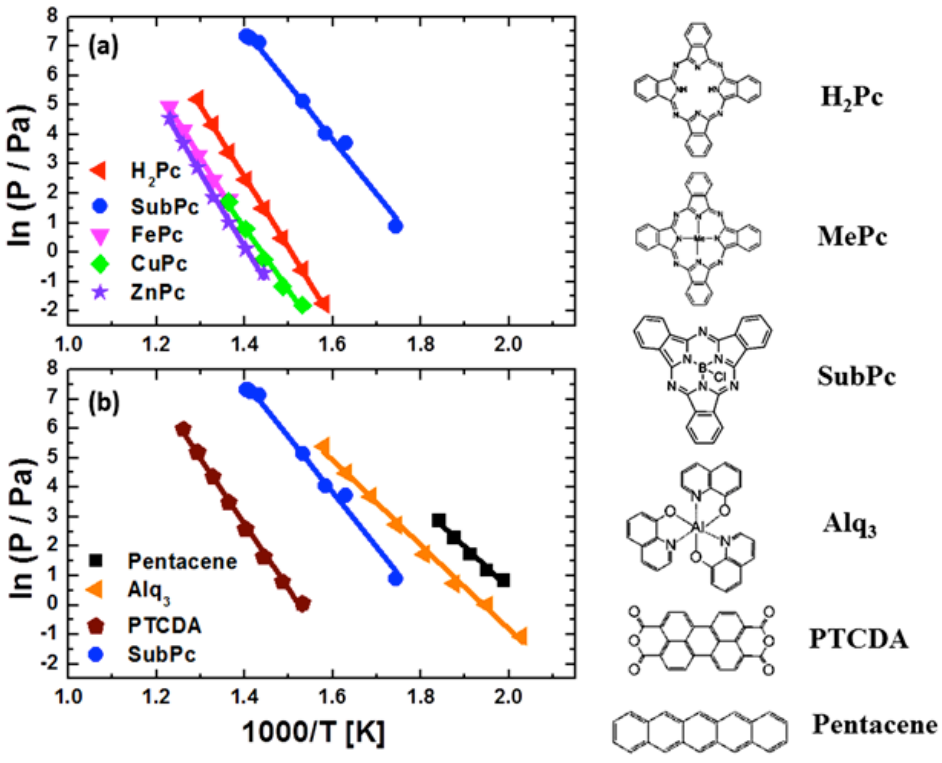

Figure 2-3 Vapor pressure and molecular structures (Me - central metal ion)

The summarized thermophysical data, the Clausius-Clapeyron constants and sublimation enthalpies, as well as a comparison of the obtained data to literature values are given in **Table 2-1**. Most of the data are in good agreement with the literature values. The discrepancies are mainly attributed to differences in purity, morphology and use of different systems and calibration methods in published reports.

Table 2-1 Thermophysical experimental and literature data of tested materials

				Experimental Results			Literature Data		
Material	**Formula**	**MW (gr/mole)**	**Temp (°C)**	**A**	**B**	**ΔH (kj/mole)**	**A**	**B**	**ΔH (kJ/mole)**
Pentacene	$C_{22}H_{14}$	278	230-270	28.8	14104±76	117.3±0.7	35.8(*10*)	18867(*10*)	156.9±13.6(*10*)
Alq_3	$C_{27}H_{18}AlN_3O_3$	459	220-360	27.9	14384±36	119.6±0.3	-	-	137.7(*11*), 164±1.2(*12*)
PTCDA	$C_{24}H_8O_6$	392	380-520	34.0	22327±43	185.6±0.5	-	-	146.5[a]
H_2Pc	$C_{32}H_{18}N_8$	514	360-500	36.4	24240±7	201.5±0.1	39.9(*5*)	26910(*5*)	170.84[a], 224.7(*5*)
SubPc	$C_{24}H_{12}BN_6Cl$	431	300-440	34	18885±84	155.6±0.7	-	-	-
FePc	$C_{32}H_{16}FeN_8$	568	460-540	34.2	23878±53	198.0±0.5	-	-	-
CuPc	$C_{32}H_{16}CuN_8$	576	380-460	30.7	21307±96	177.1±1	36(*5*)	25386(*5*)	211.1(*5*), 176±1.5(*12*)
ZnPc	$C_{32}H_{16}ZnN_8$	577	420-540	35.2	24963±36	207.5±0.5	33.5(*5*)	24230(*5*)	202±8(*5*)

[a] Sublimation enthalpy was calculated using group contribution (GC) method (*13*)

Figures 2-4 and **2-5** plot the sublimation enthalpy vs. crystal density of the tested compounds. The crystal density was calculated according to X-Ray Diffraction (XRD) data of the tested crystalline materials (*9, 14-17*). A strong correlation was observed between sublimation enthalpy and crystal density, as well as between vapor pressure and crystal density.

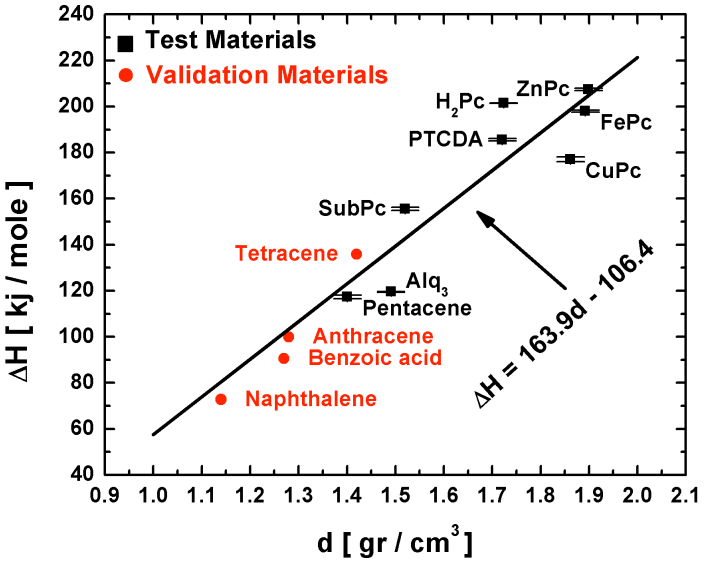

Figure 2-4 Sublimation enthalpy vs. crystal density (STP) of test and validation compounds

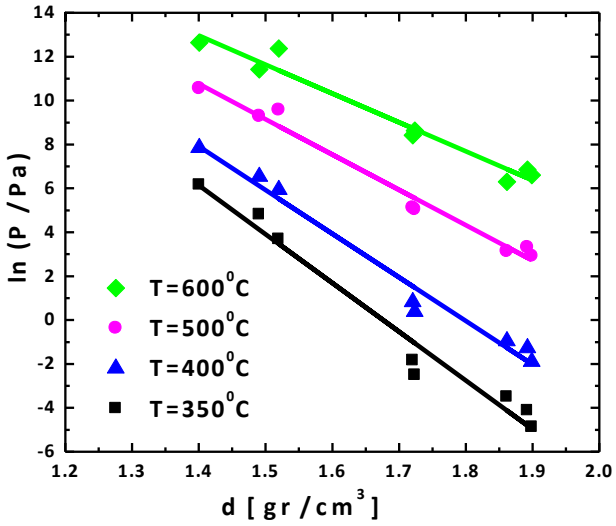

Figure 2-5 Vapor pressure vs. crystal density of tested compounds

Using linear fits in **Fig. 2-4** for the tested compounds, an empirical relationship for the prediction of sublimation enthalpy of organic molecular crystalline materials is of the form (*1*):

$$\Delta H = 163.9d - 106.4 \quad (2.10)$$

with $R^2 = 0.801$, where ΔH is the sublimation enthalpy in units of kj/mole, d is the material density in units of gr/cm^3. This relation can also be used to predict the enthalpies of different

phases or polymorphs of organic materials which can exhibit different densities, or to estimate material crystal density through information on sublimation enthalpy. We note relationships to molecular weight and to unit cell volume were also observed, but with weaker correlations than that for crystal density.

To understand the obtained relationship between ΔH and density better, a plot of density vs. the molecular weight of the compounds is shown in **Fig. 2-6**. For stronger intermolecular bonding, higher crystal density is expected. Indeed, a strong correlation exists between molecular weight and crystal density, due to the greater number of electrons participating in dispersion interactions in the larger molecule. Nevertheless, the sign and the magnitude of the deviations from the linear relation show the influence of crystal packing in each of the molecules. The highest deviations from linear relationship are obtained for Alq_3, SubPc and PTCDA. The expected crystal densities are higher than the actual densities for Alq_3 and SubPc due to their highly non-planar structures as compared to other presented molecules, while PTCDA shows higher crystal density than expected from the trend due to its high planarity.

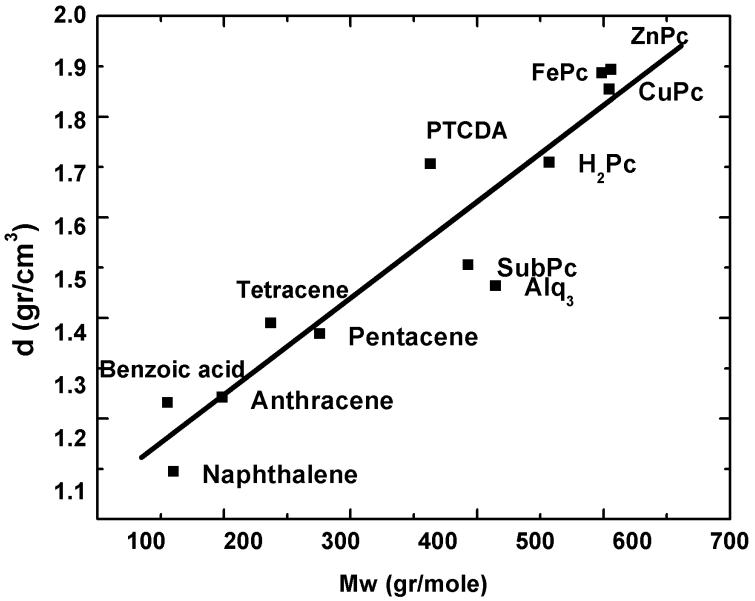

Figure 2-6 Crystal density vs. molecular weight of test and validation compounds (*1*)

Existing methods for the prediction of sublimation enthalpy of organic materials include group contribution (*13*) and the number of occurrences of different atom types (*18*). The main drawback of these models is that the crystal structure of the substance is largely ignored, which can play significant role in intermolecular interaction and therefore influence enthalpic and entropic changes during sublimation process. For instance, large differences in vapor pressures and enthalpies were observed for metal phthalocyanines having the same molecular formula and structure, but different crystallographic packing (*5*). A van der Waals surface electrostatic potential model (*19*) and statistical analysis of structural properties of hydrocarbons (*20*) take into consideration the crystal and mass densities, but the information enabling reliable statistical analysis of bonding in organometallic compounds is scarce. To describe sublimation energy in terms of crystallographic parameters, crystal lattice energy should be considered, comprising primarily three non-bonded interactions: van der Waals (repulsive and attractive) forces (*21*), electrostatic (Coulombic) forces, and hydrogen bonding energy. Each energy term is inversely proportional to some power of interatomic distance (*22*). The lattice energy is equal to the magnitude of the heat of sublimation of the crystal at absolute zero, and is defined as the lattice energy in the absence of thermal vibrations. For a material with higher packing density and lower average interatomic distances, a higher lattice energy and sublimation enthalpy are expected. Since higher molecular weight is associated with higher molecular polarizability and therefore higher dispersion forces, molecular weight also needs to be taken into account. In terms of entropic changes, a higher packing density is associated with a larger entropy increase upon vaporization. Nevertheless, it is only one of several parameters influencing entropic change during sublimation; for example it was shown that molecular symmetry might also have a strong influence on entropy (*22*).

As the discussion above touches on the complexity of predicting vaporization properties from first principles, the value of a simple and robust empirically derived means for predicting these properties is clear. To validate Eq. 2.10, other compounds with similar bonding behavior were tested, e.g.: benzoic acid, naphthalene, anthracene and tetracene - compounds for which reliable data exists. The results are presented in **Table 2-2** and **Fig. 2-4**. The deviation obtained is within 12% error. Note that the relationship embodied in **Fig. 2-4** and Eq. 2.10 is approximate, because ΔH and ρ can change with temperature.

Table 2-2 Thermophysical experimental and literature data of tested materials

Material	Formula	Mw	Crystal density (gr/cm^3)	Enthalpy of Sublimation (kj/mole)	Predicted Enthalpy of Sublimation (kj/mole)	Enthalpy of Sublimation (j/gr)
Benzoic acid	$\mathbf{C_7H_6O_2}$	122.1	1.27(*23*)	90.6±1(*8, 24*)	101.7	742.0
Naphthalene	$\mathbf{C_{10}H_8}$	128.2	1.14(*25*)	72.8±0.3(*24*)	72.6	567.9
Anthracene	$\mathbf{C_{14}H_{10}}$	178.2	1.28(*23*)	100±3(*26*)	103.3	561.2
Tetracene	$\mathbf{C_{14}H_{12}}$	228.3	1.42(*27*)	135.9±5.1(*28*)	126.3	595.3
Pentacene	$\mathbf{C_{22}H_{14}}$	278.4	1.4(*14*)	117.3±0.7[a]	123.1	421.3
Alq_3	$\mathbf{C_{27}H_{18}AlN_3O_3}$	459.4	1.49(*15*)	119.6±0.3[a]	137.9	260.3
PTCDA	$\mathbf{C_{24}H_8O_6}$	392.3	1.72(*9*)	185.6±0.5[a]	175.6	473.1
H_2Pc	$\mathbf{C_{32}H_{18}N_8}$	514.2	1.72(*17*)	201.5±0.1[a]	176.1	391.6
SubPc	$\mathbf{C_{24}H_{12}BN_6Cl}$	431.0	1.52(*16*)	155.6±0.7[a]	142.7	361.0
FePc	$\mathbf{C_{32}H_{16}FeN_8}$	568.4	1.89(*17*)	198.0±0.5[a]	203.75	348.3
CuPc	$\mathbf{C_{32}H_{16}CuN_8}$	576.1	1.86(*17*)	177.1±1[a]	198.7	307.4
ZnPc	$\mathbf{C_{32}H_{16}ZnN_8}$	577.9	1.9(*17*)	207.5±0.5[a]	204.8	359.1

[a] Experimental results, crystal density are given in (STP)

For vapor pressure prediction, the deviations in the obtained values are significantly higher than for enthalpy, which means that entropic changes attributed to molecular structure and not only the crystal density should be considered.

2.6 Summary

We show that the Langmuir relation can be applied to analyze the sublimation behavior of small molecular organic compounds, enabling the use of thermogravimetry as a rapid, simple, and reliable method for estimating the vapor pressure and the sublimation enthalpy of functional, small molecular organic compounds often used in optoelectronic devices. Since evaporative deposition is the method of choice for growing thin films and devices incorporating small molecular organic semiconductors, the data obtained here, and the general approach should be useful in designing deposition apparatus and developing new vapor-based deposition processes. The strong correlation between evaporation parameters and crystal density can be used in the future to estimate useful properties of new materials or those that have not been fully characterized. (*17*)

2.7 References

1. O. Shalev, M. Shtein, Effect of crystal density on sublimation properties of molecular organic semiconductors. *Organic Electronics* **14**, 94 (2013).
2. I. Langmuir, The vapor pressure of metallic tungsten. *Phys. Rev.* **2**, 329 (1913).
3. R. Clausius, Ueber die bewegende Kraft der Wärme und die Gesetze, welche sich daraus für die Wärmelehre selbst ableiten lassen. *Annalen der Physik* **155**, 500 (1850).
4. D. M. Price, Vapor pressure determination by thermogravimetry. *Thermochimica Acta* **367-368**, 253 (2001).
5. T. Basova, P. Semyannikov, V. Plyashkevich, A. Hassan, I. Igumenov, Volatile Phthalocyanines: Vapor Pressure and Thermodynamics. *Critical Reviews in Solid State and Materials Sciences* **34**, 180 (2009).
6. H. Ipser, Vapor pressure methods: A source of experimental thermodynamic data. *Berichte der Bunsengesellschaft für physikalische Chemie* **102**, 1217 (1998).
7. M. H. Charlton, R. Docherty, M. G. Hutchings, Quantitative structure-sublimation enthalpy relationship studied by neural networks, theoretical crystal packing calculations and multilinear regression analysis. *Journal of the Chemical Society, Perkin Transactions 2*, 2023 (1995).
8. H. G. Wiedemann, Applications of thermogravimetry for vapor pressure determination. *Thermochimica Acta* **3**, 355 (1972).
9. B. Krause *et al*., On the coexistence of different polymorphs in organic epitaxy: α and β phase of PTCDA on Ag(1 1 1). *Applied Surface Science* **175-176**, 332 (2001).

10. V. Oja, E. M. Suuberg, Vapor Pressures and Enthalpies of Sublimation of Polycyclic Aromatic Hydrocarbons and Their Derivatives. *Journal of Chemical & Engineering Data* **43**, 486 (1998).
11. Y. Kiyoshi, T. Yoshikazu, A.-k. Norihiko, K. Akira, Evaporation Rate and Saturated Vapor Pressure of Functional Organic Materials. *Japanese Journal of Applied Physics* **34**, 636 (1995).
12. M. Shtein, H. F. Gossenberger, J. B. Benziger, S. R. Forrest, Material transport regimes and mechanisms for growth of molecular organic thin films using low-pressure organic vapor phase deposition. *Journal of Applied Physics* **89**, 1470 (2001).
13. A. Tabernero, E. M. M. d. Valle, M. A. Galán, Estimation of sublimation enthalpies of solids constituted by aromatic and/or polycyclic aliphatic rings by using a group contribution method. *AIChE Journal* **58**, 2875 (2012).
14. D. Käfer, M. El Helou, C. Gemel, G. Witte, Packing of Planar Organic Molecules: Interplay of van der Waals and Electrostatic Interaction. *Crystal Growth & Design* **8**, 3053 (2008).
15. M. Rajeswaran *et al*., Structural, thermal, and spectral characterization of the different crystalline forms of Alq3, tris(quinolin-8-olato)aluminum(III), an electroluminescent material in OLED technology. *Polyhedron* **28**, 835 (2009).
16. H. Kietaibl, The crystal and molecular structure of a new phthalocyanine-like boron complex. *Monatshefte für Chemie / Chemical Monthly* **105**, 405 (1974).
17. M. Engel, Single-Crystal Structures of Phthalocyanine Complexes and Related Macrocycles in *The Porphyrin Handbook; Phthalocyanines: Structural Characterization,* vol. 20, Elsevier, 1 (2003).
18. D. Mathieu, Simple Alternative to Neural Networks for Predicting Sublimation Enthalpies from Fragment Contributions. *Industrial & Engineering Chemistry Research* **51**, 2814 (2012).
19. C. K. Kim *et al*., Prediction of physicochemical properties of organic molecules using van der Waals surface electrostatic potentials. *Journal of Computational Chemistry* **25**, 2073 (2004).
20. A. Gavezzotti, Statistical analysis of some structural properties of solid hydrocarbons. *Journal of the American Chemical Society* **111**, 1835 (1989).
21. Z. Jane Li, W. H. Ojala, D. J. W. Grant, Molecular Modeling Study Of Chiral Drug Crystals: Lattice Energy Calculations. *Journal of Pharmaceutical Sciences* **90**, 1523 (2001).
22. C. F. R. A. C. Lima *et al*., Structural and Thermodynamic Characterization of Polyphenylbenzenes. *The Journal of Physical Chemistry A* **115**, 11876 (2011).
23. W. M. Haynes, *CRC Handbook of Chemistry and Physics, 92nd Edition*. CRC Press (2011).
24. M. Colomina, P. Jimenez, C. Turrion, Vapour pressures and enthalpies of sublimation of naphthalene and benzoic acid. *The Journal of Chemical Thermodynamics* **14**, 779 (1982).
25. J. M. Robertson, The Crystalline Structure of Naphthalene. A Quantitative X-Ray Investigation. *Proceedings of the Royal Society of London A: Mathematical, Physical and Engineering Sciences* **142**, 674 (1933).
26. J. L. Goldfarb, E. M. Suuberg, Vapor Pressures and Enthalpies of Sublimation of Ten Polycyclic Aromatic Hydrocarbons Determined via the Knudsen Effusion Method. *Journal of Chemical & Engineering Data* **53**, 670 (2008).

27. J. M. Robertson, V. C. Sinclair, J. Trotter, The crystal and molecular structure of tetracene. *Acta Crystallographica* **14**, 697 (1961).
28. M. V. Roux, M. Temprado, J. S. Chickos, Y. Nagano, Critically Evaluated Thermochemical Properties of Polycyclic Aromatic Hydrocarbons. *Journal of Physical and Chemical Reference Data* **37**, 1855 (2008).

Chapter 3
Resolution

3.1 Introduction

As described in introduction section, OVJP system is an easily reconfigurable table-top system that can potentially operate in various environments, depending on the applications and properties needed. For instance, system operating conditions can be adjusted in accordance with depositing material properties: when working with highly volatile materials (substantial vapor pressure of >10 Pa at room temperature), system will need to be operated at elevated pressure in order to enable control of evaporation rate. If air stable materials are used for deposition, the need for inert environment can be relaxed. Generally speaking, expanding the conditions at which OVJP operates can allow access to new films growth modes and open a potential for new applications, as well as teaching about system performance at "extreme" conditions. For instance, S. Biswas et al. demonstrated guard flow-enhanced organic vapor jet printing (GF-OVJP) for the fabrication of organic light emitting diodes and photovoltaic cells in air, with device performances comparable to analogous device structures made using vacuum thermal evaporation (VTE) (*1, 2*). The technique utilized carrier gas (*CG*) transport of sublimated organic vapor towards the substrate in the form of a focused jet, surrounded by an annular inert guard flow jet (*GF*). GF-OVJP approach potentially enables direct, solvent-free, additive patterning of device-quality organic semiconductors in ambient air.

In this chapter we will demonstrate a pathway for enhancement of pattern resolution and deposition throughput in OVJP and GF-OVJP systems.

Because fabrication of very high resolution capable nozzles is potentially very expensive, we use larger scale experimental apparatus and printing results to validate numerical modeling of OVJP. These validated models are then used to predict advantageous nozzle geometries and printing conditions that can lead to ~1 micrometer or better pixel edge dispersion. Care is taken to ensure that the transport regime and simulation are commensurate across the different length scales, although it is recognized that reliable simulations are lacking for the transitional transport regime (i.e. between full continuum and free molecular).

This chapter is organized as follows: first an experimental study of OVJP and GF-OVJP system operating under atmospheric pressure in an inert environment will be described. The trade-offs between pattern resolution, deposition throughput and film quality will be discussed, followed by a model that enables further system modification and improvement. Using the developed model, number of examples for alternative system configurations geared toward maximization of patterning ability will be shown.

3.2 OVJP and GF-OVJP experimental setup and data analysis

Previous studies have shown that choosing low molecular mass gases (e.g. helium) for the carrier gas reduces the dispersion of the organic vapor jet and thus improves resolution when printing in vacuum at higher rates (*3*). Concomitantly, varying the guard jet flow rates has a significant impact on crystallinity, roughness and device performance of the patterned films (*1, 2*). In this study, we vary the *CG* and *GF* gases (choosing between He, N_2, Ar and CO_2) and show the effect of gas molecular weight, size, and structure, on the film's pattern resolution. We demonstrate theoretically and experimentally that the diffusivity of sublimated organic molecules

and pattern resolution can be improved by appropriate combinations of *GF*/*CG* gases and can therefore enable greater flexibility in choosing deposition conditions (sublimation and substrate temperatures, mass flow rates, etc.) for a given molecular material.

3.2.1 OVJP and GF-OVJP experimental system design

Schematics of GF-OVJP and OVJP systems are demonstrated in **Fig. 3-1**.

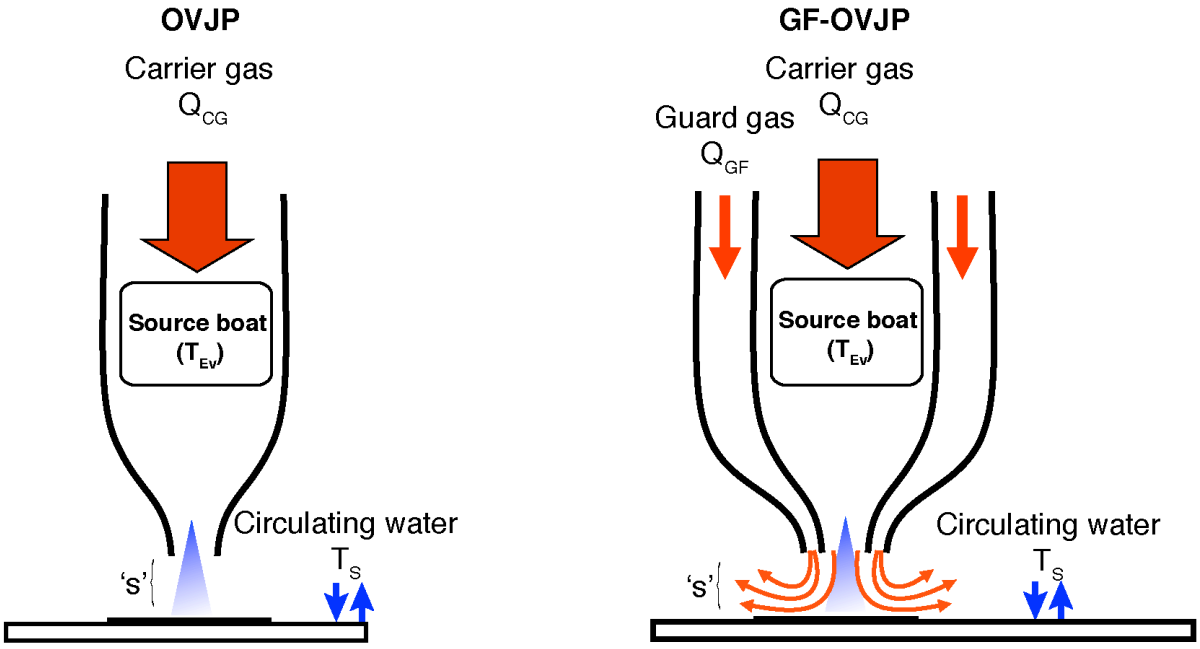

Figure 3-1 Schematic of OVJP and GF-OVJP system
The systems comprise from a number of independently controllable processing parameters: nozzle geometry, choice of carrier gas (CG) and guard flow (GF) gases (for GF-OVJP case), CG and GF mass flow rates (Q_{CG} and Q_{GF} respectively), evaporation source and substrate temperatures (T_{Ev} and T_S respectively), nozzle - substrate spacing '*s*', nozzle and substrate X and Y translation speed (V_x, V_y).

All the work in this thesis has been done with deposition nozzles made of quartz. Due to quartz thermal stability up to ~1100^{o}C, variety of small organic molecules and deposition temperatures could be used. This enabled design of different sizes and shapes of nozzles and also visual testing of nozzles after deposition. For instance, nozzle clogging and cleanness could be easily

detected and nozzle geometry could be adjusted accordingly.

For guard flow free OVJP setup, one glass tube with circular cross-section nozzle was used. Quartz tube was pulled and cut to obtain needed cross-sectional diameter. For GF-OVJP setups, the experiments were performed with two concentrical circular cross-section nozzles. For comparison studies, GF-OVJP nozzle was used as OVJP setup with guard flow gas turned off. GF-OVJP setup was made from two glass tubes placed one inside the other, with the latter being shorter than the former. Then tubes were aligned coaxially and fused at the back end. The front ends were pulled together, cooled and ground along the nozzle axis to form the nozzle exit of the required dimensions. Typical dimensions of the setup are shown in **Fig. 3-2**. In case OVJP setup is used, similar inner nozzle dimensions are used.

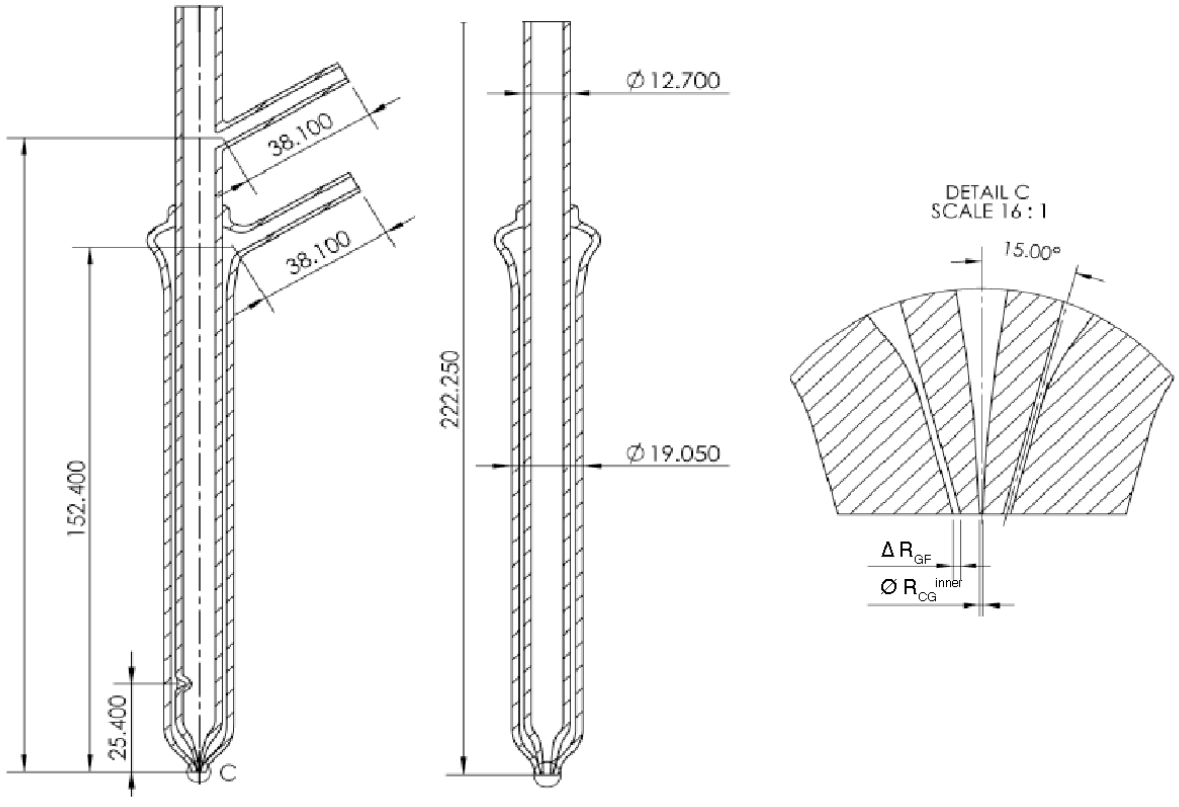

Figure 3-2 Typical dimensions in GF-OVJP system

R_{CG} and R_{GF} are the radii of the inner and outer nozzles, respectively. The main design factor to consider when choosing R_{CG} is the dimension of pixel size required for the application. The system design in our case is made for learning purposes, therefore the dimensions were chosen so that deposit pattern will be large enough for detailed analysis (180 µm), as explained in a following section, and flow conditions will be consistent with previous studies. The nozzle dimensions used in current study section are shown in **Fig. 3-3**.

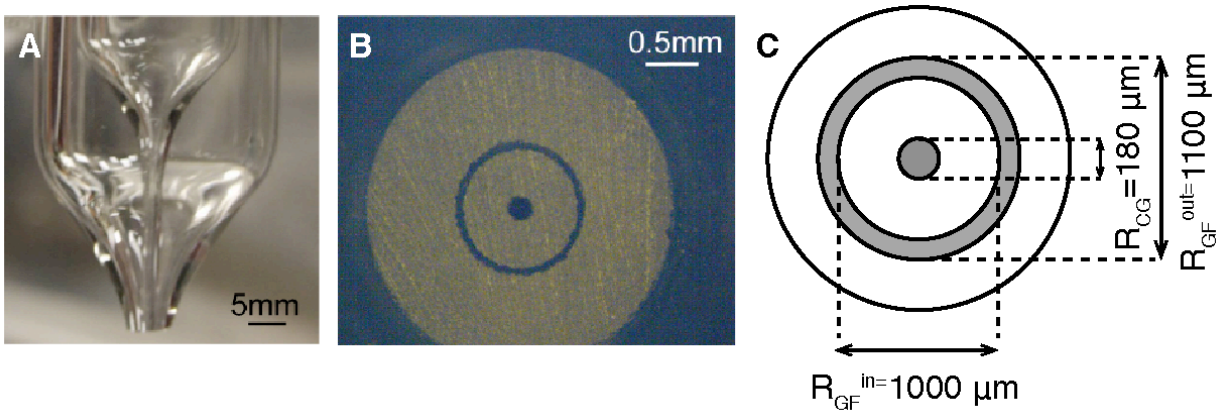

Figure 3-3 GF-OVJP nozzle used in the study
GF-OVJP circular nozzle side view and cross-section images with the geometry parameters labeled. (*4*)

The velocities magnitudes of the CG and GF jets are determined by the gas volumetric flow rates, Q_{CG} and Q_{GF}, and the nozzle cross sectional area:

$$V_{CG} = \frac{Q_{CG}}{\pi \cdot R_{CG}^2} \quad (3.1)$$

$$V_{GF} = \frac{Q_{CG}}{\pi \cdot ((R_{GF}^{out})^2 - (R_{GF}^{in})^2)} \quad (3.2)$$

For 100-200 sccm carrier gas flow rate this enables flow velocities through the nozzle exit on the order of 144-290 m sec^{-1}. This order of carrier gas velocity provides high enough vertical momentum for organic molecules to substantial number of molecules to arrive onto the substrate

positioned at ~1mm from the nozzle. Keeping in mind these parameters, the nozzle size can be decreased or increased in parallel with flow rate, in order to obtain similar flow regimes and similar effects on deposit profile in accordance with a requirement. For OVJP uses in OLED manufacturing, the nozzle size should be as small as possible, since dispersion scales roughly linearly with nozzle size (*5*). On the other hand, OPVs usually require organic deposits with large, planar area film coverage at high deposition rates. For this application, a rectangular slit nozzle with large opening can be designed and translated perpendicular to the slit length to deposit large area films of uniform thickness over a planar substrate. Additional parameter to consider is the nozzle length. Sufficiently long nozzle where nozzle length to diameter ratio is higher than 10, will enable fully developed flow with organic molecules bulk velocity similar to that of carrier gas.

The nozzle was cleaned with solvents, dried and wrapped with 36-gauge heavy insulated tape heater (Omega Engineering, Inc.) with a power density of 8.6 $W \cdot in^{-2}$. The heating tape leads were connected to a temperature controller (Digi-Sense Benchtop temperature controller, Cole-Palmer Instruments Co.) and a 1/16" K-type thermocouple was used to maintain the temperature of the source. The source consisted of 0.15 g of powder sandwiched between quartz wool and placed in the heated source section of the inner tube. The carrier gas and guard jet flow rates were maintained using mass flow controllers (C100 MFC, Sierra Instruments).

The motion of nozzle and a substrate were controlled via computer controlled XYZ- positioning stage (**Fig. 3-4**). The translation speed of the stage can vary 0.1-5 mm sec^{-1}. Gas flow rates were regulated by mass flow controllers. The process was performed in a nitrogen glove box at ~ atmospheric pressure with < 5 ppm oxygen and water. The substrate was positioned on a cooling stage with circulating water. The substrates used in the experiments were silicon (100) wafers.

These were cleaned using ultrasonication in detergent solution and deionized water followed by heated acetone, trichloroethylene and isopropanol for 10 min each. Substrates were then placed in boiling isopropanol for 5min and dried in pure nitrogen gas before film deposition. The material used in the study was Tris (8-hydroxyquinolinato) aluminium (Alq_3) at sublimed grade purity from Luminescence Technology Corp..

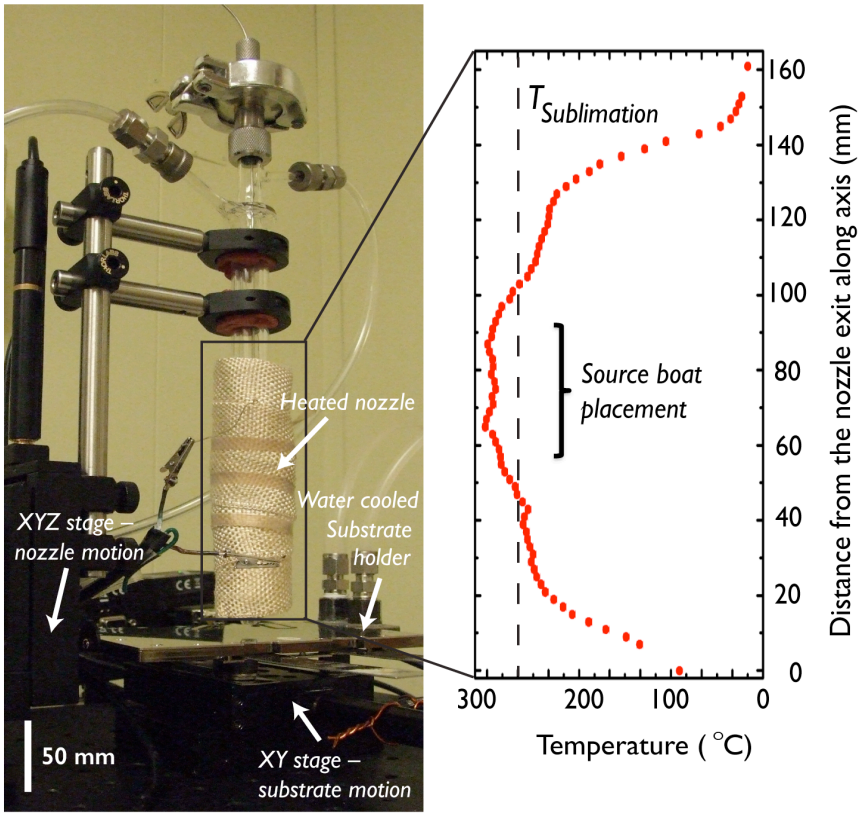

Figure 3-4 OVJP nozzle setup and temperature profile

All patterns were obtained by printing a pixel for a certain dwell time. The nozzle would approach a given coordinate at 3mm sec^{-1} speed, kept above a coordinate for a given time and moved away at 3mm sec^{-1} speed. The patterns were then analyzed with interference microscopy through illumination with monochromatic source with wavelength λ = 540 ± 10 nm. The thickness profile was extracted from digitized pattern image by counting the number of dark fringes (for destructive interference). The pattern thickness at each fringe position was calculated

with Eq. 3.3.

$$d = \frac{(m+1/2)\lambda}{2n} \quad (3.3)$$

where d is a pattern thickness, m=0,1,2,3 etc. is the fringe order and n=1.74 is the refractive index of Alq_3. In order to detect the full spread of Alq_3 pixel, fluorescence microscopy was used. An example of image analysis is demonstrated in **Fig. 3-5**.

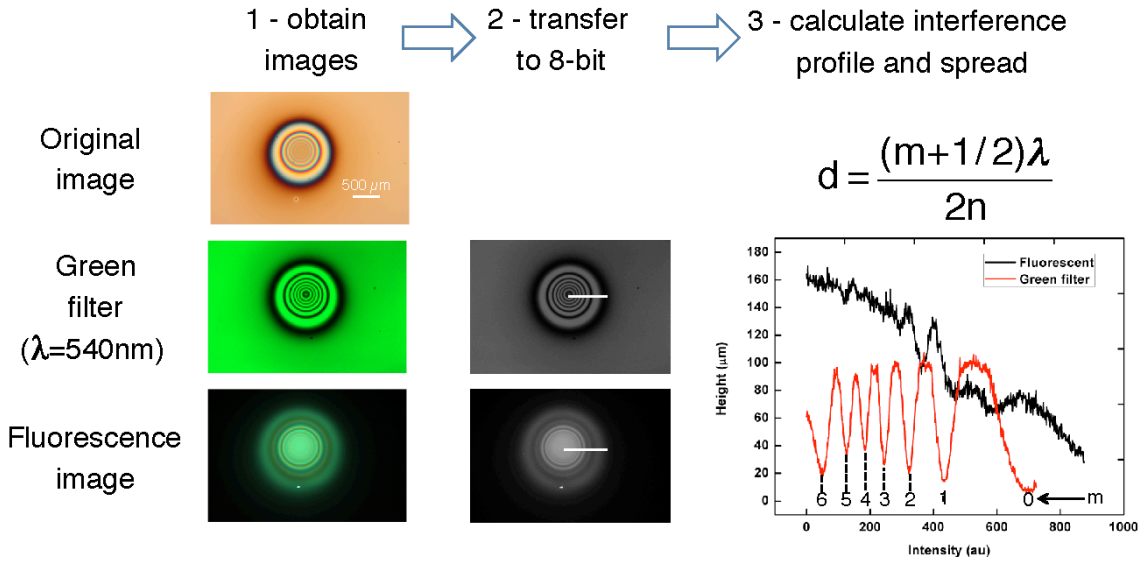

Figure 3-5 Deposit image analysis steps
Original image - bright field image obtained with optical microscope. Green filter image - same image obtained with 540 nm filter. Image then digitalized and position of black fringes and deposit spread are extracted from radial scan using Image-J software.
Variable parameters and gases types used in the study are given in **Tables 3-1** and **3-2**.

Table 3-1 Controllable variables used in study

Variable	Tested range
's' (mm)	0.3-3
Q_{CG} (sccm)	25-200
Q_{GF} (sccm)	0-150
Deposition duration- *t* (sec)	20-210

Table 3-2 Gases types with corresponding molecular weights used in the study

Tested gases	Mw (g mol^{-1})	Gas use
N_2	28	CG, GF
He	4	CG, GF
Ar	40	CG, GF
CO_2	44	GF

Variable parameters included: deposition duration, nozzle- substrate separation distance, carrier gas type and flow rate, guard flow gas type and flow rate. The following sections discuss an effect of each of the parameters. To analyze the deposits shape, size, material utilization efficiency the following parameters were calculated:

Full width half maximum (*FWHM*) of the profile was extracted through Voight function fit to the profile (**Fig. 3-5**). Base diameter was extracted from fluorescence microscopy. Both these parameters evaluate pixel size. *FWHM/Base* ratio gives an idea about profile shape. This parameter is especially important when defined pixels are required (*FWHM/Base* ➔ 1). Domed pixel profile shape (**Fig. 3-5**) is undesirable for OLED application, since it would result in a pixels crosstalk and non-uniform pixel thickness resulting in visible display defects.

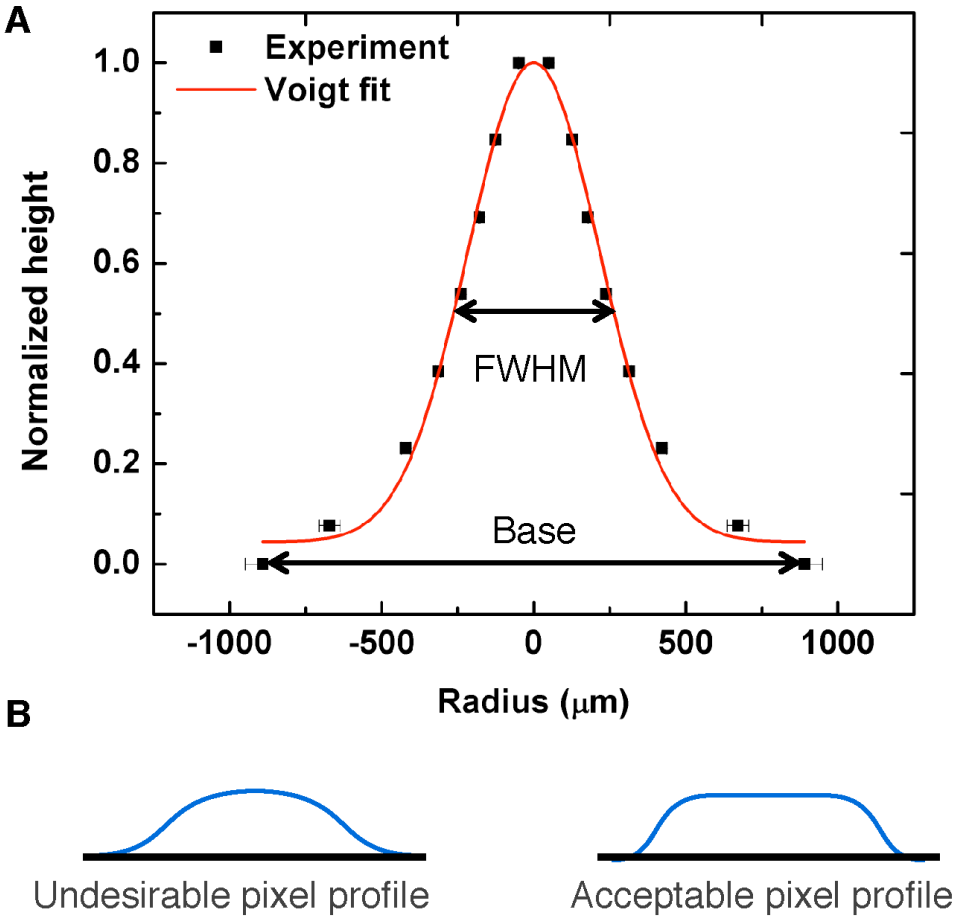

Figure 3-6 Example of pixel profile analysis

Deposit weight was calculated from 3-D integration of profile thickness multiplied by material density. Weight/Base ratio evaluates how well the deposit is focused within a given area. Deposit weight evaluates how well the material is utilized when exiting the nozzle. The following sections will demonstrate an effect of each of the variable parameters on these merits.

3.2.2 Effect of deposition duration

In order to determine how deposit shape is affected by deposition duration, nozzle dwell time above the substrate was varied from 30-210 seconds. This is an important parameter when nozzle

speed needs to be determined in order to get desired thickness deposit without hindering the resolution. This effect is demonstrated in **Fig. 3-7**. Deposit weight scales linearly with time (**Fig. 3-7a**, meaning that boundary layer thickness above the substrate for diffusion of molecules and deposition onto substrate is negligible and process is limited by convection rate of carrier gas containing the organic molecules. Deposition rate in this case is 2 μg sec^{-1}.

Deposit FWHM is not changing with deposition duration and only base diameter is increasing (**Fig. 3-7b,c**). This means that two parameters control deposit shape: the first one is the concentration profile of organic molecules in the jet above the substrate, and second is the spread of molecules around the center of the deposit. Plotting base diameter vs. square root of time reveals linear dependence (**Fig. 3-7d**), meaning that spread along the surface is diffusion - limited process ($x=\sqrt{Dt}$ where x is base diameter, D is diffusion coefficient and t is time). In case of OVJP, the hot organic molecules exiting the nozzle have high enough kinetic energy to diffuse along the surface after impinging onto the substrate. This understanding is important in order to be able to model the growth in OVJP regime, as will be shown in **Chapter 4**. In current case (substrate temperature is 20 $^{\circ}$C), the calculated surface diffusion coefficient is $3 \cdot 10^{-8}$ cm^2 sec^{-1}. Since diffusion coefficient scales up exponentially with temperature, this means that the spread can be significantly decreased at low substrate temperatures. This measurement approach also demonstrates potential usage of OVJP as a tool to determine molecular surface diffusion values and determine substrate temperature required for a specific application.

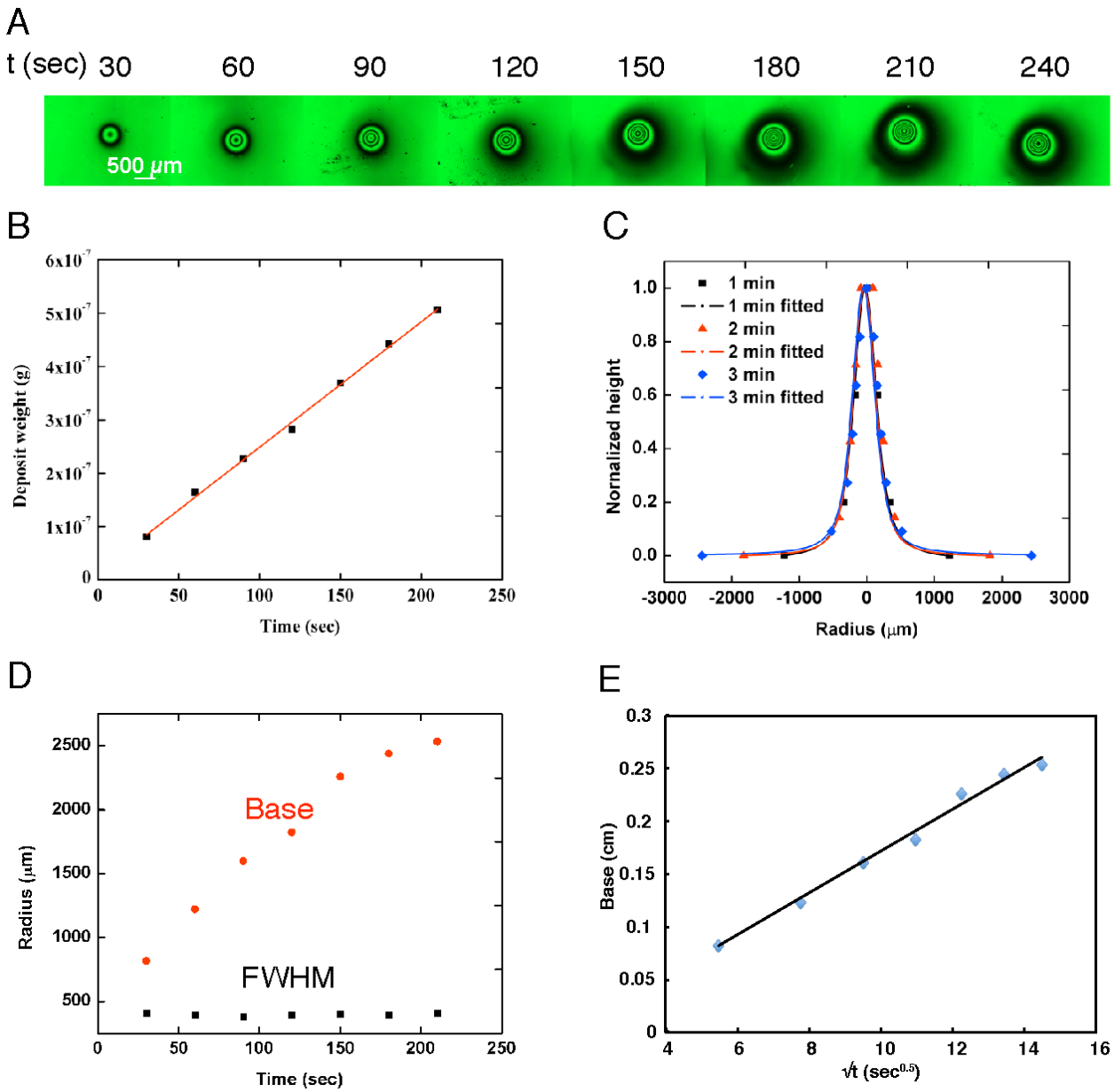

Figure 3-7 Effect of deposition duration on deposit parameters
Deposition conditions: carrier gas - He, Q_{CG}=50 sccm, Q_{GF}=0 sccm, '*s*'=0.5 mm, T_{Ev}=330°C, T_s=25°C. A: deposits images. B: Deposits weight vs. time. C: deposits profiles vs. time. D: Base diameter and FWHM vs. time. E: Base diameter vs. √t.

3.2.3 Effect of substrate-nozzle separation distance

The nozzle-substrate separation distance *'s'* is an important parameter which influences the behavior of the jets before reaching the substrate and therefore impacts the resolution of the

deposited pixel, the degree of penetration of ambient molecules inside the organic jet stream and deposition rate. This effect is demonstrated in **Fig. 3-8**. When the substrate is placed close to or beyond the intersection point, the jet streams undergo turbulent mixing (*6*) which results in broadening of the pixel. When the substrate is too far, jetted molecules lose vertical momentum and velocity during the travel, which results in decrease of utilization efficiency as compared to focused jet.

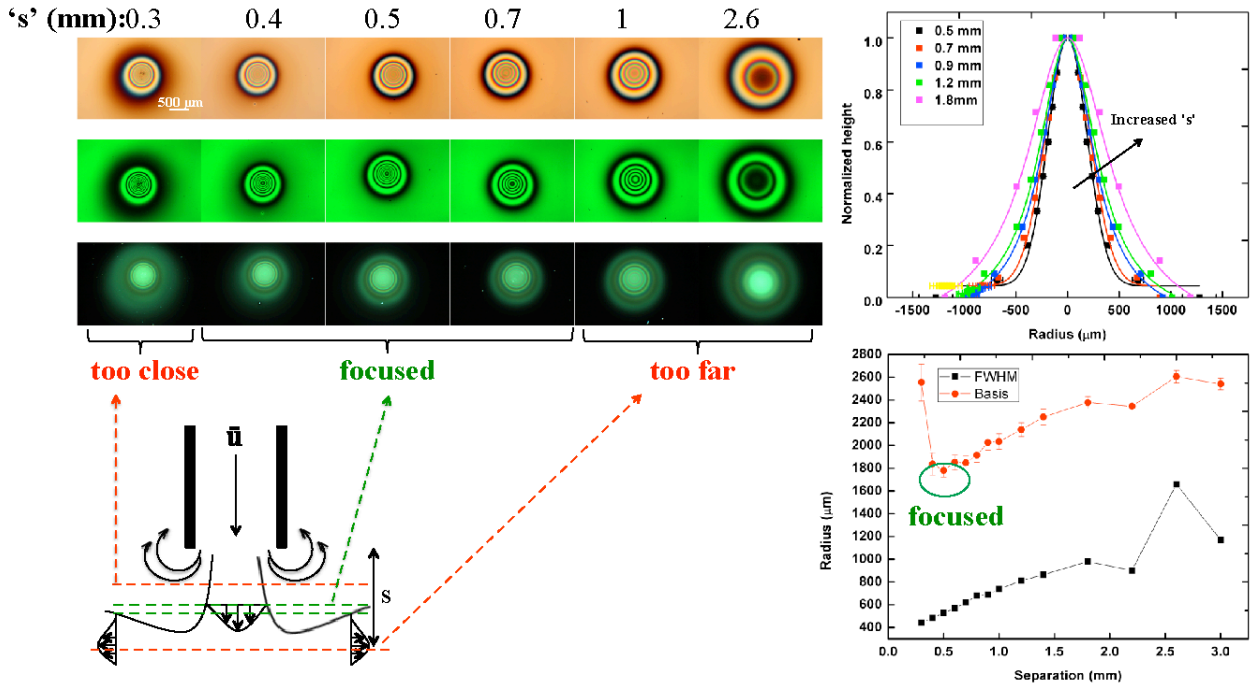

Figure 3-8 Effect of substrate-nozzle separation distance on deposit profile
Deposition conditions: Deposition conditions: carrier gas - He, Q_{CG}=50 sccm, Q_{GF}=0 sccm, T_{Ev} = 330°C, T_s = 25°C.

3.2.4 Carrier gas effect in OVJP

In OVJP system the carrier gas picks up the sublimated small molecular organic vapor, forms a jet at the CG nozzle exit and impinges onto the substrate. The heavier organic molecules have a higher momentum than the lighter CG molecules in the jet, and are more collimated (**Fig. 3-9**).

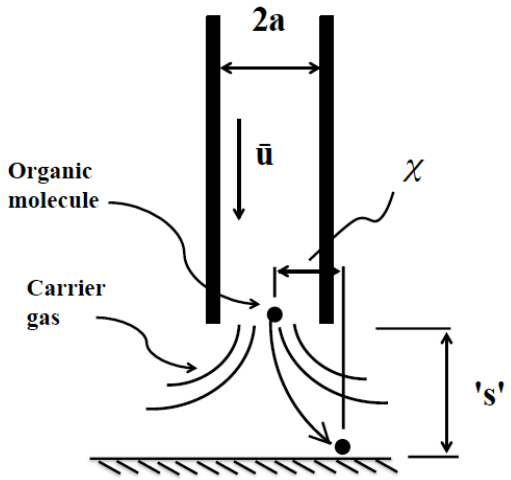

Figure 3-9 Schematic of carrier gas effect in OVJP

The molar mass and size of the carrier gas molecules play an important role in establishing the film quality. (*1-3*) The effect of carrier gas on deposit dispersion was derived qualitatively by Shtein (*7*):

$$\frac{\chi}{a} = \frac{s}{\lambda}\frac{m_{CG}}{m_{org}} + \sqrt{\frac{D \cdot s}{u_{ave} \cdot a^2}} \quad (3.4)$$

where χ is pattern dispersion, a is nozzle diameter, s is nozzle-substrate separation, λ is molecular mean free path at the working pressure, m_{cg} and m_{org} are the carrier gas and organic molecular weights, D is organic molecular diffusivity in the carrier gas at the working pressure, and u_{ave} is average flow velocity through the nozzle. Molecular diffusivity between gases A and B is defined by Chapman-Enskog theory:

$$D_{AB} = \frac{2}{3}\sqrt{\frac{k_B^3 \cdot N_A}{\pi^3}}\frac{\sqrt{T^3 \cdot (1/(2M_A) + 1/(2M_B))}}{\Omega \cdot p \cdot \left(\frac{\sigma_A + \sigma_B}{2}\right)^2} \quad (3.5)$$

where k_B and N_A are the Boltzmann constant and Avogadro number, T is the evaporation zone temperature, p is the pressure, M is the molar mass, σ is the collision diameter of each species

and Ω is the collision integral (close to 1 in this case). Diffusivities of Alq_3 in gases used in experiment at 300 °C are summarized in **Table 3-3**.

Table 3-3 Alq_3 diffusivity in gases used in experiments

Gas	He	N_2	Ar	CO_2
Mw (g mol^{-1})	4.0	28.0	39.9	44.0
σ (Å)	2.5	3.8	3.5	3.9
$D_{Alq3\text{-}gas}$ (m^2 sec^{-1})	3.2e-5	1e-5	9.3e-6	8.1e-6

Mean free path λ is given by:

$$\lambda = \frac{k_B T}{\sqrt{2}\pi d^2 p} \quad (3.6)$$

where d is molecular diameter. Since mean free path is inversely proportional to pressure, s/λ will change substantially with deposition conditions and m_{cg}/m_{org} ratio will have different effects at different pressures. G.J. McGraw, for instance, was using OVJP at conditions were s and λ were on the same order of magnitude (microns) (*8*). In this case, the effect of carrier gas type was not observed. In case of nitrogen carrier gas flowing at atmospheric pressure at 330 °C, λ is ~150nm, meaning that *'s'*>>λ. In addition, when operating at atmospheric pressures, the difference in diffusivity of the molecules in the carrier gas and in the ambient gas also plays a role. In case the diffusivity in the carrier gas is higher (e.g. carrier molecular weight is lower than that of ambient gas), the ambient gas in the system will be naturally acting as a shield of heavy molecules, preventing them to diffuse outwards. The effect of carrier gas at atmospheric pressure is shown in **Fig. 3-10**.

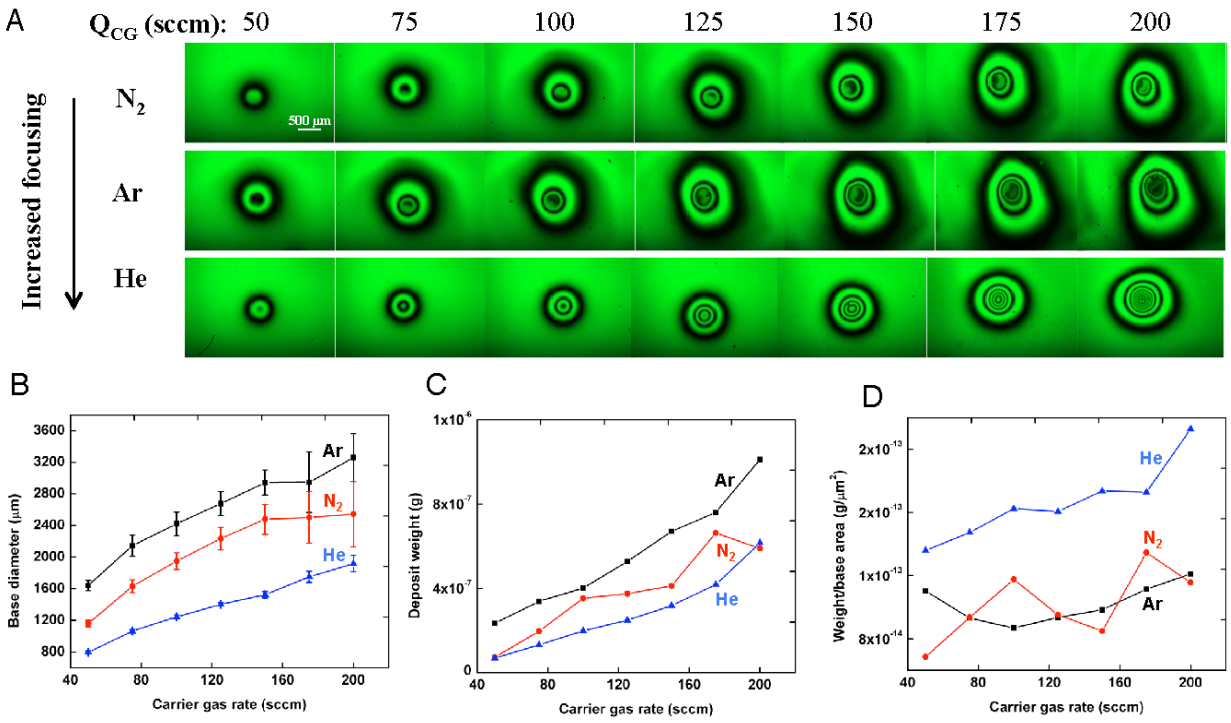

Figure 3-10 Effect of carrier gas type on deposit profile
Deposition conditions: '*s*'=0.5 mm, Q_{GF}=0 sccm, T_{Ev} = 330°C, T_s = 25°C. A: deposits images. B: deposits base diameter vs. carrier gases rates. C: Deposits weight vs. carrier gas rates. D: deposit weigh/base area for different carrier gases.

For all carrier gases the deposit spread is increasing with carrier gas flow rate (**Fig. 3-10b**). Since higher flow rate is associated with higher momentum of carrier molecules, both horizontal and vertical momentum are increasing, scattering the organic molecules outwards the center. Deposit weight is increasing with carrier gas rate, meaning that system is operating in "equilibrium" evaporation regime. (*9*) Since argon is the heaviest gas, it provides highest vertical and horizontal momentum to the organic molecules, resulting in highest deposit weight but also highest spread (**Fig. 3-10c**).

Carrier gas type has tremendous effect on deposit shape for OVJP operating at atmospheric pressure. For carrier gases Ar vs. N_2 the pattern spread ratio is ~x1.4, Ar vs. He and N_2 vs. He are ~x2 and ~x1.5, respectively. Interestingly, in case of helium not only deposit base diameter is

significantly lower, but also weight/deposit area is x2 times higher than for other gases. This is most probably a result of high diffusivity of organic molecules within helium stream and lower momentum which prevents from them to escape into surrounding ambient gas.

3.2.5 Guard flow gas in GF-OVJP

The effect of guard flow gas is demonstrated in **Fig. 3-11**. In this case helium was used as carrier gas.

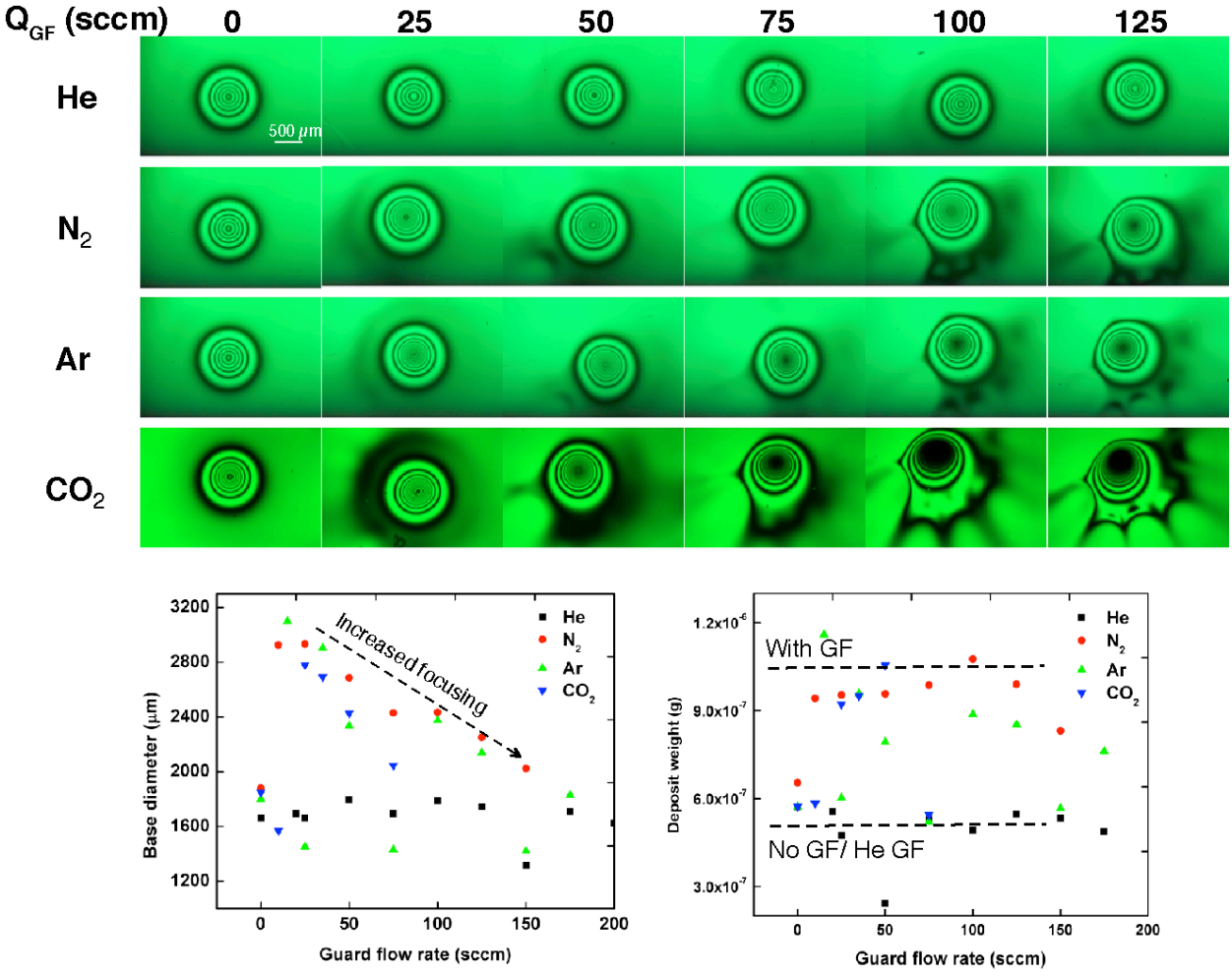

Figure 3-11 Effect on guard flow gas on deposit profile
Deposition conditions: '*s*'=0.5 mm, Q_{CG}=50 sccm, T_{Ev} = 330°C, T_s = 25°C.

At low guard flow rates (Q_{GF}/Q_{CG}~1), introduction of guard flow does not improve the resolution of the deposit. The reason for that is diffusivity of molecules from carrier into guard flow gas and low carrier gas vertical velocity. The surrounding guard flow triggers additional horizontal and vertical collisions, "bouncing" the organic molecules outside the carrier gas and provides them with horizontal momentum to diffuse along the substrate. When guard flow rate becomes substantially higher, vertical momentum of the guard molecules becomes high enough so that on one hand, some of the molecules are scattered outwards the center due to turbulence of the flow near the substrate, but the inner part of the deposit becomes substantially more collimated (the inner part of deposit becomes "squeezed"), especially for Q_{GF}/Q_{CG} >2. In case CO_2 used as guard flow, the collimation is further enhanced by Joule - Thompson effect, where the temperature drop of expanding CO_2 gas causes more molecules to condense in the center of the deposit. In all cases deposits weight becomes significantly higher (>2 times) with introduction of guard flow gas since additional vertical momentum provided by guard flow gives high enough kinetic energy to perimeter organic molecules to arrive to substrate. For patterning applications the effect of guard flow can potentially be improved if additional outer exhaust would be introduced, preventing from perimeter molecules to condense around the deposit. A simulated example of such setup will be presented in the following section.

3.3 Modeling of OVJP system

In the previous sections we have shown the effects of various deposition conditions on deposit shape. Although some understanding on the various effects of control parameters exists, obtaining the full map of control parameters in OVJP system experimentally would require enormous time- and energy- consuming effort. Modern computational tools enable full modeling

of complex physical systems in a comprehensive and user-friendly manner. Here we model OVJP using Comsol Multiphysics 5.1® finite element analysis software.

In order to define the flow regime in OVJP system, Knudsen number (*Kn*) needs to be considered. *Kn* defined as:

$$Kn = \frac{\lambda}{l} \quad (3.7)$$

where l is a characteristic length of a system. In case of OVJP system at atmospheric pressure, λ~150 nm, characteristic length is ~0.4 mm (nozzle diameter) and $Kn \ll 1$. The conditions in OVJP can therefore be treated as a continuum flow. The velocity at nozzle exit is ~100 m sec^{-1}, with Reynolds (*Re*) number is ~2000, signifying transient flow regime. The turbulence intensity I_T in this case is 0.05. To simulate turbulence, k-epsilon (k-ε) model with turbulence length scale of 0.1 mm and reference velocity scale of 1 m sec^{-1} was used. (*10*) Since molar fraction in the jet is <1%, the organic solute is highly diluted, and the mass transport of organic species won't significantly affect the fluid flow. The carrier gas flow can then be described by steady state equations for a compressible Newtonian fluid (*11*) :

$$\vec{\nabla} \cdot (\rho \cdot \vec{v}) = 0 \quad (3.8)$$

$$\rho(\vec{v} \cdot \vec{\nabla})\vec{v} = -\vec{\nabla}p + \vec{\nabla} \cdot \left[\mu(\vec{\nabla}\vec{v} + (\vec{\nabla}\vec{v})') - \frac{2}{3}\mu(\vec{\nabla} \cdot \vec{v})I \right] + \rho\vec{g} \quad (3.9)$$

$$\rho C_p \vec{v} \cdot \vec{\nabla}T = \vec{\nabla} \cdot (k\vec{\nabla}T) \quad (3.10)$$

where ρ, $\vec{v}$, p and T are the carrier gas density, velocity, pressure and temperature, respectively. μ, C_p, and k are the carrier gas dynamic viscosity, isobaric specific heat, and thermal conductivity, respectively. $\vec{g}$ is acceleration of gravity and I is the identity matrix. In the dilute

binary gas flow, mass transfer of organic species is calculated assuming steady-state mass balance (*12*) :

$$\vec{\nabla} \cdot (\vec{v}c) = \vec{\nabla} \cdot [D\vec{\nabla}c + \alpha c D \ln(T)] \quad (3.11)$$

Where D is diffusion coefficient of the organic species calculated from Eq. 3.5. Diffusion coefficient is calculated for each element in the system according to temperature of the element. In Comsol Multiphysics software we use turbulent fluid dynamics flow module combined with thermal transport module and mass transport module. This enables solving thermal, mass and fluid transport equations simultaneously enabling monitoring temperature, velocity, pressure and concentrations profile. Since nozzle is circular, axysimmetrical geometry can be used instead of full 3-dimensional model. This substantially saves memory consumption and convergence time during the calculation. **Fig. 3-12** demonstrates an example of geometry definition in the system.

Parameters	Constant
Nozzle material	Quartz
Organic material	Alq_3
Substrate material	Silicon
Stage temperature- T_{stage}	5°C
Nozzle temperature- T_{nozzle}	300°C
Carrier gas type and flow	He, 100 sccm
Guard gas type	Ar, 0 sccm
Concentration of organic in the carrier- C_{Org}	1% Molar
Carrier gas flow- Q_{CG}	100 sccm
Guard gas flow- Q_{GF}	10 sccm
Carrier inlet radius- Rin_{CG}	90µm
Carrier outlet radius- $Rout_{CG}$	90µm
Guard inlet diameter- Rin_{GF}	50µm
Guard outlet diameter- $Rout_{GF}$	50µm
Carrier gas- nozzle separation- h_{CG}	1 mm
Guard gas- nozzle separation- h_{GF}	1 mm
Outer guard flow wall thickness- $Rwall_{GF}$	100 µm
Carrier flow to guard flow distance- $Rwall_{GF}$	210 µm
Guard flow deviation angle – α	72 °
Substrate thickness - $h_{substrate}$	0.5 mm
Stage thickness - h_{stage}	1 mm
Calculated range - R_{calc}	3mm

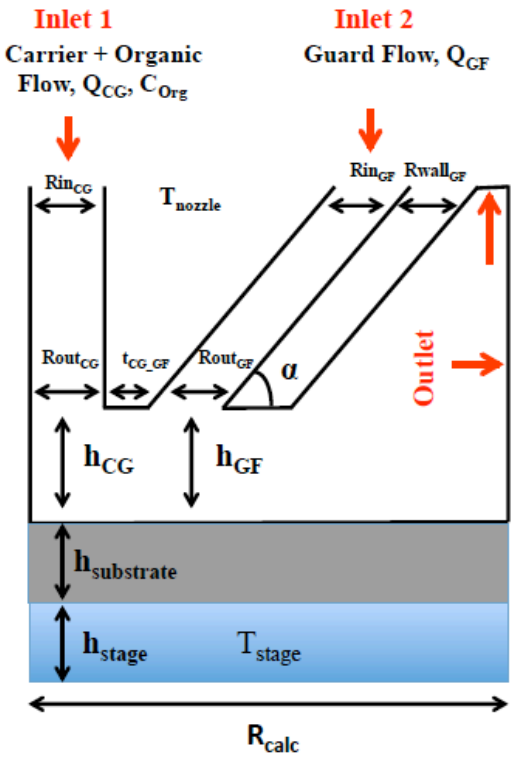

Figure 3-12 Example of geometry setup for simulation

Each of the geometry parameters is defined as variable that can be changed. This way "parametric sweep" can be performed during calculation, testing the effect of a given parameter or a combination of parameters. Inlets, outlets and nozzle walls are defined as boundary conditions.

In order to obtain meaningful results, the element mesh size is at least three times smaller than size of adjacent boundary (to enable at least two data points within a boundary). For instance, if the nozzle diameter is 200 µm, element mesh size is maximum ~50 µm in that region. An additional important aspect is correct definition of boundary conditions and computational space size. An example of simulation results is shown in **Fig. 3-13**. In this case parameters used are from **Fig. 3-12**.

The gas outlet is defined as open boundary at ambient pressure with zero concentration of organic species. Computational size R_{calc} in the simulation is 3mm (~ 4 times larger than nozzle outer diameter). R_{calc} should be chosen so that computational time and memory usage is reasonable, and data about spread of organics within the system is fully captured. Assuming sticking coefficient of 1, concentration of organic molecules in a vicinity to substrate is assumed to represent the resulting deposit profile. In current work the concentration profile was extracted at distance of '*s*'/ 100 above the substrate (for instance10 μm for '*s*'=1mm).

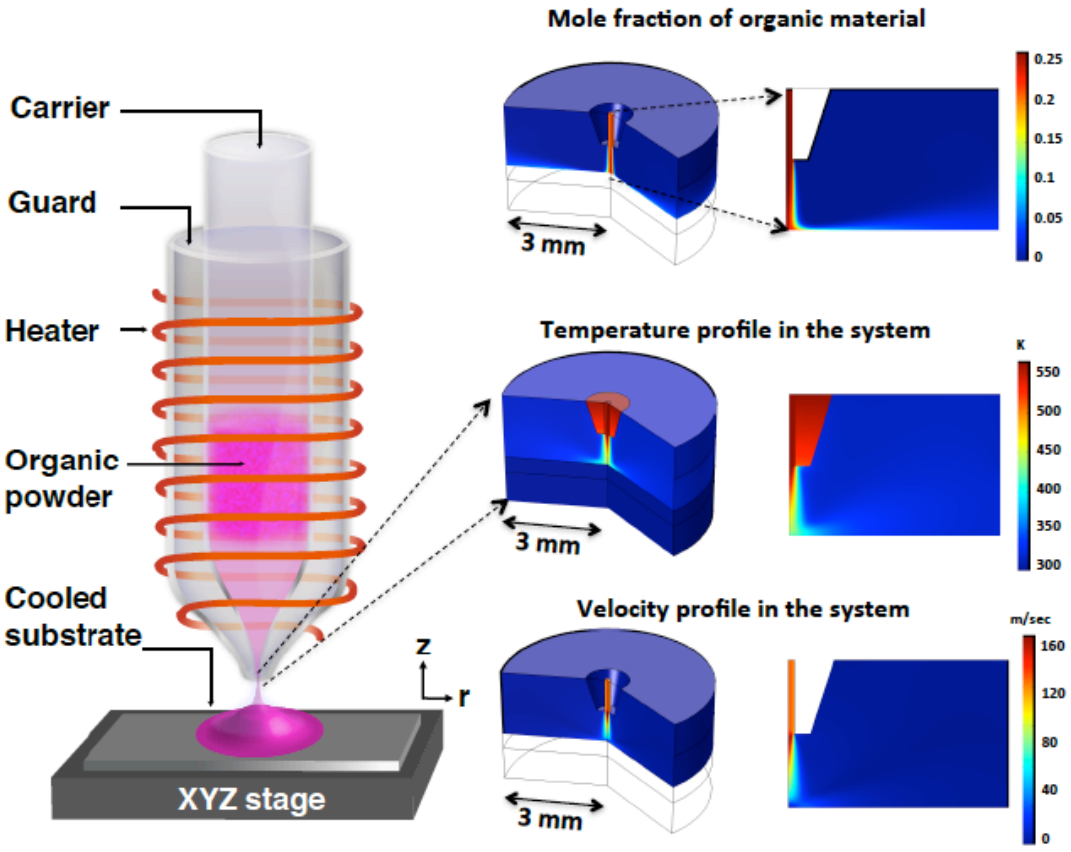

Figure 3-13 Example of simulation result

In order to confirm agreement between simulation and experimental results, effect of substrate-nozzle separation distance was tested. Geometry used was identical to experimental nozzle

geometry. Simulation results are demonstrated in **Fig. 3-14**. Optimum focusing of the deposit is obtained at separation ~0.8 mm. Below '*s*' of 0.8 mm, turbulence occurs near the nozzle exit, resulting in high organic concentration of organic molecules around the nozzle. Above 0.8 mm, velocity of impinging jet approaching 0 near the substrate, resulting in dilution of organic molecules above the substrate. In a similar manner, effects of carrier and guard flow combinations can be now studied computationally and further system improvements can be made.

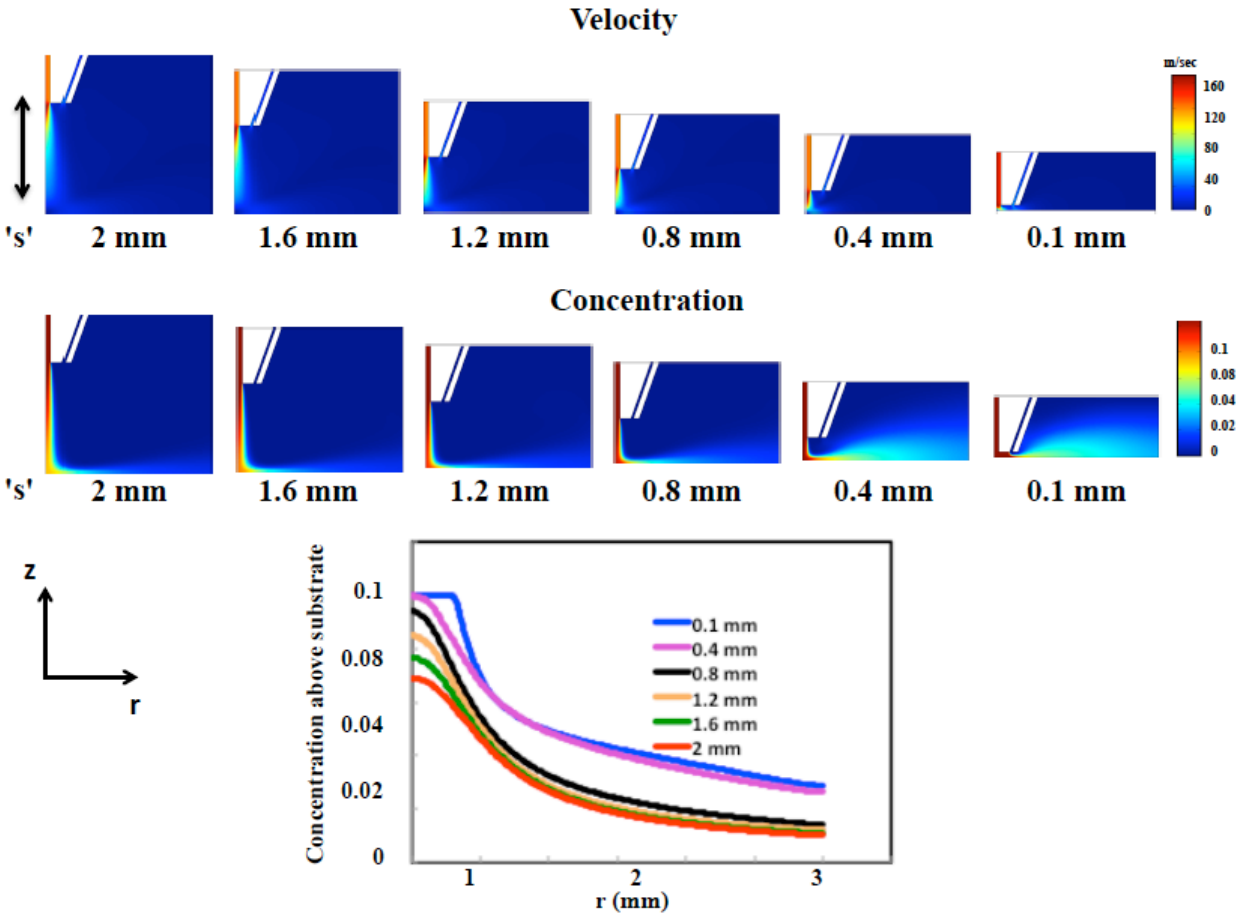

Figure 3-14 Effect of nozzle-substrate separation distance on deposit profile

In order to design a system aiming to maximize the printed pattern resolution for OLED applications, alternative evaporation systems setups were simulated. One example is using

exhaust at the nozzle outlet instead of guard flow. The proposed geometry is shown in **Fig. 3-15**.

Parameters	Constant
Nozzle material	Si
Organic material	Alq_3
Substrate material	Silicon
Stage temperature- T_{stage}	5°C
Nozzle temperature- T_{nozzle}	300°C
Carrier gas type and flow	He, 3 sccm
Concentration of organic in the carrier- C_{Org}	1% Molar
Carrier gas flow- Q_{CG}	100 sccm
Carrier inlet radius- Rin_{CG}	30 µm
Carrier outlet radius- $Rout_{CG}$	9 µm
Exhaust inlet diameter- Rin_{GF}	16 µm
Exhaust outlet diameter- $Rout_{GF}$	16 µm
Carrier gas- nozzle separation- h_{CG}	10 µm
Exhaust- nozzle separation- h_{GF}	1 mm
Outer guard flow wall thickness- $Rwall_{GF}$	16 µm
Carrier flow to guard flow distance- $Rwall_{GF}$	16 µm
Substrate thickness - $h_{substrate}$	0.5 mm
Stage thickness - h_{stage}	1 mm
Calculated range - R_{calc}	300 µm

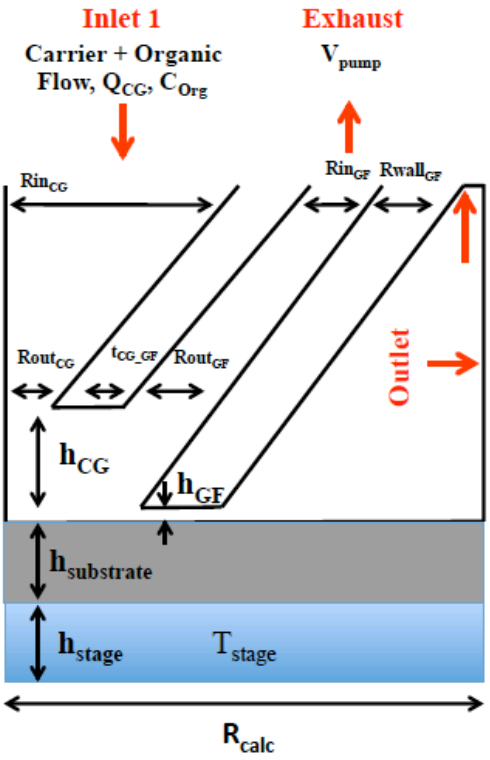

Figure 3-15 Miniaturized OVJP system with exhaust geometry

The exhaust pumping speed can be adjusted so that maximum concentration of organic molecules will be obtained between substrate and nozzle and at the same time pump out the escaping perimeter molecules. Using miniaturized OVJP system with exhaust can potentially obtain sub- micron deposit profiles. **Fig. 3-16** demonstrates the effect of pumping speed on velocity and concentration profile in the system. At 10 m sec^{-1} pumping speed, optimal velocity profile is obtained - organic molecules are concentrated precisely under the nozzle. At lower

speed, molecule dispersed outside and at higher speed extra ambient molecules are pumped.

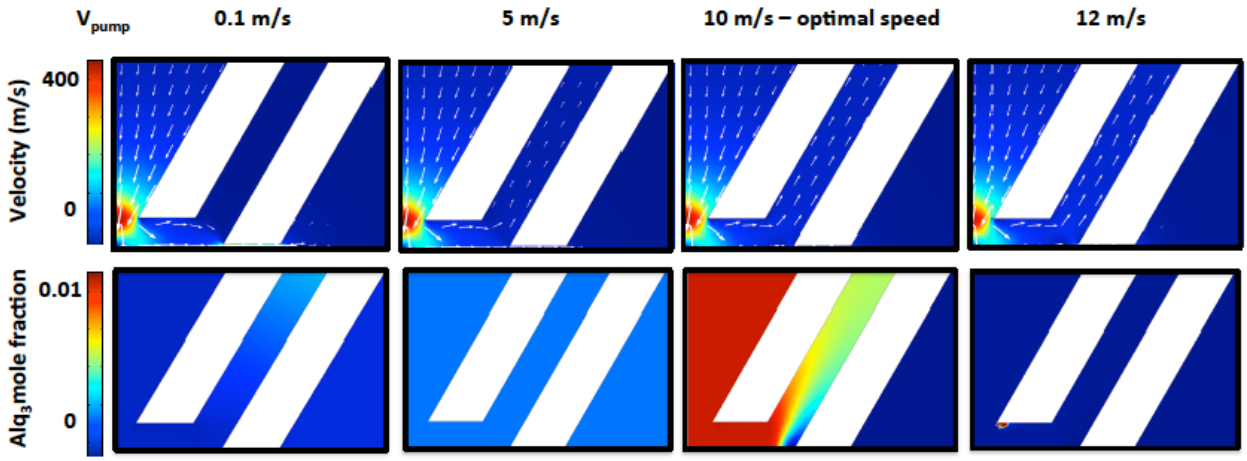

Figure 3-16 Effect of exhaust pumping speed on velocity and organic molecules concentration

This setup can be further improved by adjusting the height of carrier gas nozzle height, h_{CG} (**Fig. 3-13**), as demonstrated in **Fig. 3-17**. At h_{CG}=30 µm sharp rectangular deposit shape of <40 µm can be obtained.

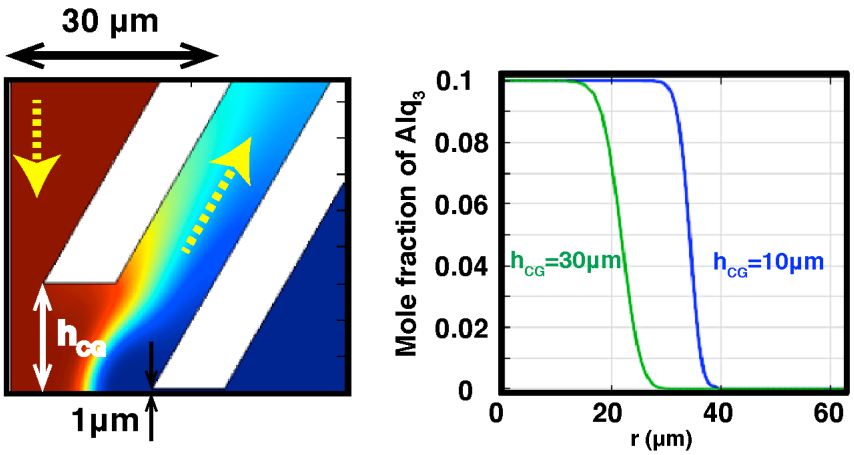

Figure 3-17 Effect of carrier gas nozzle- substrate separation distance in exhaust OVJP setup on deposit profile

Additional example for further improvement is usage of alternative nozzle geometries. For instance, in order to improve conductance of molecules through the nozzle, curved nozzle

geometry can be used (**Fig. 3-18**). Combining the geometry with exhaust from previous example, further decrease in deposit size and sharpness can be obtained, with pixel size of less than 40 µm. This pixel size is comparable to modern 200-400 pixel per inch (PPI) (e.g. Retina) high definition displays (*13*).

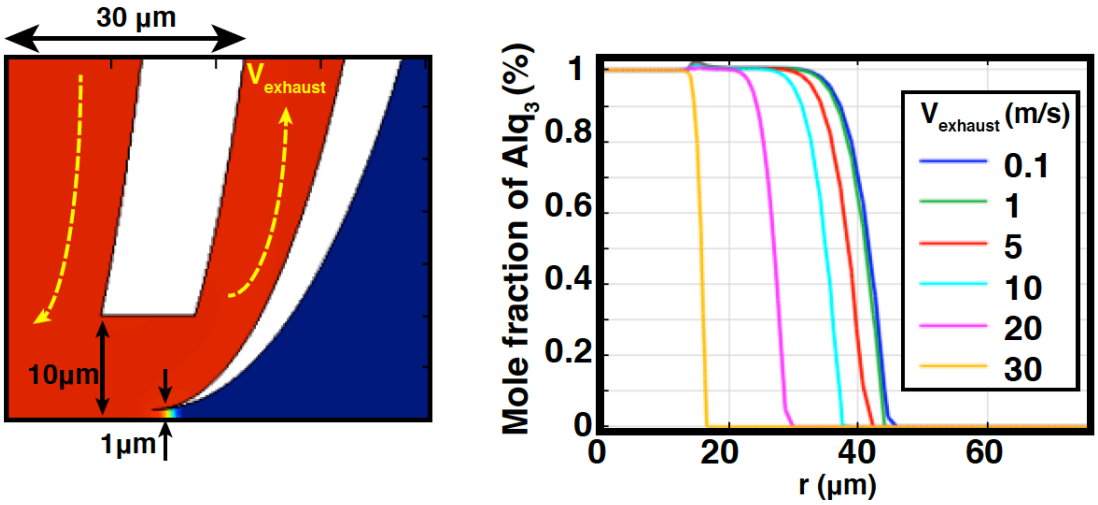

Figure 3-18 Effect of curved nozzle geometry on deposit profile in exhaust OVJP setup

3.4 Summary

In this chapter we studied how additive, mask and vacuum-free patterning of small molecular organic films can be achieved using OVJP and GF-OVJP, and how pattern resolution depends on process parameters. The relationship between deposition duration and amount of material on the substrate is linear, meaning that the deposition is convection controlled; understanding the flow fields is critical to predicting the deposited pattern shape. The nozzle-substrate separation distance is an important parameter in jet printing. Closer is not always better; choosing the correct separation distance during printing can improve the resolution by 40%. Increase in carrier gas flow rate increases the deposition rate, meaning that material evaporation at the source is limited by convection rather than diffusion from the source into the gas stream. Although deposition rate is increased, the spread of material is increased as well. This trade-off can be

broken by introducing lighter carrier gas, such as helium. Increasing the guard flow rate doubles the deposition rate, focusing the diverging organic molecules onto the substrate, but also introducing turbulence at the perimeter of the deposit. The strongest focusing is observed for CO_2 as guard flow gas, due to its both highest molecular weight and larger collision cross-section compared to Ar and N_2.

Full simulation of OVJP and GF-OVJP setup was built in order to further optimize system parameters. Microns-scale resolution was demonstrated by miniaturizing system size and introducing exhaust OVJP with curved nozzle geometry.

3.5 References

1. S. Biswas, K. P. Pipe, M. Shtein, Solvent-free, direct printing of organic semiconductors in atmosphere. *Applied Physics Letters* **96**, 263301 (2010).
2. S. Biswas *et al*., Spatial Mapping of Morphology and Electronic Properties of Air-Printed Pentacene Thin Films. *Advanced Functional Materials* **24**, 3907 (2014).
3. M. Shtein, P. Peumans, J. B. Benziger, S. R. Forrest, Direct mask-free patterning of molecular organic semiconductors using organic vapor jet printing. *Journal of Applied Physics* **96**, 4500 (2004).
4. S. Biswas, Guard Flow-enhanced Organic Vapor Jet Printing of Molecular Materials in Air, Thesis, The University of Michigan, (2014).
5. G. J. McGraw, S. R. Forrest, Fluid dynamics and mass transport in organic vapor jet printing. *Journal of Applied Physics* **111**, 043501 (2012).
6. E. Bitziou, N. C. Rudd, M. A. Edwards, P. R. Unwin, Visualization and Modeling of the Hydrodynamics of an Impinging Microjet. *Analytical Chemistry* **78**, 1435 (2006).
7. M. Shtein, P. Peumans, J. B. Benziger, S. R. Forrest, Direct, Mask- and Solvent-Free Printing of Molecular Organic Semiconductors. *Advanced Materials* **16**, 1615 (2004).
8. G. J. McGraw, High Resolution Organic Vapor Jet Printing of Phosphorescent Organic Light Emitting Diode Arrays, Thesis, The University of Michigan, (2013).
9. M. Shtein, H. F. Gossenberger, J. B. Benziger, S. R. Forrest, Material transport regimes and mechanisms for growth of molecular organic thin films using low-pressure organic vapor phase deposition. *Journal of Applied Physics* **89**, 1470 (2001).
10. N. Zuckerman, N. Lior, Jet impingement heat transfer: physics, correlations, and numerical modeling. *Advances in heat transfer* **39**, 565 (2006).
11. R. B. Bird, W. E. Stewart, E. N. Lightfoot, *Transport Phenomena*. Wiley (2007).
12. K. F. Jensen, E. O. Einset, D. I. Fotiadis, Flow Phenomena in Chemical Vapor Deposition of Thin Films. *Annual Review of Fluid Mechanics* **23**, 197 (1991).
13. https://www.noteloop.com/kit/display/pixel-density/

Chapter 4
Growth Mechanisms of Small Organic Molecules in OVJP

4.1 Introduction

Micro- and nano-structures based on small molecular materials have many promising applications: in optoelectronic devices with unique charge and light transfer properties (*1-3*), in sensors, and in the pharmaceutical (*4*) and food industries. Among vapor-based film growth techniques, vacuum thermal evaporation (VTE) is one of the most widely implemented method to fabricate small molecular organic thin films. In this method the material is evaporated from a resistively heated boat under high vacuum ($<10^{-7}$ Torr). (*5*) The evaporated molecules are ballistically transported to the substrate where they are adsorbed through van der Waals forces. In well-controlled conditions, quasi-epitaxial growth can persist for several monolayers, after which strain relaxation results in pronounced stacking defects. (*6*) Most of the organic thin film growths by VTE result in amorphous or nano-crystalline morphologies, while the substrate is usually heated in order to enhance crystallinity. Substrate templating involves using thin crystalline films of small molecular organic materials (*7, 8*) or thin membranes of grapheme (*9*) as seed layers. The degree of vapor saturation of organic material at the substrate is an important parameter that determines film morphology. Zhao et al., for instance, have demonstrated the

growth of single crystal Alq_3 nanowires using adsorbent-assisted physical vapor deposition, where degree of saturation of Alq_3 can be controlled *via* adsorbents in the vapor phase. (*10*) Huang et al. *(11)* developed a method for the micropatterned growth of iron phthalocyanine (FePc) nanofiber arrays using VTE by controlling the surface energy and temperature of the substrate, where a grain-like (in-plane) morphology was obtained on Si surfaces (higher surface energy) and a fiber-like (out-of-plane) morphology was obtained on Ag surfaces (lower surface energy) within a certain range of substrate temperatures. Chiu et al. *(3)* have used a vapor condensation method for the growth of Alq_3 nanowires.

In OVPD, the crystalline domain size is controlled by adjusting the substrate temperature, carrier gas flow rate and chamber pressure. (*12*) Using this method, Yang et al. (*1*) showed controlled growth of ordered bulk heterojunction photovoltaic cells, where the electron donor layer of copper phthalocyanine (CuPc) exhibited a continuous wetting layer, with short needle-like crystals grown on top (**Fig. 4-1**).

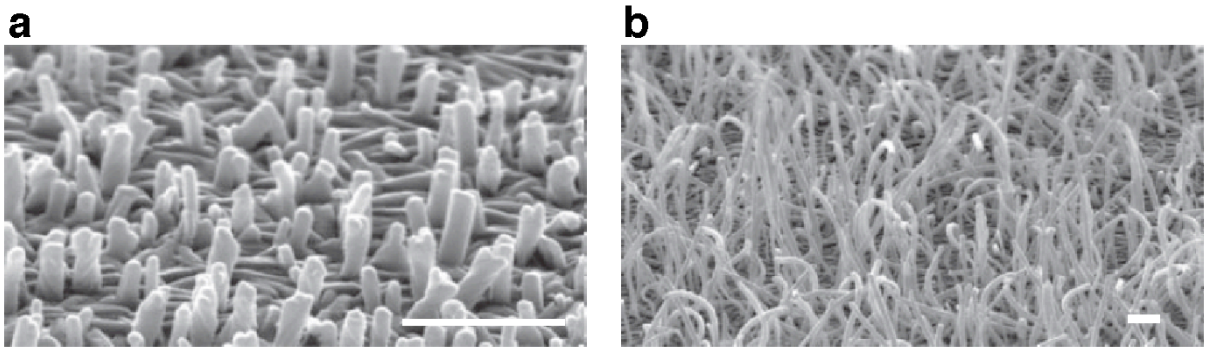

Figure 4-1 SEM and atomic force microscope (AFM) images of CuPc films grown in OVPD
(A) Surface of a CuPc film with a continuous wetting layer plus short needle-like crystals grown on a silicon wafer surface by organic vapour phase deposition (OVPD). (B) Surface of a CuPc film grown on ITO-coated glass substrate. (*1*)

OVJP deposition approach is particularly interesting for a broad set of applications, not only because of the additional morphological control, (*13-16*) but also due to its ability to generate

relatively thick (>500 nm) and large area deposits, while also enabling additive patterning with high materials utilization efficiency.

Spherical nanoparticles are useful building blocks in many fields, including photonics, (*17*) pharmaceuticals, surfaces with controlled wettability, (*18, 19*) and others. Challenges in scaling up and broadening their applications include the limited set of materials from which they have been made, and the ability to directly attach these particles to any desired surface. Achieving sphere-like morphologies using small molecular compounds is nearly impossible using common techniques, such as precipitation from solution (*10*), aerosol coating (*20*), or vacuum thermal evaporation. The traditional methods either yield smooth amorphous or faceted crystalline particles.

Here we use GF-OVJP to generate the growth of variable aspect ratio micro-features that are attached to the substrate and exhibit crystallinity without faceting. Below we describe some of the growth modes and propose a model that can quantitatively predict surface morphology in small molecular organic films. We demonstrate the growth of continuous, non-faceted, crystalline nano-spheroids of archetypal small molecular organic semiconductor compounds-boron subphthalocyanine chloride (SubPc) and tris (8-hydroxyquinolinato) aluminum (Alq_3). Using a surface evolution framework of small molecular organic film growth, we present an analytical model to describe the highly kinetic and thermal aspect of GF-OVJP deposition. The model incorporates the thermophysical, structural and mechanical properties of the materials, and is validated by observed morphologies. It can be used to predict nano-structured morphologies in films of different materials with known thermo-physical and mechanical properties.

4.2 Experimental setup

4.2.1 Film fabrication and process parameters

All organic materials were purchased at sublimed grade purity from Luminescence Technology Corp. and deposited with no further purification. SubPc, Alq_3, PTCDA were sublimed grade. All samples were deposited on Si (100) wafers. These were cleaned by ultrasonication in detergent solution and deionized water followed by heated acetone, trichloroethylene, and isopropanol for 10 min each. Substrates were then placed in boiling isopropanol for 5 min, dried in pure nitrogen gas prior to film deposition. In order to check the effect of Si substrates orientation and remove native silicon oxide, the substrates were etched in hydrofluoric acid (HF) for 2 min prior to deposition.The GF-OVJP nozzles used in this study were constructed from two coaxial glass tubes of 0.5" and 0.75" outer diameters, fused at one end and pulled at the other to form concentric nozzle tips of 200 μm and 700 μm internal diameters. The inert carrier gas and evaporated organic were transported through the inner tube. The inner gas used was 99.99% pure nitrogen. The annular channel for the guard jet was found to be 100 μm wide and angled at $\alpha \sim 15$ ° from the nozzle axis. The nozzle was cleaned with solvents, dried and wrapped with 36-gauge heavy insulated tape heater (Omega Engineering, Inc.) with a power density of 8.6 $W \cdot in^{-2}$. The heating tape leads were connected to a temperature controller (Digi-Sense Benchtop temperature controller, Cole-Palmer Instruments Co.) and a 1/16" K-type thermocouple was used to maintain the temperature of the source. The source consisted of ~0.15 g of powder sandwiched between quartz wool and placed in the heated source section of the inner tube. The carrier gas and guard jet flow rates were maintained using mass flow controllers (C100 MFC, Sierra Instruments). The process parameters, that were kept constant are nozzle- substrate separation distance- 1mm,

substrate temperature- 20 °C, carrier gas flow rate - 100 sccm, and guard gas flow rate- 200 sccm. The process was performed in glove box purged with 99% pure nitrogen.

4.2.2 X-RAY measurements

For all x-ray measurements, standard timescans (*in-situ*) or *2θ* scans (*ex-situ*) were taken in the vertical scattering plane with a PILATUS 100K pixel detector. *In-situ* x-ray diffraction experiments were conducted at the beamline X21 (wiggler source) of the National Synchrotron Light Source (NSLS) at Brookhaven National Laboratory with10 keV x-ray energy. The detector was placed at a fixed *2θ* position, and the detector images were taken every second during the film growth (**Fig. 4-2**). The detector covers about 7° of *2θ* angular range with 0.02° resolution. The *ex-situ* measurements were carried out at Sector 13-BM-C (15 keV, bending magnet source) and Sector 33-ID-D (15 keV, undulator source) of the Advanced Photon Source (APS) at Argonne National Laboratory. X-ray reflectivity data was first measured with a typical *θ-2θ* scan to determine the critical angle for total external reflection, and full *2θ* scans were performed two times for each sample, with the x-ray incidence angle above and below the critical angle.

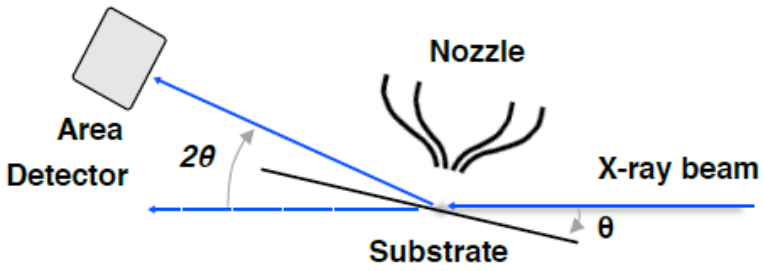

Figure 4-2 Schematic of the synchrotron based XRD experimental set up for *θ-2θ* measurements

4.2.3 Microscopy

FEI Nova 200 Nanolab scanning electron microscope with accelerating voltage of 5-10 kV and

current 0.1-0.5 nA was used to obtain the surface morphology images.

4.2.4 Thermal expansion coefficient measurements

Spectroscopic ellipsometry was used to measure the time dependent thickness changes exhibited by the samples when heating from room temperature to temperature, T, of 250 °C, at 1 °C/min, using a variable angle spectrometric ellipsometer (M-2000, J.A. Woollam Co.) equipped with an Instec heating stage. The measurements were performed at a fixed angle of 70°. The thickness and refractive index, were determined by fitting the acquired ellipsometric angles Δ and Ψ to a Cauchy/SiOx/Si model over the entire measured spectral range (wavelength range 400−1700 nm). During the experiments, the heating stage was purged using purified nitrogen gas to maintain an inert atmosphere and prevent oxidation, and a liquid nitrogen pump was used to maintain the temperature and cooling rates. Extrapolated linear fits were performed to amorphous and crystalline regions of SubPc to calculate the thermal expansion coefficient. (*21*)

4.2.5 Surface energy measurements of SubPc films

For surface energy measurements GF-OVJP deposited 100 μm film of SubPc was used. All contact angles were measured by advancing angle with about 2 μl of liquid onto the surface (Ramé-Hart 200-F1 goniometer). Water was used as a polar liquid for polar surface energy measurement and methyl iodide (CH_2I_2) was used as a non-polar liquid for dispersive surface energy measurement.

4.2.6 Modeling

COMSOL Multiphysics 4.3a software with fluid dynamics module was used for temperatures and flow profile, and mechanical module for stress calculations. For surface evolution modeling, Matlab_R2012b was used.

4.3 Experimental results

4.3.1Morphology evolution.

Subphthalocyanine chloride (SubPc) is an archetypal small organic material, commonly used as an electron donor material in organic photovoltaic cells. This molecule has a conical shape with an orthorhombic crystal structure in the bulk phase. **Figure 4-3** shows the surface evolution of SubPc grown on (100) silicon using GF-OVJP at a source temperature of 325 $^{\circ}$C. Smooth thin films are obtained up to a film thickness of ~ 200 nm, evolving into wavy, sinusoidal-like morphology upon further growth (**Fig. 4-3a**). Beyond a critical total thickness (~ 800 nm), the film evolves into a spheroidal, lobe-like morphology (**Fig. 4-3b-d**). From this point on, film thickness remains constant and only the lobes grow, eventually combining into ferns-like microstructures (**Fig. 4-3e,f**).

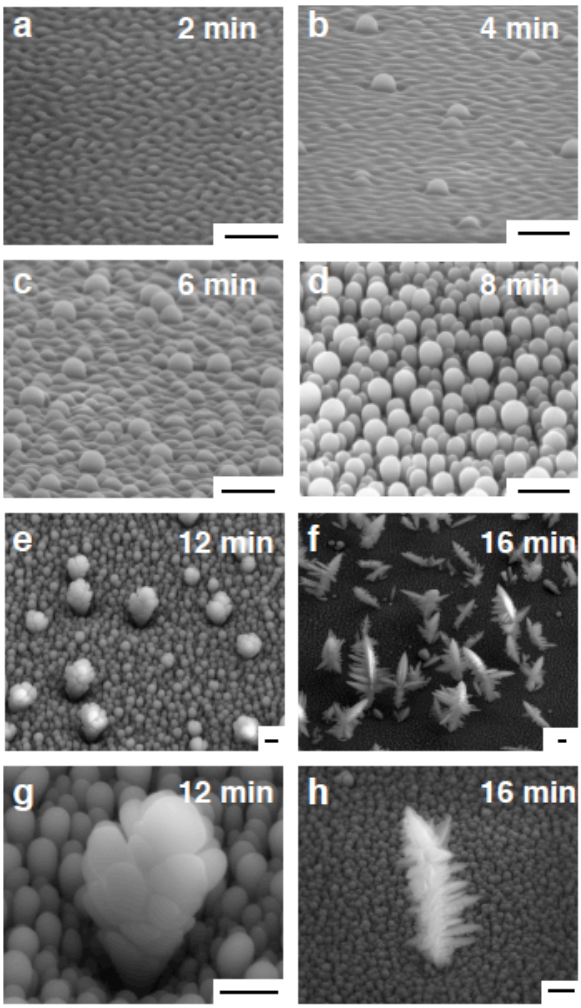

Figure 4-3 Surface evolution of SubPc film continuously grown by GF-OVJP
Dwell time durations of stationary nozzle above substrate as indicated on the figures: (A) 2min, (B) 4 min, (C) 6 min, (D) 8 min, (E) 12 min, (F) 16 min, (G) 12 min - enlarged, (H) 16 min-enlarged. Scale bar 1μm.

4.3.2 Effect of process conditions

To understand the role of vapor saturation on growth kinetics and morphology, the source temperature was varied, while keeping all the other process parameters constant (**Fig. 4-4**).

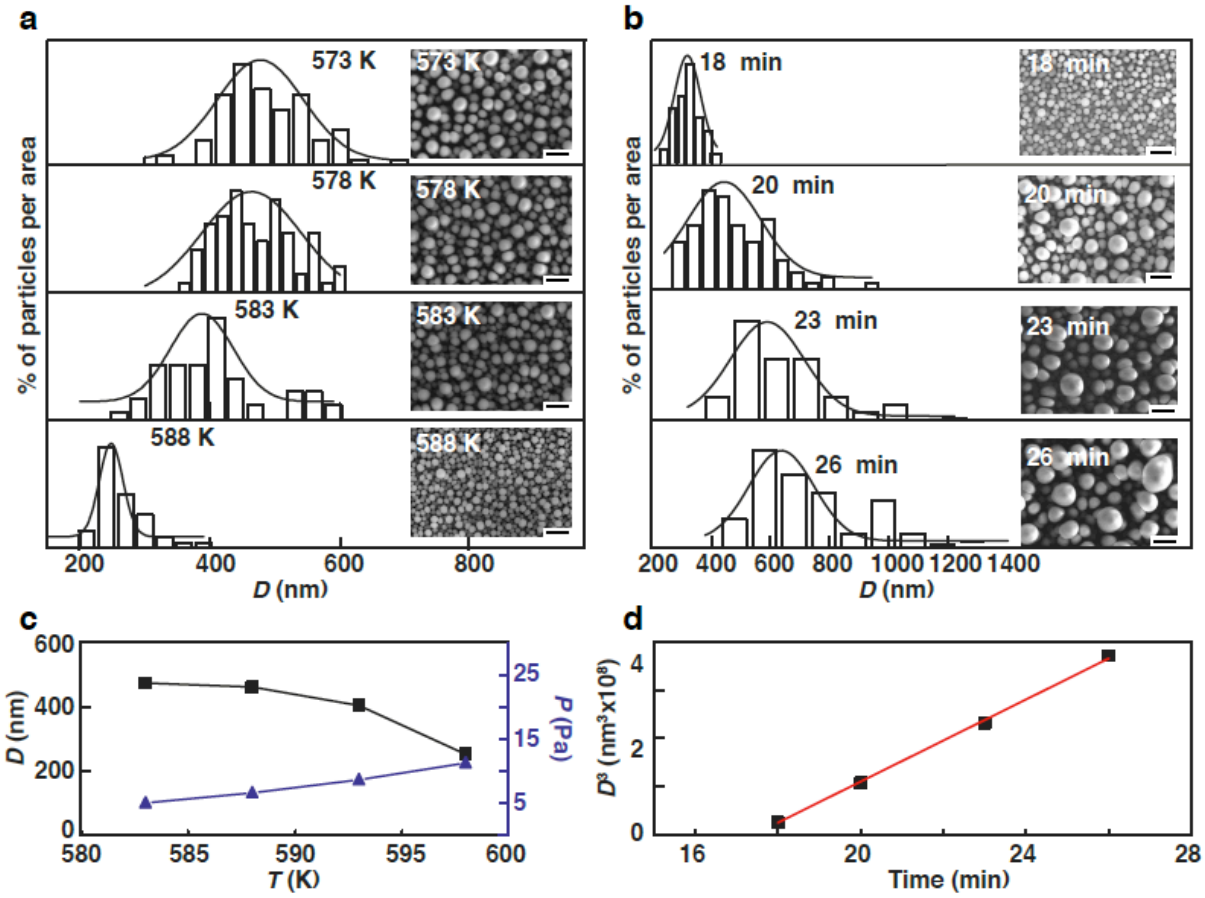

Figure 4-4 Morphology control in GF-OVJP
(A) Distribution of lobe diameters for different source temperatures. Scale bar 1μm. (B) Distribution of lobe diameters with time. Scale bar 1μm. (C) Effect of temperature on average lobe diameters and partial pressure of the evaporating molecules *P* (Pa) near the material source. (D) Lobe coarsening process plotted as cube of average lobe diameter vs. time (black datapoints) with linear fit (red line).

The resulting mean lobe diameter and diameter distribution width (**Fig. 4-4**) decrease with an increase in source temperature. As evaporation source temperature increases, the partial pressure and concentration of organic material in the carrier gas jet increases; nucleation density (or number of nuclei per unit area) increases, in turn, with the concentration of organic admolecules. These denser nucleation sites act as surface perturbations, and therefore, promoting smaller and more uniform lobe formation with higher source temperature. These trends are shown clearly in **Fig. 4-4c**. Further growth results in coarsening of the lobes, as shown in **Fig. 4-4b**. In this case,

the experiment was performed at a constant temperature of 310 °C, while the nozzle dwell time was varied. The coarsening can be explained by an Ostwald ripening mechanism (**Fig. 4-4d**), where large particles grow at the expense of smaller particles. In this case, there is a linear relation between the average particle diameter cubed and time, similarly to what is expected by Ostwald theory. (*22*) According to classical Ostwald theory the average particles radius is as follows (*23*):

$$\langle R \rangle^3 - \langle R \rangle_0^3 = \frac{8\gamma c_\infty v^2 D}{9 R_g T} t \quad (4.1)$$

where: $\langle R \rangle$- average particle diameter (m), γ- particle surface energy (j m^{-2}), c_∞- solubility of particle material (mole m^{-3}), v- molar volume of particle material (m^3 $mole^{-1}$), D- diffusion coefficient of the particle material (m^2 sec^{-1}), R_g- ideal gas constant (J $mole^{-1}$ K^{-1}), T- temperature (K), t- time (sec). Classical Ostwald theory states that diameter cube is proportional to $1/T$ and t. For the material system and process described here, Ostwald ripening is happening simultaneously with growth due to continuous deposition from the vapor phase. Consequently, the lobe size evolution mechanism is more complex than what is dealt with in the classical Ostwald ripening theory, i.e. particles size changes at constant system volume.

4.3.3 X-ray diffraction

In situ X-ray diffraction (XRD) reveals that the films are polycrystalline throughout the growth (**Fig. 4-5a**).

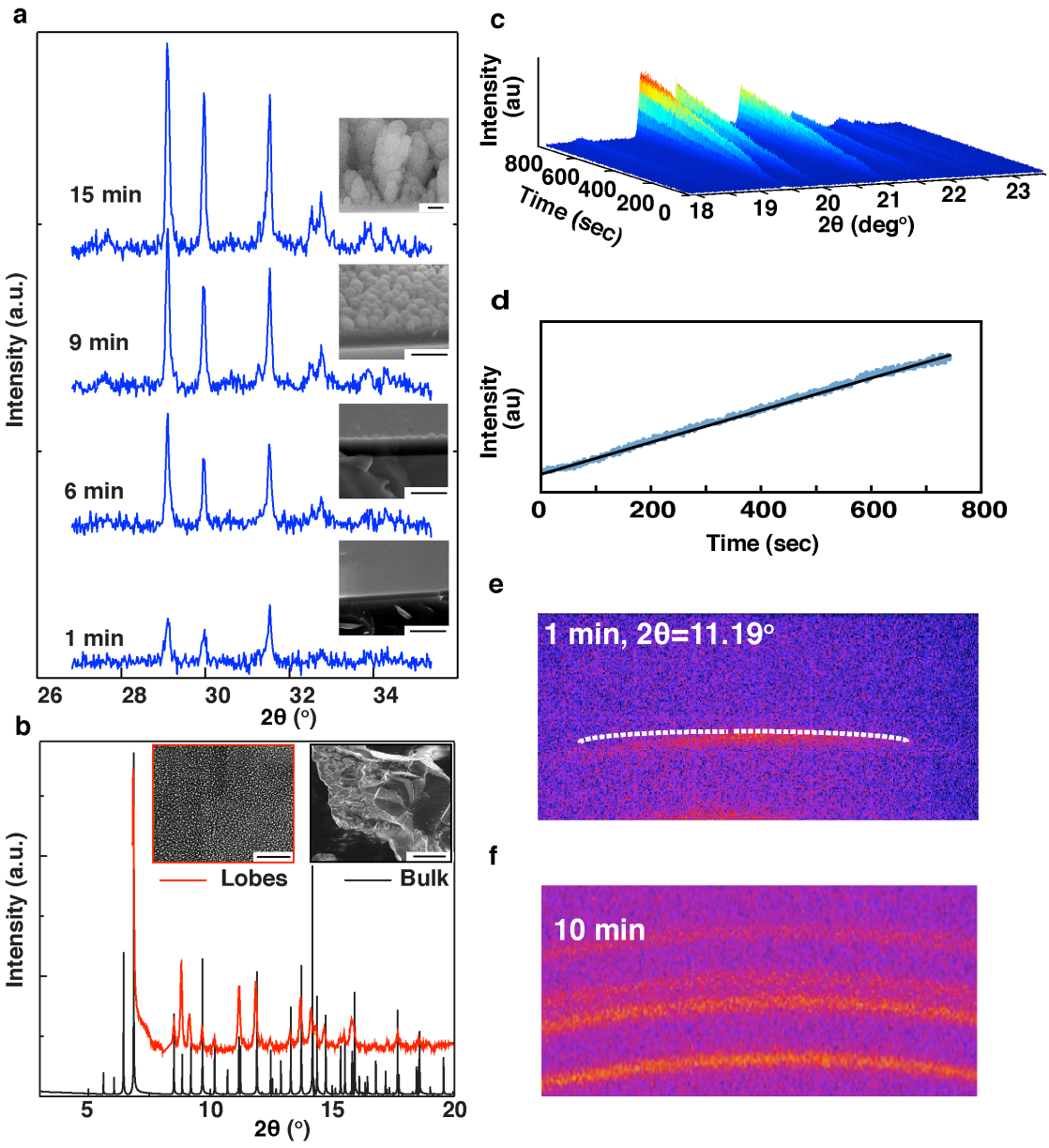

Figure 4-5 XRD of SubPc deposits

(A) *In-situ* XRD measurement during the SubPc film growth showed that the diffraction peak intensities continuously increase as a function of film thickness, regardless of the morphology of the film surface (smooth, wavy, lobes, ferns). Diffraction intensity data at four different film thicknesses (nozzle dwell time: 1, 6, 9, 15 min) are shown, and the SEM image insets describe the morphology of the film surface at each growth stage. Scale bar 1μm. (B) Full 2θ scan of deposit with lobe microstructure (red curve) and simulated powder diffraction pattern from its bulk structure [24] (black curve) showing good agreement between their peak positions. Inset depicts the micrographs of SubPc bulk powder and deposit. Scale bar 10 μm. (C) Full in-situ scan of spot deposited film for 800 sec at 325 °C source temperature. Peak intensities are increasing linearly with time; (D) Example of integrated peak intensity vs. time at 2θ =19.37°

peak; (E) An area detector image of ex-situ full scan for spot-deposited thin film deposited with 1min dwell time. In this case the film obtained shows smooth surface morphology, and some preferential growth is observed (non-uniform intensity distribution along the arc); (F) An area detector image for spot-deposited thin film deposited with 10 min dwell time. In this case polycrystalline lobes are formed without preferred orientation (arcs with uniform intensity distribution).

The linear dependence of peak height on growth time (**Fig. 4-5a-d**) indicates that the lobes, as well as the wetting layer are polycrystalline, and the degree of crystallinity does not change. *Ex situ* XRD was performed with the x-ray incidence angle below the critical angle (~ 0.1°) of the film containing the lobe structures (**Fig. 4-5b**), such that the diffraction beam probes only the top 10 nm of the deposit. Powder rings with uniformly distributed intensity were observed, suggesting that the lobes are highly polycrystalline throughout, without any preferred orientation (**Fig. 4-5e,f**). The average size of crystals is calculated to be approximately 50 nm using Scherrer's equation (*25*), while the lobes are approximately 500 nm in diameter, indicating that each lobe is comprised of number of crystallites. Measured peak positions are in very good agreement with those from reported bulk crystal structure of SubPc (*24*), indicating that the crystal structure of the film as well as that of the lobes is similar to that of bulk SubPc, which was used as the evaporation source material. Yet the lobes are non-faceted. This uncommon growth modality can be understood in part by considering the balance of driving forces in the thin film growth.

4.4 Discussion

Significant surface perturbations in the film arise beyond a thickness of 200 nm. Unlike other vapor based deposition methods, where the source of organic material is far from the substrate (usually 50 cm and more), in GF-OVJP, the jet temperature within 10 microns of the substrate reaches 200 °C.

The wave-like surface perturbations obtained here are reminiscent of Stransky-Krastanov growth, usually occurring in inorganic materials due to substrate-film crystal mismatch, which leads to the formation of quantum dots and nanorods (*26*). In the present case, the stresses originate from the thermal gradients within the film; therefore, significantly larger critical thicknesses are required to obtain the thermal stress needed to cause a 3-D surface formation. The evolution of a wavy surface instability into the observed spheroidal shapes depends on the balance between the energy relaxation of the thermally driven elastic strain in the film, and the energy cost of increasing the surface area, embodied by [1](*27*):

$$G = (\frac{\pi^2\gamma}{\lambda} - \frac{\pi\sigma^2}{Y})q^2 \quad (4.2)$$

where G is the body free energy of the system per wavelength (J m^{-1}); γ is the surface energy (J m^{-2}); λ is the surface waviness wavelength (m); Y is material's Young modulus (Pa); σ is the stress acting on the surface (Pa), and q is the amplitude of the perturbation (m). The perturbation is amplified when the wavelength λ exceeds a critical value, given by:

$$\lambda_c = \frac{\pi Y\gamma}{\sigma^2} \quad (4.3)$$

where λ_c is the critical wavelength beyond which the surface is no longer stable and three-dimensional growth occurs. For the SubPc system, the measured surface energy is 44.7 mJ m^{-2}; the estimated Young modulus (from other phthalocyanine materials) (*28*)is approximately 5 GPa. Thermal expansion measurement is shown in **Fig. 4-6**.

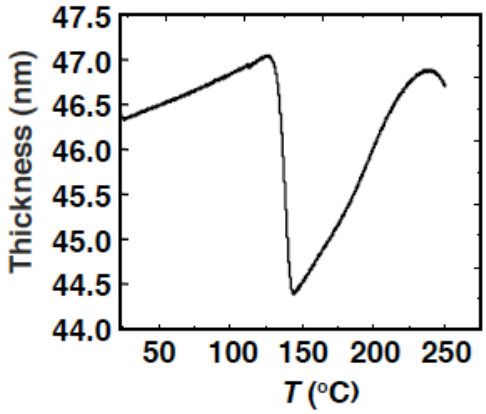

Figure 4-6 Thermal expansion of SubPc film
SubPc flat film deposited by VTE was used to determine thermal expansion coefficient. Thickness variation versus temperature for SubPc film was measured at 1 °C/min heating rate. Extrapolated linear fits were performed to amorphous and crystalline regions of SubPc to calculate the thermal expansion coefficient. Amorphous - crystalline transition of SubPc occurs at ≈150°C, as seen in the plot.

The thermal expansion coefficient of SubPc is 1.4×10^{-4} K^{-1} in the amorphous phase and 6.5×10^{-4} K^{-1} in the crystalline phase. For 800 nm film thickness, temperature differences both in-plane and out-of plane of the film can reach tens of degrees (**Fig. 4-7a,b**), resulting in thermal stresses acting on the surface being on the order of tens to hundreds MPa (**Fig. 4-7c**).

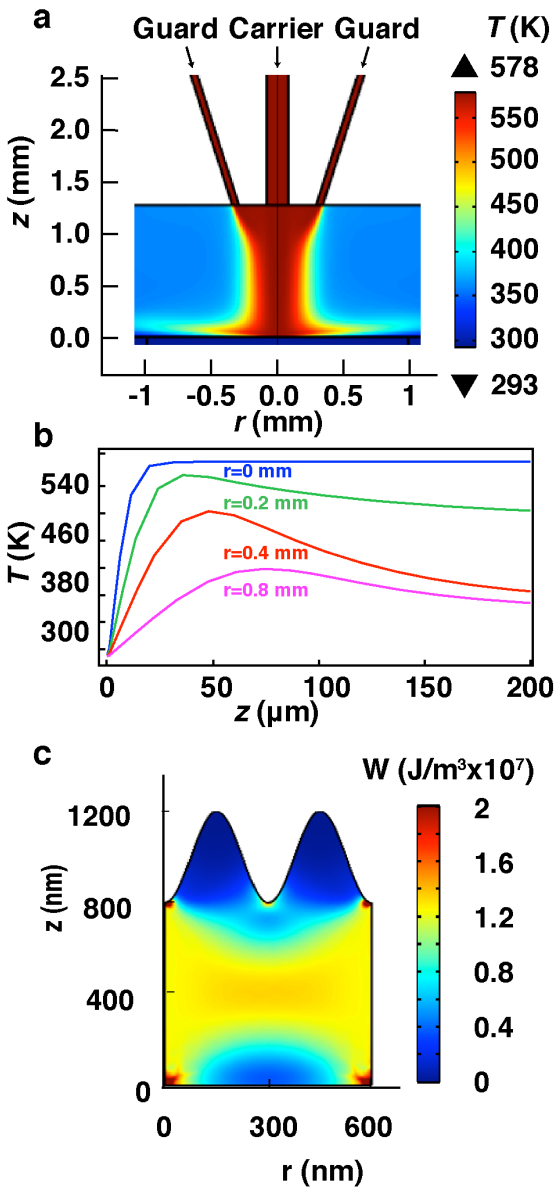

Figure 4-7 Temperature distribution in GF-OVJP system.
(A) Simulated temperature of jet exiting the nozzle and impinging onto substrate. (B) Simulated temperature distribution across substrate- nozzle region at different radial positions. (C) Simulated thermal stresses occurring in GF-OVJP grown film.

Consequently, the in-plane and out-of-plane thermal gradient in the film increases with film thickness, due to the low thermal conductivity of organic materials (~0.1W $m^{-1}K^{-1}$) (*29*), causing elastic strains in and out of the substrate plane. **Figures 4-6a** and **4-6b** show the thermal gradients and resulting stresses occurring within a film grown by GF-OVJP.

For these values, the critical wavelength is on the order of 100 nm, in good agreement with experimentally observed critical wavelength for SubPc (**Fig. 4-9a**). As deposition continues, film thickness increases, and so does the amplitude of the waviness. When lobes start to form, the film thickness does not increase anymore, and only spheres are growing.

To model the surface evolution, we start with an equation describing the driving force acting on a given surface element during growth and under mechanical stress (*27*):

$$P_f = -\gamma K - g - W \quad (4.4)$$

where: P_f - driving force (N m^{-2}); γ - surface energy (J m^{-2}), K - surface curvature (m^{-1}); g - phase transition enthalpy (J m^{-3}), W - elastic strain energy (J m^{-3}). The relation between the driving force and velocity normal to the surface of a surface element is

$$v_n = LP_f \quad (4.5)$$

where v_n is the surface element velocity (m s^{-1}), and L is surface element mobility (m^2 s kg^{-1}). Then the velocity of each surface point during the evolution can be recalculated with each time step according to the new surface geometry (**Fig. 4-8**) and the resulting driving force.

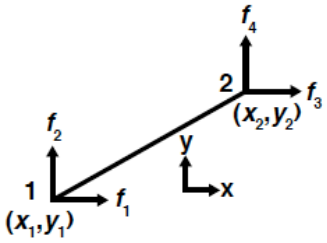

Figure 4-8 Surface element definition
The surface is divided into surface elements, each element is represented by x, y coordinates and angle deviation from flat surface θ.

The surface strain energy at a nodal point i, W_i is approximated via Eq. 4.5, where the maximum strain energy is at the surface valleys (**Fig. 4-7c**):

$$W_i = \frac{\sigma^2}{r}[1 - r(y_i - \bar{y})]^2 \quad (4.6)$$

where r is a dimensionless constant matched to surface waviness; $(y_i - \bar{y})$ is the elemental deviation from the average surface height $\bar{y}$ (m). Basic equation defining the relation between geometry- **H** matrix, elements points velocities vector $[\dot{x}, \dot{y}]$, and elements points forces vector **f** is given by:

$$\left[H_{ij}\right]\begin{bmatrix} \dot{x}_1 \\ \dot{y}_1 \\ \dot{x}_2 \\ \dot{y}_2 \end{bmatrix} = \begin{bmatrix} f_1 \\ f_2 \\ f_3 \\ f_4 \end{bmatrix} \quad (4.7)$$

Equation 4.8 describes vector **f** expressed in terms of material properties:

$$\begin{bmatrix} f_1 \\ f_2 \\ f_3 \\ f_4 \end{bmatrix} = \gamma \begin{bmatrix} \cos\theta \\ \sin\theta \\ -\cos\theta \\ -\sin\theta \end{bmatrix} + \frac{\lg}{2}\begin{bmatrix} -\sin\theta \\ \cos\theta \\ -\sin\theta \\ \cos\theta \end{bmatrix} + \frac{l}{2}\begin{bmatrix} (\frac{2}{3}W_1 + \frac{1}{3}W_2)\sin\theta \\ -(\frac{2}{3}W_1 + \frac{1}{3}W_2)\cos\theta \\ (\frac{1}{3}W_1 + \frac{2}{3}W_2)\sin\theta \\ -(\frac{1}{3}W_1 + \frac{2}{3}W_2)\cos\theta \end{bmatrix} \quad (4.8)$$

H matrix is given by:

$$\left[H_{ij}\right] = \frac{l}{6L}\begin{bmatrix} 2\sin^2\theta & -2\sin\theta\cos\theta & \sin^2\theta & -\sin\theta\cos\theta \\ -2\sin\theta\cos\theta & 2\cos^2\theta & -\sin\theta\cos\theta & \cos^2\theta \\ \sin^2\theta & -\sin\theta\cos\theta & 2\sin^2\theta & -2\sin\theta\cos\theta \\ -\sin\theta\cos\theta & \cos^2\theta & -2\sin\theta\cos\theta & 2\cos^2\theta \end{bmatrix} \quad (4.9)$$

Same approach for surface evolution modeling is used for multiple elements. Each iteration corresponds to single time step. At each iteration the velocity of a surface element is recalculated

according to the driving force applied to surface element and migrates according to defined time step and corresponding velocity. Detailed explanation of model can be found in (*27*). The time step used in this study was 0.001 s, and the final surface evolution was calculated for 1000 sec. The surface element size *l* was 1-10 nm (element size is changing during simulation due to changing surface morphology).

Figure 4-9 shows the predicted morphological evolution at different time steps. The mechanism for spheroidal morphology formation obtained using this analytical model is in good agreement with the experiments.

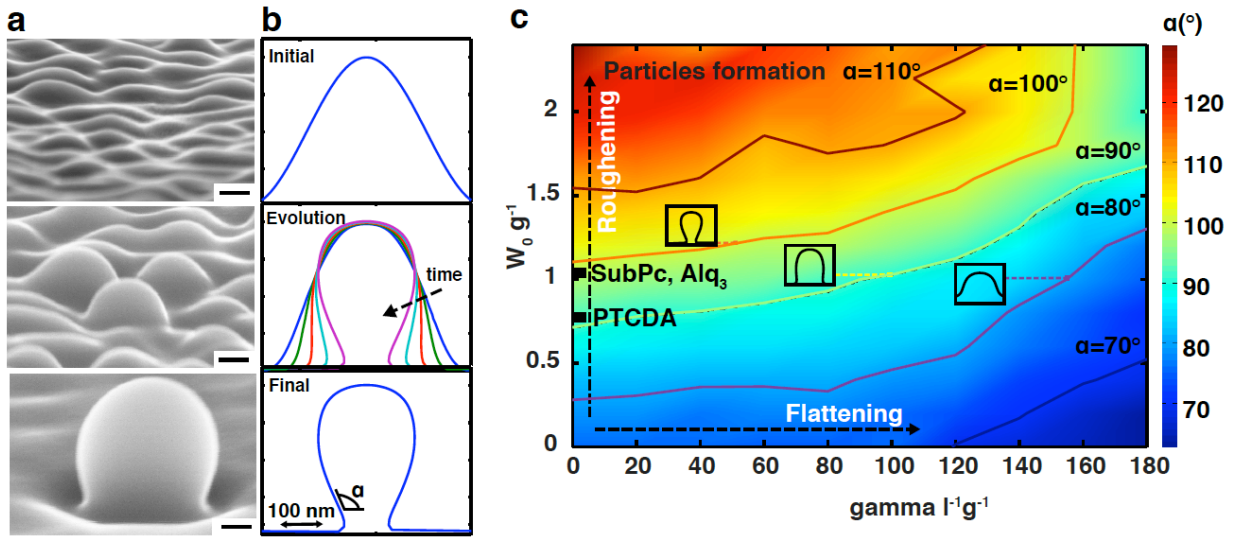

Figure 4-9 Surface evolution simulation
(A) Evolution of surface from wave to lobe shape. Scale bar 100 nm. (B) Simulated evolution from wave into lobe shape modeled using finite element difference approach. (C) Contour plot of possible final geometries with respect to deviation from surface, as a function of dimensionless ratio of material surface energy gamma and initial maximal elastic energy W_0 to material bulk energy g (gas-solid phase transition enthalpy in this case). l- characteristic length-scale of interest, taken here as 1 nm.

The process of surface evolution happens simultaneously with growth and film annealing, which is the main reason for the observed phenomenon of obtaining crystalline, yet smooth and spherical microstructures. **Figure 4-9c** is a contour plot of the resulting morphologies where the

figure of merit is a deviation angle α from the surface. Different morphologies and their associated α values are obtained by varying the dimensionless numbers $W_0\ g^{-1}$ and $\gamma\ l^{-1}g^{-1}$), relating the surface energy γ (*gamma* in the **Fig. 4-9c**) and initial maximum elastic energy W_0 to phase transition enthalpy g, respectively. Here l (m) is a characteristic scale of interest. A deviation angle greater than 90 degrees will lead to spheroidal morphologies, while deviation angles close to 90 degrees will result in platelet-like morphology. Deviations less than 90 degrees will result in a less wavy morphology with a tendency towards surface flattening. Surface energy and phase transition enthalpy are intrinsic materials properties, while elastic strain energy is calculated from both intrinsic mechanical properties and deposition parameters (e.g. inasmuch as they determine the degree of thermal expansion and strain). There is thus a trade-off between surface and elastic energy; while high surface energy will flatten the films, low surface energy will result in lobe formation. The model, therefore, can be used to describe morphologies of other organic materials under different processing conditions and provide a foundation for understanding microstructure formation and evolution.

As an example, while Alq_3 films deposited by GF-OVJP show identical spherical morphologies (**Fig. 4-10a**) due to similar intrinsic properties and process conditions, organic molecules with high anisotropy in molecular shape and mechanical properties, such as 3,4,9,10-Perylentetracarbonsäuredianhydrid (PTCDA) evolve a platelet-like morphology (**Fig. 4-10b**).

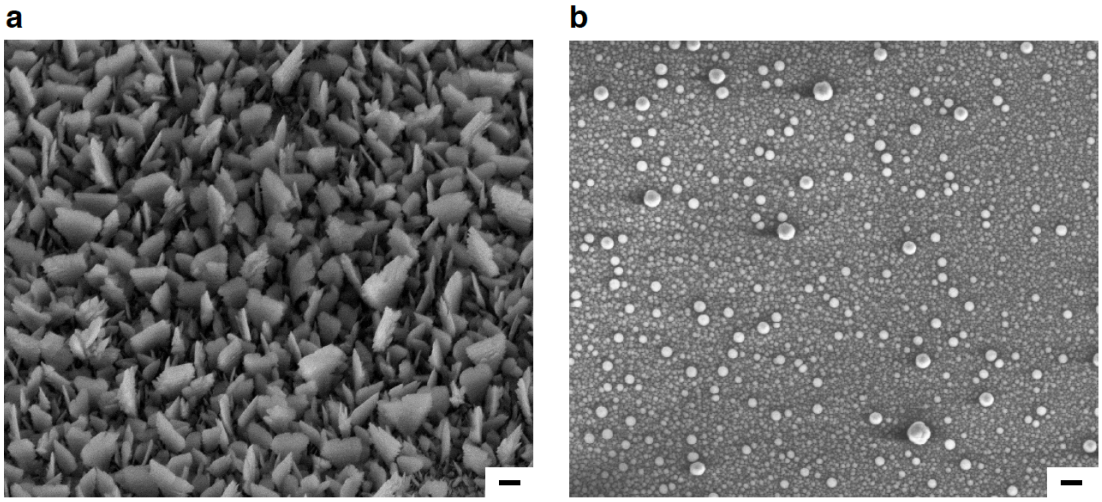

Figure 4-10 PTCDA and Alq_3 morphology grown in GF-OVJP
(A) Morphology of PTCDA deposited at 450°C source temperature, 5 min dwell time spot deposit. In this case platelet-like growth demonstrated, with deviation angles measured from the surface close to 90 degrees. (B) Morphology of Alq_3 deposited at 300°C source temperature, 1 min dwell time deposit. In this case, lobular features, similar to SubPc, are obtained. Scale bar is 1 μm[2].

All samples in the current study were deposited onto (100) silicon. Similar microstructures were obtained on different orientations of silicon: (110) and (111), as well as on Si (100) substrate coated with 100 nm Al, indicating that the obtained microstructures are a result of temperature profiles in the substrates and the film coatings, rather than related to the crystal structure of the substrate.

4.5 Summary

We observed new spheroidal crystalline ("lobe"-like) microstructures comprised of small organic molecules, with controllable and scalable sizes (100 nm - 1 μm), when grown by organic vapor jet printing. Initially, the film surface forms wavelike features with a characteristic wavelength, which evolve into lobes. X-ray diffraction indicated these lobes to be crystalline, despite their non-faceted shape. A model was developed for surface evolution that can be applied for the prediction and quantitative understanding of small molecular-based film morphologies obtained

via different growth techniques and conditions. For example, we showed that some organic materials will not exhibit lobe growth, but instead will show platelet-like features, confirmed by experiment. The deposition approach discussed here opens a new path for applications of small organic molecular materials where microstructural features of interest are on the order of hundreds of nanometers. These include optoelectronic device applications with high charge carrier mobility and exciton diffusion length (*30*), antireflection coatings(*31*), hydrophobic/oleophobic/omniphobic textured surfaces (**Fig. 4-11**), as well as the printing of pharmaceutical and food substances (*32*), where thick organic films with high surface area are needed[3]. In the next chapter we will demonstrate application of OVJP for printing of molecular pharmaceutical substances.

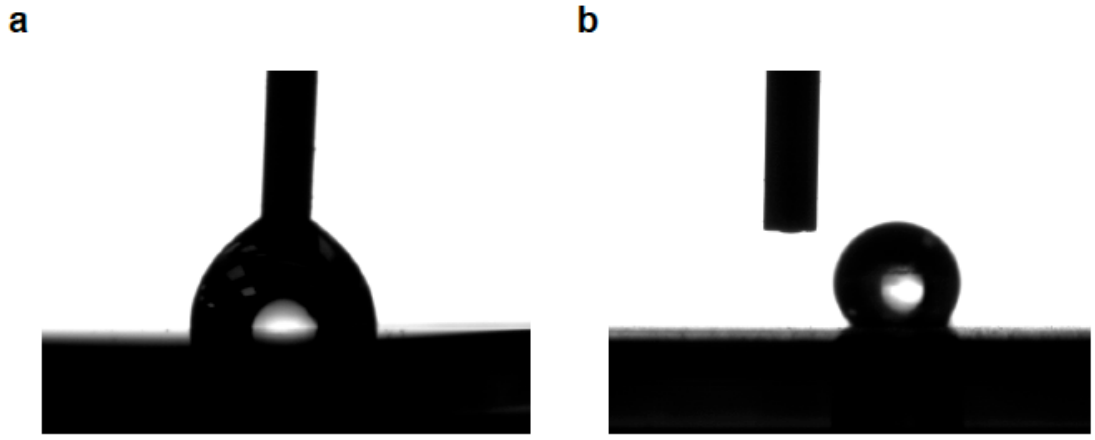

Figure 4-11 Contact angle measurement for SubPc films with and without lobes
Here difference in water contact angle is demonstrated for 300 nm thick film (A) and 800 nm film with lobes (B) formed on top. Due to lobes formation, a highly hydrophobic surface is obtained and contact angle is changing from 90±2^{o} for flat surface to 155±2^{o} for lobes surface. This demonstrates one of the possible applications of the obtained surfaces.

4.6 References

1. F. Yang, M. Shtein, S. R. Forrest, Controlled growth of a molecular bulk heterojunction photovoltaic cell. *Nature Materials* **4**, 37 (2005).
2. S. Y. Heo *et al*., Bifunctional Moth-Eye Nanopatterned Dye-Sensitized Solar Cells: Light-Harvesting and Self-Cleaning Effects. *Advanced Energy Materials* **4**, 1 (2014).

3. J. J. Chiu, C. C. Kei, T. P. Perng, W. S. Wang, Organic Semiconductor Nanowires for Field Emission. *Advanced Materials* **15**, 1361 (2003).
4. S. Mitragotri, J. Lahann, Physical approaches to biomaterial design. *Nature Materials* **8**, 15 (2009).
5. S. Biswas, O. Shalev, M. Shtein, Thin-Film Growth and Patterning Techniques for Small Molecular Organic Compounds Used in Optoelectronic Device Applications. *Annual Review of Chemical and Biomolecular Engineering* **4**, 289 (2013).
6. S. R. Forrest, Ultrathin Organic Films Grown by Organic Molecular Beam Deposition and Related Techniques. *Chemical Reviews* **97**, 1793 (1997).
7. B. E. Lassiter, R. R. Lunt, C. K. Renshaw, S. R. Forrest, Structural templating of multiple polycrystalline layers in organic photovoltaic cells. *Optics Express* **18**, A444 (2010).
8. J. D. Zimmerman *et al*., Independent Control of Bulk and Interfacial Morphologies of Small Molecular Weight Organic Heterojunction Solar Cells. *Nano Letters* **12**, 4366 (2012).
9. S. Singha Roy, D. J. Bindl, M. S. Arnold, Templating Highly Crystalline Organic Semiconductors Using Atomic Membranes of Graphene at the Anode/Organic Interface. *The Journal of Physical Chemistry Letters* **3**, 873 (2012).
10. Y. S. Zhao *et al*., Low-Dimensional Nanomaterials Based on Small Organic Molecules: Preparation and Optoelectronic Properties. *Advanced Materials* **20**, 2859 (2008).
11. K.-J. Huang, Y.-S. Hsiao, W.-T. Whang, Selective growth and enhanced field emission properties of micropatterned iron phthalocyanine nanofiber arrays. *Organic Electronics* **12**, 1826 (2011).
12. M. Shtein, Organic Vapor-Phase Deposition in *Organic Electronics: Materials, Processing, Devices and Applications*, F. So, Ed., CRC Press, 27 (2009).
13. M. Shtein, P. Peumans, J. B. Benziger, S. R. Forrest, Direct, Mask- and Solvent-Free Printing of Molecular Organic Semiconductors. *Advanced Materials* **16**, 1615 (2004).
14. S. Biswas, K. P. Pipe, M. Shtein, Solvent-free, direct printing of organic semiconductors in atmosphere. *Applied Physics Letters* **96**, 263301 (2010).
15. S. Biswas, K. A. Luck, M. Shtein, Guard flow-enhanced organic vapor jet printing of photovoltaic donor materials in air. *Organic Electronics* **13**, 2905 (2012).
16. S. Biswas *et al*., Spatial Mapping of Morphology and Electronic Properties of Air-Printed Pentacene Thin Films. *Advanced Functional Materials* **24**, 3907 (2014).
17. A. Gumennik *et al*., Silicon-in-silica spheres via axial thermal gradient in-fibre capillary instabilities. *Nature Communications* **4**, 1 (2013).
18. L. Bocquet, E. Lauga, A smooth future? *Nature Materials* **10**, 334 (2011).
19. A. Tuteja, W. Choi, G. H. McKinley, R. E. Cohen, M. F. Rubner, Design Parameters for Superhydrophobicity and Superoleophobicity. *MRS Bulletin* **33**, 752 (2008).
20. M. Lefort *et al*., Nanosized Films Based on Multicharged Small Molecules and Oppositely Charged Polyelectrolytes Obtained by Simultaneous Spray Coating of Interacting Species. *Langmuir* **29**, 14536 (2013).
21. J. E. Pye, C. B. Roth, Physical Aging of Polymer Films Quenched and Measured Free-Standing via Ellipsometry: Controlling Stress Imparted by Thermal Expansion Mismatch between Film and Support. *Macromolecules* **46**, 9455 (2013).
22. P. W. Voorhees, The theory of Ostwald ripening. *Journal of Statistical Physics* **38**, 231 (1985).

23. I. M. Lifshitz, V. V. Slyozov, The kinetics of precipitation from supersaturated solid solutions. *Journal of Physics and Chemistry of Solids* **19**, 35 (1961).
24. H. Kietaibl, The crystal and molecular structure of a new phthalocyanine-like boron complex. *Monatshefte für Chemie / Chemical Monthly* **105**, 405 (1974).
25. B. E. Warren, *X-ray diffraction*. Addison-Wesley Pub. Co. (1969).
26. D. J. Eaglesham, M. Cerullo, Dislocation-free Stranski-Krastanow growth of Ge on Si(100). *Physical Review Letters* **64**, 1943 (1990).
27. Z. Suo, Motions of Microscopic Surfaces in Materials in *Advances in Applied Mechanics,* vol. 33, J. W. Hutchinson, T. Y. Wu, Eds., Elsevier Science, 193 (1997).
28. M. Kanari, H. Kawamata, T. Wakamatsu, I. Ihara, Intermolecular elastic and plastic characteristics of organic phthalocyanine thin films evaluated by nanoindentation. *Applied Physics Letters* **90**, 061921 (2007).
29. Y. Jin *et al*., Thermal boundary resistance of copper phthalocyanine-metal interface. *Applied Physics Letters* **98**, 093305 (2011).
30. B. Verreet, P. Heremans, A. Stesmans, B. P. Rand, Microcrystalline Organic Thin-Film Solar Cells. *Advanced Materials* **25**, 5504 (2013).
31. K. Choi *et al*., Nano-tailoring the Surface Structure for the Monolithic High-Performance Antireflection Polymer Film. *Advanced Materials* **22**, 3713 (2010).
32. N. Sandler *et al*., Inkjet printing of drug substances and use of porous substrates-towards individualized dosing. *Journal of Pharmaceutical Sciences* **100**, 3386 (2011).

Chapter 5
OVJP of Molecular Pharmaceuticals for Controlled Drug Release

5.1 Introduction

5.1.1 Small organic molecules in pharmaceutical industry

As of 2014, there are nearly 1460 Food and Drug Administration (FDA) approved medicines on market and tens of thousands drug candidates being tested (*1*). Nearly 90% of active pharmaceutical ingredients (API) comprise small molecular organic compounds (<900 g mol^{-1} molecular weight). Similarly to small molecular organic compounds in organic electronics industry these molecules comprise mostly from carbon-hydrogen bonds. Examples of archetypal compounds are shown in **Fig. 5-1**.

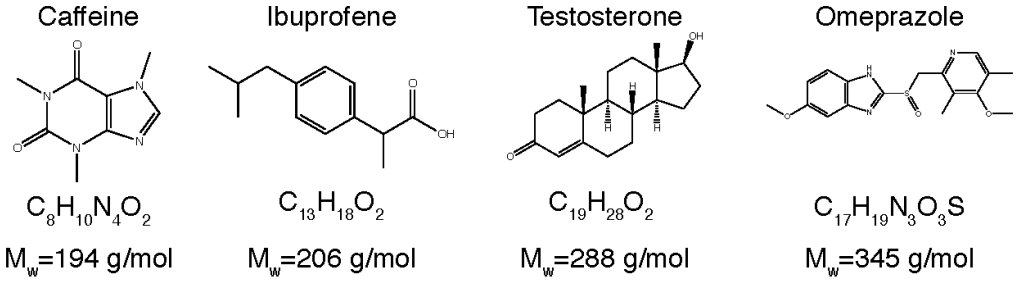

Figure 5-1 Archetypal small molecular substances used in medical applications

5.1.2 Current challenges in pharmaceutical industry

The drug development process is divided to three main stages (or phases) (*2*). Phase I is drug discovery and development. This step starts from understanding of the disease process and involves molecular design that would stop or inhibit the effect of the disease. Screening of thousands of compounds is performed to find the best drug candidates that would result in desired drug efficacy with minimum side effects (or toxicity). At this stage all tests are performed on a laboratory scale where drug is tested for absorption, distribution and metabolism in the body. The tests are performed in simulated biological environment, depending on drug administration route – oral, transdermal, intravenous, etc. Phase II is preclinical research where drug is usually tested on animal models. The purpose of this stage is to obtain knowledge about drug toxicity and needed dosage before it can be administered to humans. Phase III is clinical research where drugs are tested on human patients with the disease. In case all three phases are successful and drug is proved to have the desired efficacy and safety, FDA reviews all development and manufacturing processes and gives the final approval for release of medicine to the market.

Drug discovery, reliable dosing, and manufacturing scale-up are severely limited by poor solubility kinetics. Over 40% of newly developed small molecular compounds have poor solubility in aqueous media and, hence, poor bioavailability (*3, 4*). While there is a growing emphasis in drug research and development on high potency medicines and alternative delivery vehicles (*5-7*) (e.g. dermal and buccal patches, biodegradable implants, etc.), the traditional approaches used in the pharmaceutical industry do not offer adequate precision in medicine formulation and manufacture (*8*). Furthermore, prior to approval for general use (Phase I and II), drugs undergoing initial testing are typically dissolved in organic solvents, dimethyl sulfoxide

(DMSO) being one of the most common, leading to erroneous estimation of drug efficacy and bioavailability, as compared to direct application of the API in its powder form. Finally, high throughput manufacturing is limited with respect to poorly soluble APIs and suffers from fundamental trade-offs with requirements for achieving personalized dosing (*9, 10*).

All aforementioned limitations result in extremely high costs of drug development, and, perhaps most importantly in lack of ability to provide a cure for many diseases (*11*). For instance, only 5% of agents that have anticancer activity in preclinical development are licensed after demonstrating sufficient efficacy in phase III testing (*12*). **Table 5-1** and **Fig. 5-2** demonstrate attrition rates and development costs of medicines over the past years, exceeding 1 billion dollars price to develop a new medicine (*13,14*).

Table 5-1 Attrition rates and duration of various drug development stages
The overall chance of failure for new tested compound is >90% (*15*)

	Discovery	Preclinical	Phase I	Phase II	Phase III	Overall
Time per stage (years)	3.5	0.46	1.4	2.3	5.1	**12.9**
Chance of failure	0.4	0.35	0.22	0.3	0.1	**0.984**
Progression probability (to next discovery stage)	0.5	0.5	0.4	0.4	0.15	
Chance that one project entering this stage will eventually successfully leave it	0.58	0.52	0.42	0.52	0.44	
Number of projects needed to achieve one successful launch	30	13	6.2	3.6	1.7	

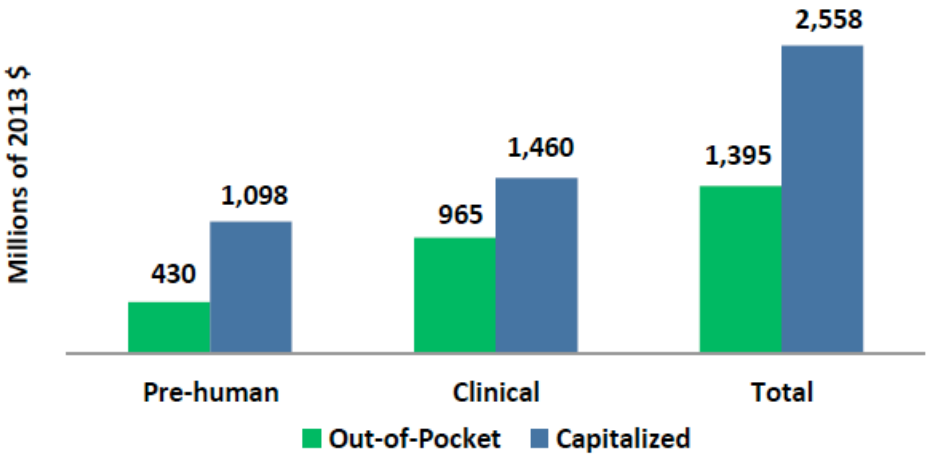

Figure 5-2 Out-of-pocket and capitalized costs per approved new compound (*13*)
Out-of-pocket is the total cost required for drug launch. Capitalized cost is out-of-pocket cost corrected for cost of capital. Since investors require a return on research investments that reflects alternative potential uses of their investment, the capitalized cost per drug launch increases out-of-pocket costs by the cost of capital for every year from discovery to launch.

This recent costs analysis leads to understanding that a radically new approach is needed to address the challenges that pharmaceutical industry faces these days. In current chapter we will discuss in detail the underlying principles in drug research and development and state-of-the art solutions to some of challenges mentioned above.

5.1.3 Classification of drug properties

65% of human body is comprised of water (*16*). Therefore, in order to reach the target site in the organism, the drug must have appropriate aqueous solubility. However in order to penetrate biological tissues, a drug needs to be lipophilic, i.e. able to dissolve in fats and oils (*16*). This inherent trade-off is one of the main reasons for difficulties in drug development today.

Poorly water soluble drugs are eliminated from the gastrointenstinal tract before they fully dissolve and are absorbed in blood circulation. This results in low bioavailability and poor dose portionality, which hinders clinical translations. In such cases, dose increase is necessary to ensure appropriate drug concentration in the blood. The dose augmentation results in topical

toxicity in gastrointestinal tract and decrease in patient compliance, in addition to increased manufacturing costs. *In-vitro* essay studies of poorly water soluble or drugs with low dissolution rates drugs is also a complicated task since drug precipitation will lead to inaccurate data reading of the drug properties. The degree of thermodynamic solubility of different drugs is demonstrated in **Table 5-2**.

Table 5-2 Drugs solubility classification (*3*)

Description forms (solubility definition)	Solubility range (mg/ml)
Very soluble (VS)	>1,000
Freely soluble (FS)	100-1,000
Soluble	33-100
Sparingly soluble (SPS)	10-33
Slightly soluble (SS)	1-10
Very slightly soluble (VSS) 0.1-1 0.1	0.1-1
Practically insoluble (PI) 0.01	<0.1

In order to determine if a chemical compound with a certain pharmacological or biological activity has properties that would make it a likely orally active drug in humans C. Lipinski et al (*17*) formulated a “Rule of five” (RO5), based on the observation that most orally administered drugs are relatively small and moderately lipophilic molecules. The rule describes molecular properties important for drugs pharmacokinetics: absorption, distribution, metabolism, and excretion ("ADME"). However, the rule does not predict if a compound is pharmacologically active.

The rule is important to keep in mind during drug discovery when a pharmacologically active lead structure is optimized to increase the activity and selectivity of the compound as well as to ensure drug-like physicochemical properties are maintained as described by Lipinski's rule.

Candidate drugs that conform to the RO5 tend to have lower attrition rates during clinical trials and hence have an increased chance of reaching the market.

Components of the rule are:

1. No more than 5 hydrogen bond donors (the total number of nitrogen-hydrogen an oxygen-hydrogen bonds).
2. No more than 10 hydrogen bond acceptors (all nitrogen or oxygen atoms)
3. A molecular mass less than 500 gr/mol
4. An octanol-water partition coefficient log P not greater than 5.

G. Amidon et.al presented a Biopharmaceutics Classification System, BCS (*18*), which is based on drug solubility and permeability properties and classifying the severity of solubility-permeability interplay in API (**Fig. 5-3**).

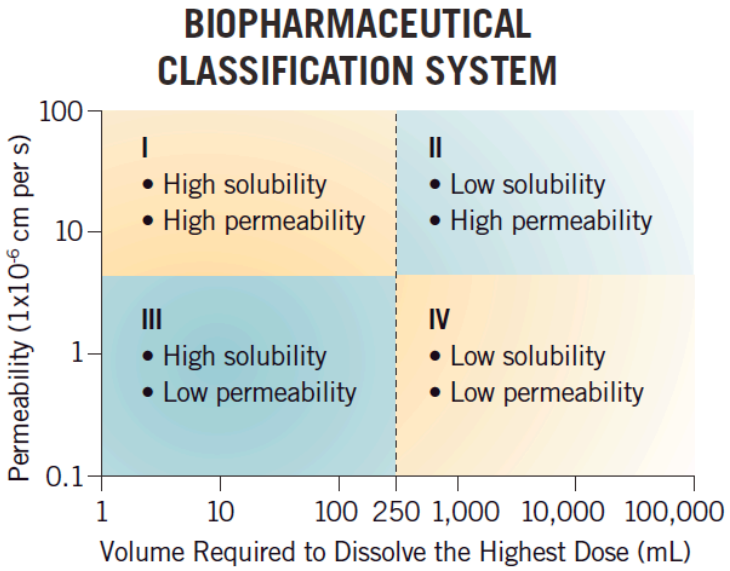

Figure 5-3 BCS classification system

BCS places an orally administered API in one of four categories depending on its solubility and permeability. A drug substance is considered "highly soluble" when the highest clinical dose strength is soluble in 250 mL or less of aqueous media over a pH range of 1-7.5 at 37 °C. A drug

substance is considered to be “highly permeable” when the extent of the absorption (parent drug plus metabolites) in humans is determined to be ≥90% of an administered dose based on a mass balance determination or in comparison to intravenous reference dose (*18*).

Currently ~60% of newly developed compounds are BCS Class II, making low solubility one of the major challenges in drug development (*16*).

5.1.4 Solubility and dissolution rate of API

Physical picture of dissolution process is shown in **Fig. 5-4**.

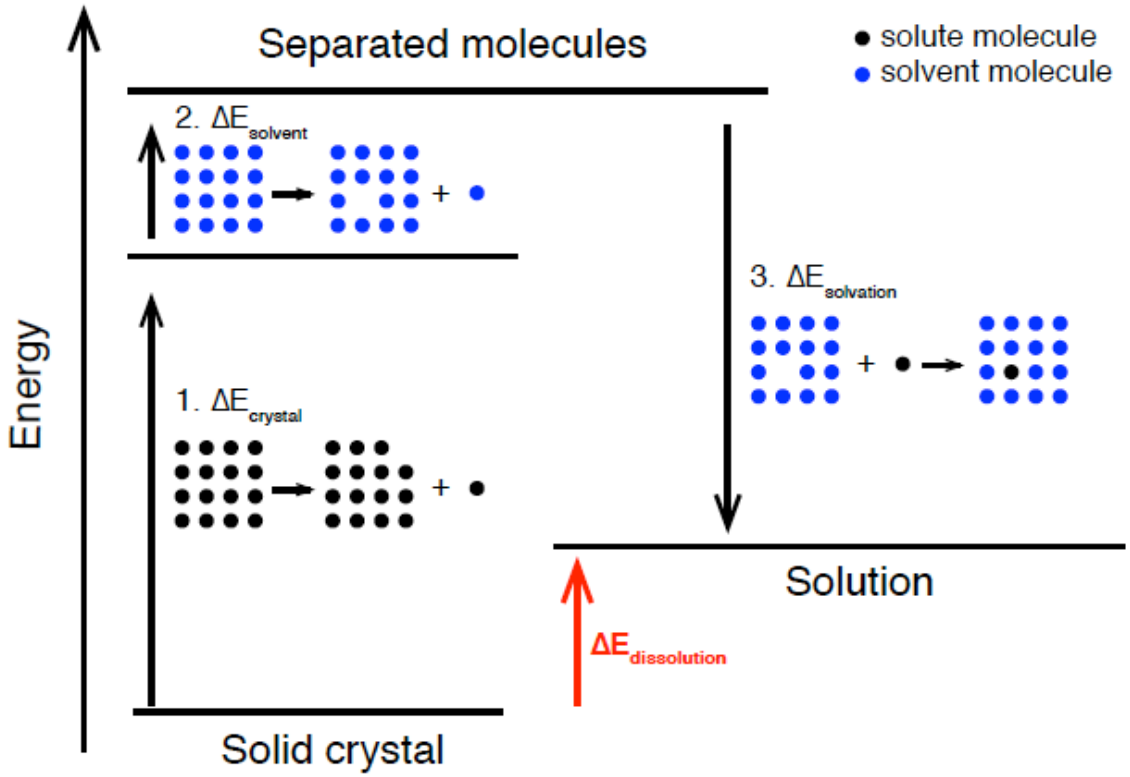

Figure 5-4 Dissolution process schematic
Depending on differences between crystal lattice energy and solvation energy the dissolution process will be thermodynamically favorable ($\Delta E_{dissolution}<0$) or unfavorable ($\Delta E_{dissolution}<0$)

The dissolution process can be described by three steps (*19*). First step is removal of solid particle from the crystal lattice - this energy can be estimated by solid-solid interactions. As was

discussed in **Chapter 2**, melting and evaporation enthalpies are good estimates for bonding strength in organic solids. Second step is a void formation in the solvent that is sufficient to accommodate the abstracted solute molecule. Since intermolecular forces in the liquid state are much lower than those in the solid state, the energy required to create a void in the solvent is relatively lower than rest of energies associated with dissolution process. Third step is the insertion of the solute molecule into the solvent void. For molecules with some affinity for a polar solvent such as water, this process is energetically favorable and therefore drives drug solubility ($\Delta E_{dissolution}<0$). The rationale behind the last step is often quoted as " like dissolves like". Overall there are two primary determinants of drug solubility: 1) the energy required to overcome the strength of intermolecular forces in the solute solid state and 2) the energy generated on the interaction of solute and solvent molecules in solution (solvation). Therefore, high crystal energy and low solvation energy result in low solubility. In case of ideal solubility, where the intermolecular forces between solute and solvent equal to those between solute and solute and those between solvent and solvent (no net energy charge), solubility is defined as (*19*):

$$\log C_s = -\frac{\Delta H_f}{2.303R}\left(\frac{T_m - T}{T_m T}\right) \quad (5.1)$$

where C_s is mole fraction solubility of solute, ΔH_f is enthalpy of fusion of solid, T_m is melting point and T is temperature. Since the differences between solute-solute interactions and solute-solvent interactions in aqueous solutions are significant, nonideal solution behavior is obtained with solubility lower than would be predicted in ideal solution. In this case, the difference between ideal and nonideal behavior is described by by a correction factor termed the activity coefficient (γ) (*19*):

$$\log c_s = -\frac{\Delta H_f}{2.303R}\left(\frac{T_m - T}{T_m T}\right) - \log(\gamma) \quad (5.2)$$

the activity coefficient is a function of the molar volume of the solvent V_s, the volume fraction of the solute φ_1, and the difference in the solubility parameters for the solvent δ_1 and solute δ_2:

$$\log(\gamma) = \frac{V_s \varphi^2}{2.303RT}(\delta_1 - \delta_2)^2 \quad (5.3)$$

The solubility Eq. 5.2 is determined by the changes in the solid state properties of a drug and the activity coefficient. These principles define the possible pathways to solubility enhancement – one is alternating solid-state properties (the strength of the crystal lattice), the other is changing solvation behavior (solute solvent interactions in solution), or a combination of thereof. When a compound have a combination of limited affinity for water (hydrophobicity) and strong intermolecular forces in a solid state, it will be poorly soluble in both aqueous and nonaquueous solvents. In case of hydrophobic molecules with relatively low intermolecular forces, the compounds might dissolve in lipid-based solvents (lipophilic). In this case lipid-based delivery technology can be used (e.g. gelatin capsules) (*19*).

5.1.5 Effect of pH on solubility

The solvation properties of drug molecules in aqueous media depend on the extent of ionization (*19*). In case molecule is comprised from charged functional group, ion-dipole interactions with polar solvents such as water will occur and increase hydration and water solubility. Depending on the interaction strength, the solutes can be categorized into nonelectrolytes (no dissociation into ionic species in water), weak electrolytes (partial dissociation) or strong electrolytes (full ionization such as in ionic material NaCl).

Small organic molecular medicines are either nonelectrolytes or weak electrolytes (*19*). In case of weak electrolytes, the degree of dissociation into ions dependents on the pKa of the electrolyte and the pH of the solution. If pH values above the pK_a of a weak acid and below the pK_a of a

weak base, solubility will increase due to ionization (*19*). Therefore, modification in a pH of a solution can enhance the solubility in case the drug is weak electrolyte.

5.1.6 Solubility vs. dissolution rate

Drug solubility is a thermodynamic term, which defines the maximum concentration of a solute that can be reached in a given solution. The rate at which solid drug transforms into dissolved compound is also important in case the time available for dissolution is limited. For instance, in case of oral administration, the time it takes the drug to dissolve should be significantly higher than the time to pass through gastrointestinal tract. At the same time, if the dissolution rate is high, but the equilibrium solubility is low, the dose of the absorbed drug would not be sufficient (*19*).

The process of dissolution can be considered as a heterogeneous reaction in which a mass transfer is affected by net flux of solute molecules at a solid surface (*20*). These reactions can be classified as following: (a) The reaction or interaction at the interface occurs much faster than the rate of transport of reactants to and products from the interface. The rate in this case is determined by the transport process. In dissolution this would be the diffusion or convective transport of solute from the interfacial boundary to the body of the solution. (b) The rate of reaction at the interface is much slower than the transport processes and hence determines the rate. If this were to occur in dissolution, the actual processes of desorption and adsorption of the solute molecules at the interface would determine the rate. (c) Both rates are of the same order of magnitude so that the over-all rate is a function of both processes. Looking back at different carrier gas assisted deposition techniques described in introduction section, process (a) would be analogous to OVPD process, controlled by rate of evaporation from the surface and (b) would be analogous to OVJP process, controlled by rate of carrier gas convection above the evaporating

surface. Noyes and Whitney (*21*) quantitatively studied dissolution by rotating cylinders of benzoic acid and lead chloride in water, deriving the following relationship:

$$\frac{dC}{dt} = kA(C_s - C) \quad (5.4)$$

where C is solute concentration, t is time, k is dissolution constant, A is solute-liquid contact area It was found that a thin layer of saturated solution formed at the interface and that the observed velocity was the rate at which molecules diffused from this layer to the bulk solution (**Fig. 5-5**).

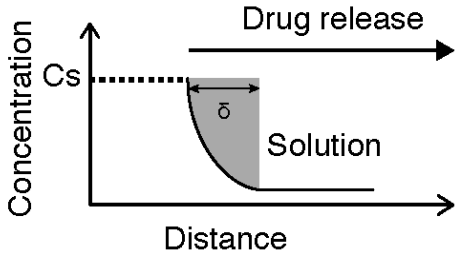

Figure 5-5 Schematic of dissolution process

Brunner (*21*) and Nernst used Fick's law of diffusion to define a correlation between k in the Eq. 5.1 and the diffusion coefficient of the solute,

$$k = \frac{DA}{V\delta} \quad (5.5)$$

where D is the diffusion coefficient, V is solvent volume, δ is boundary layer thickness. Initially it was assumed that boundary layer thickness is only dictated by diffusion process. The diffusion of small organic molecules in water is relatively high (*19*) and reducing the thickness of the diffusion layer through agitation in *vivo* is not feasible. Therefore solubility and surface area are the only factors that can be changed to affect the dissolution process. Importantly, enhancing the solubility will also increase the dissolution rate (Eq. 5.4).

Since solubility depends on solid-solid interactions in crystal lattice and on chemical structure of the molecule (polarity), three strategies for enhancement of solubility and dissolution rate are usually applied.

1. Reducing of solid crystal lattice energy through amorphous dispersions and cocrystallization with polar coformers.
2. Reducing of molecular hydrophobicity through surfactants, cyclodextrins and lipid-based systems.
3. Maximizing the surface area available for dissolution through particle size reduction.

For more information of various approaches for first and second group of strategies we recommend to read an extensive Savjani (*4*) and Williams (*19*) reviews. As will be described in a following sections, the main focus of this work is on particle size reduction.

5.1.7 Particle size reduction

Surface area of a particle scales as $1/r^2$, where r is an average particle size (*19*). Particle size reduction approaches are categorized into "top-down" - big particles are fragmented into smaller particles, or as " bottom-up" - small particles are recrystallized from a supersaturated solution.

Micronization process such as powder milling, results in the formation of particles in the micron size range. Addition of polymeric and surfactant stabilizers can produce particles in 200- 500 nm range (*19*). Particles reduction to nano-size scale (*23*) can result not only in enhanced dissolution rate but also in increased solubility due to changes particle curvature (*24*). However, nanocrystal formulations are complex due to high tendency to particles agglomeration and polymorphism (*25*, *26*).

5.1.8 Film form drug manufacturing

To achieve personalized dosing, combined with continuous manufacturing, formulation can be processed in a film form (*27, 28*). For topical applications, thin film pharmaceutical coatings are used in transdermal drug delivery systems such as patches and microneedles (*29*). For localized drug delivery, thin films of APIs are applied in the form of coatings onto various delivery vehicles (wafers, rods) (*6*). Film-form drug systems are also used for transmucosal and oral drug delivery, providing the means for rapid drug dissolution and transport to the systemic circulation (*30, 31*). Manufacturing of film-form drugs includes dispersion of API particles in a polymer matrix by mixing, dipping or spraying, followed by polymer casting or extrusion (*32*). An examples of most commonly used techniques - solvent casting and hot melt extrusion are shown in **Fig. 5-6**. These approaches suffer from limited particle dispersion, stability, and drug loading, especially when working with nanoparticles (*28*).

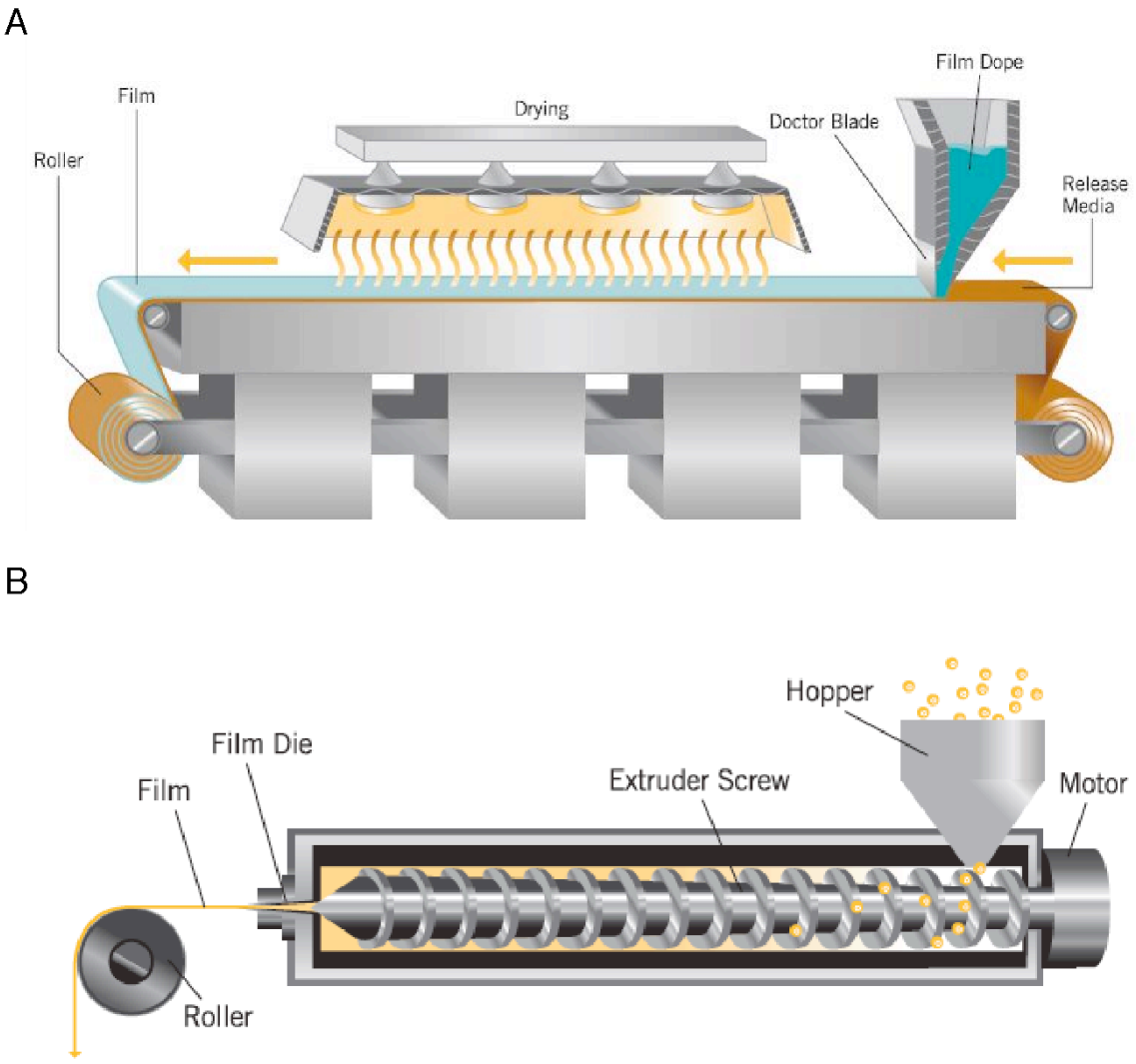

Figure 5-6 Film manufacturing techniques in pharmaceutical industry
(A) Solvent casting - polymer blend with active material and film forming and flavor additives is casted and dried. Relatively controlled thickness can be obtained, but required drying step is energy- and time- intensive. (B) Hot melt extrusion - polymer with active material is heated and extruded. Although this technique is solvent-free, thickness control is poor (*33*).

More recent approach of inkjet printing can potentially overcome these limitations, but would require a use of various solvents (**Fig. 5-7**). This is especially difficult task when working with low aqueous solubility compounds, where organic solvents would be needed and layer-by-layer deposition of different substances would not be possible (*34*).

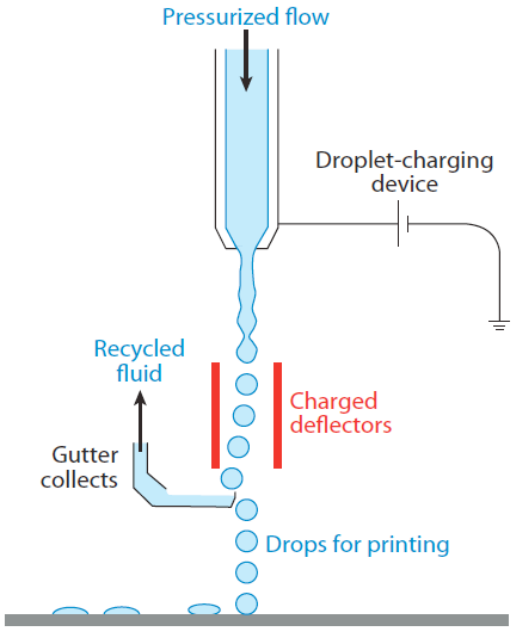

Figure 5-7 Schematic diagram of a continuous inkjet printer (*45*)

5.2 Printing of small molecular medicines from vapor phase

As discussed in previous section, reliable dosing, and manufacturing scale-up are severely limited by poor solubility kinetics, with over 40% of compounds having poor solubility in aqueous media and, hence, poor bioavailability (*36, 4*). While there is a growing emphasis in drug research and development on high potency medicines and alternative delivery vehicles (*6-7*) (e.g. dermal and buccal patches, biodegradable implants, etc.), the traditional approaches used in the pharmaceutical industry do not offer adequate precision in medicine formulation and manufacture (*8*). Various *micronization* and *nanonization* (*37*) techniques have been developed to enhance the bioavailability of an active pharmaceutical ingredient (API), commonly made in powder form, based on the fact that smaller particles possess greater surface area to volume ratio and hence faster dissolution. However, mechanical methods for producing small particles, such as powder milling, high pressure homogenization (HPH), are energy- and time- consuming. The resulting nanoparticles may lack stability during storage and controlled release (*38*). Formulating

medicines with nanoparticles is also challenging, since homogeneity and stability are difficult to achieve due to particles agglomeration and changes in crystallinity (*7*).

A radically new approach is needed to circumvent these and other challenges. In this work we demonstrate how deposition of API from vapor phase (using OVJP system as tool) bypasses dissolution rate bottlenecks with regard to formulation, yet produces coatings with dramatically and controllably improved dissolution kinetics. The proof-of-principle demonstration of enhanced bioavailability[4] of printed tamoxifen (*39*), a widely used yet poorly soluble cancer drug (BCS II type), suggests a completely new pathway for accelerating drug discovery, improving process control for dose accuracy [5]and consistency, and economical, scalable manufacturing.

5.3 Experimental setup

5.3.1 Film fabrication and process parameters

Caffeine (C0750) >99% was purchased from Sigma Aldrich. Tamoxifen (ICN15673883) >99.24% and paracetamol (5074863) >99.5% were purchased from Fisher Scientific. BAY 11-7082 (19542-67-7) >98% and ibuprofen (401003) >99% were purchased from EMD Millipore, fluorescein (32615) >99.8% was purchased from Fluka; all were used as received. Borosilicate glass slides, 12 mm diameter and 0.2 mm thickness, were used as substrates for film deposition. Substrates were cleaned by ultrasonication in detergent solution and deionized water, followed by acetone and isopropanol rinses, for 10 minutes each. Substrates were then placed in boiling isopropanol for 5 min and dried in pure nitrogen gas prior to film deposition.

OVJP nozzles used in this study were made from quartz tubes having 12.5 mm outer diameter and a nozzle tip of 500 μm internal diameter, with an approximately 15 degree inside wall taper

from the nozzle axis. The inert carrier gas was 99.99% pure nitrogen. The source consisted of ~0.15 g of powder embedded in a porous SiC ceramic foam of 100 DPI and placed in the heated source section of the tube. The process parameters that were kept constant are: nozzle-substrate separation distance (1.5 mm), substrate temperature (20 °C). The process was performed in glove box purged with 99.99% pure nitrogen gas.

To determine evaporation temperature of the powders, and subsequently source temperature in the system, thermogravimetric analysis (TGA) was used. All measurements were performed using a TA Instruments Thermogravimetric Analyzer Q500 at 0.01% accuracy, with nitrogen sample purge flow rate 60 ml/min and balance purge flow rate of 40 ml/min. Heating rate was 5 °C/min. Detailed processing conditions are given in **Table 5-3**. Deposits were formed by rastering the nozzle over the substrate to form adjacent, overlapping lines at 0.2 mm center-to-center spacing, allowing for homogeneous thickness of deposit for a nozzle of 0.5 mm inner diameter positioned 1.5 mm from substrate surface. Fluorescein films on microneedles were deposited through a flexible mask. The same process can be performed without a mask when using nozzle with appropriate printing resolution.

Table 5-3 OVJP processing conditions for materials used in the study.
Source temperature was determined via thermogravimetry and carrier gas flow rate tuned to obtain local deposition rate of ~ 0.5 μg/min.

Process parameter / Material	Carrier gas type	Carrier gas rate (sccm)	Source temperature (°C)	Substrate temperature (°C)
Fluorescein	Nitrogen	200	300	20
Caffeine	Nitrogen	100	130	20
Tamoxifen	Nitrogen	100	115	20
BAY 11-7082	Nitrogen	100	90	20
Paracetamol	Nitrogen	100	190	20
Ibuprofen	Nitrogen	150	75	20

5.4 OVJP system modification and initial feasibility tests

In order to test applicability of OVJP to pharmaceuticals printing, a number of questions must be addressed. For example, typical API films should be thicker than the organic semiconductor films used in optoelectronic devices, e.g. on the order of 100-1000 nm vs. 10 nm, respectively. As demonstrated in **Chapter 4**, OVJP is compatible with the deposition of thick (>500 nm) films (*40*). How does the (potentially prolonged) evaporation process affect the chemistry, structure, and functionality of a drug compound? Will advantageous film and particle morphologies be obtained when the API is printed at useful thicknesses and onto biocompatible substrates? What range of physical and chemical transformation temperatures of APIs are compatible with this technique?

To answer these questions, the OVJP process was modified further to evaporate an API from a porous ceramic source (**Fig. 5-8**) for enhanced rate stability, while the deposits are made onto biologically compatible substrates, followed by their detailed characterization.

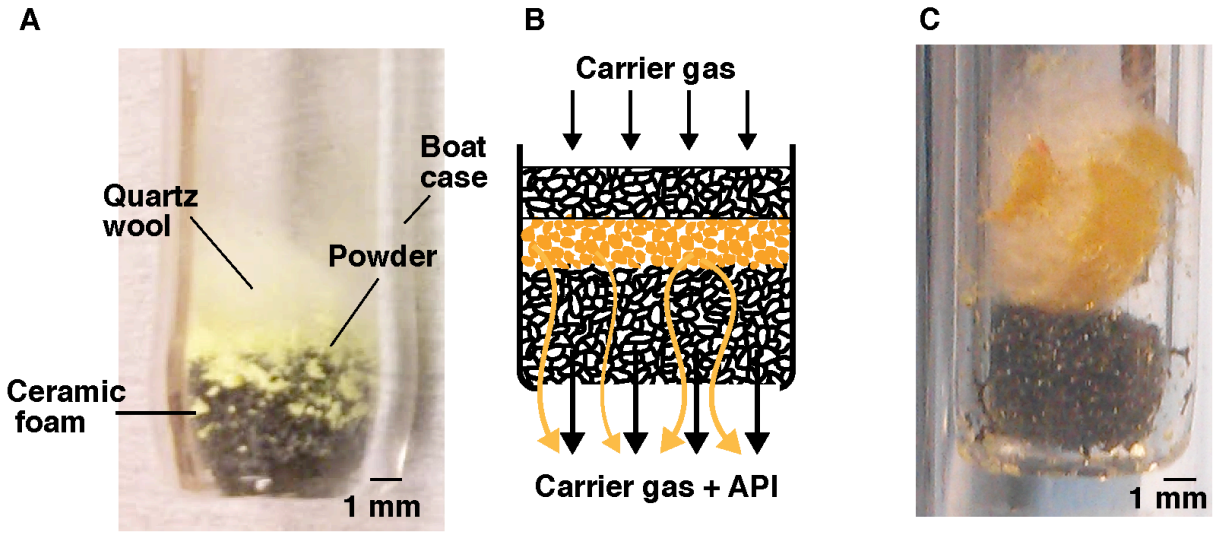

Figure 5-8 Porous evaporation source used for medicines printing

(A) Porous ceramic source loaded with powder. The source is made from silicon carbide foam cut to fit the boat size. Here the boat case is made of quartz and ceramic foam used is silicon carbide with porosity of 80 pores per inch (ppi) from Ultramet. The powder to be evaporated is placed either between two porous foam disks or a foam and a quartz wool. (B) Schematic of porous source operation. The pores prevent from powder to fall out and at the same time maximizing surface area for evaporation. Pore size can be chosen in accordance with powder particle size and state of material during evaporation (solid or liquid). (C) Example for evaporation of liquidized material. Material is held by capillary forces preventing it from spilling. The source can be reused after washing off the organic powder with appropriate solvents. This way repeatable processing conditions are obtained.

Figure 5-9 demonstrates the first reported examples of vapor jet coating onto medical grade substrates with fluorescein patterned onto a 3M™ Tegaderm™ patch and a Listerine® tab (**Fig. 5-9a, 5-9b**), fluorescein deposited onto a microneedle patch (*41, 42*) (**Fig. 5-9c**), and tamoxifen deposited onto borosilicate glass slide (**Fig. 5-9d**).

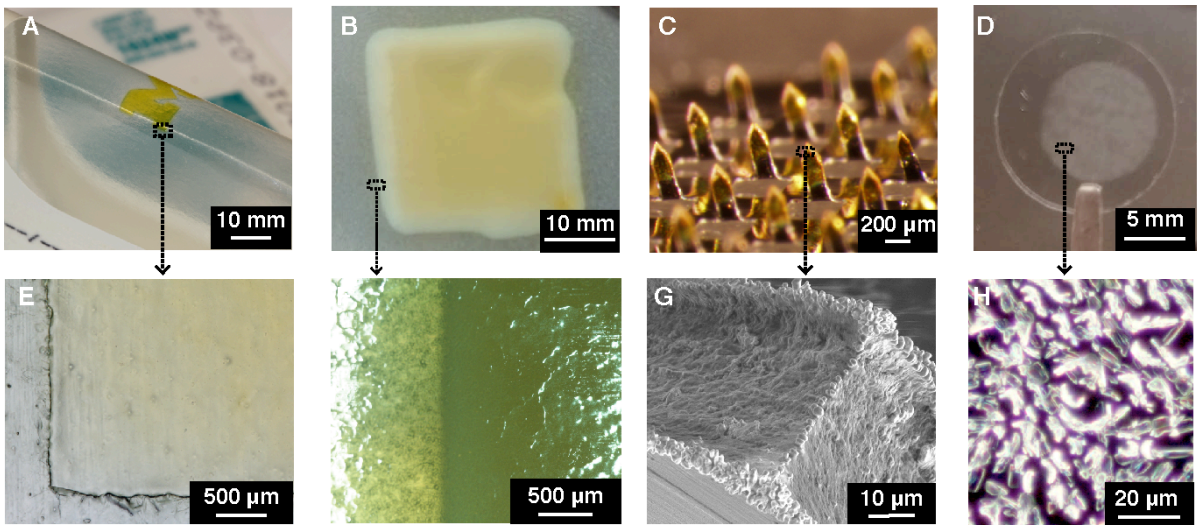

Figure 5-9 Examples of OVJP coating modes
(A), (E) Fluorescein on 3M™ Tegaderm™, (B), (F) Fluorescein on Listerin ®, (C), (G) Fluorescein printed on tips of stainless steel microneedles, (D), (H) Tamoxifen printed with OVJP onto borosilicate glass slides.

5.5 OVJP printed films characterization

5.5.1 Morphology characterization

An FEI Nova 200 Nanolab scanning electron microscope with accelerating voltage of 5-10 kV and current 0.1-0.5 nA was used to obtain the surface morphology images. Optical microscopy analysis was performed with Zeiss microscope (bright field, top-illumination).

Six different drugs - caffeine, paracetamol, ibuprofen, tamoxifen, fluorescein and BAY 11-7082 (BAY) - were characterized by thermogravimetric analysis (TGA) to determine their evaporation temperature and vapor pressure, establishing the conditions for deposition (i.e. flow rate of carrier gas, source temperature, and substrate temperature, as summarized in **Table 5-3**).

Then, 9 mm diameter circular films were deposited onto borosilicate glass slides (**Fig. 5-9d**) using identical nozzle geometry in each case, with the deposits characterized using x-ray diffraction, chemical analysis, and high resolution optical and electron microscopies.

The obtained film microstructures are shown in **Fig. 5-10**. All films were evaporated from original coarse powders with particle sizes approximately between 1-100 μm. The caffeine coating consisted of needle-like features whose diameter and length were 400±100 nm and 3±1 μm, respectively (**Fig. 5-10a**). Tamoxifen films consisted of continuous platelet-like features 800±100 nm and 500±100 nm in height and width, respectively (**Fig. 5-10b**). BAY 11-7082 films also consist of discrete platelets-like features 800±100 nm and 500±100 nm in height and width, respectively, and 5±2 μm in length (**Fig. 5-10c**). In the case of paracetamol and ibuprofen, 10 μm diameter, crystallized, interconnected droplets were obtained (**Fig. 5-10d**). We attribute the latter morphology to the fact that paracetamol and ibuprofen were deposited at temperatures

of 190 and 75 °C, respectively, which were 20 and 5 °C above their melting point; we hypothesize that adsorption on the substrate at these conditions is taking place *via* a transitory liquid phase, forming a continuous layer initially, followed by crystallization and dewetting, eventually forming the solid phase that retains a liquid-like appearance.

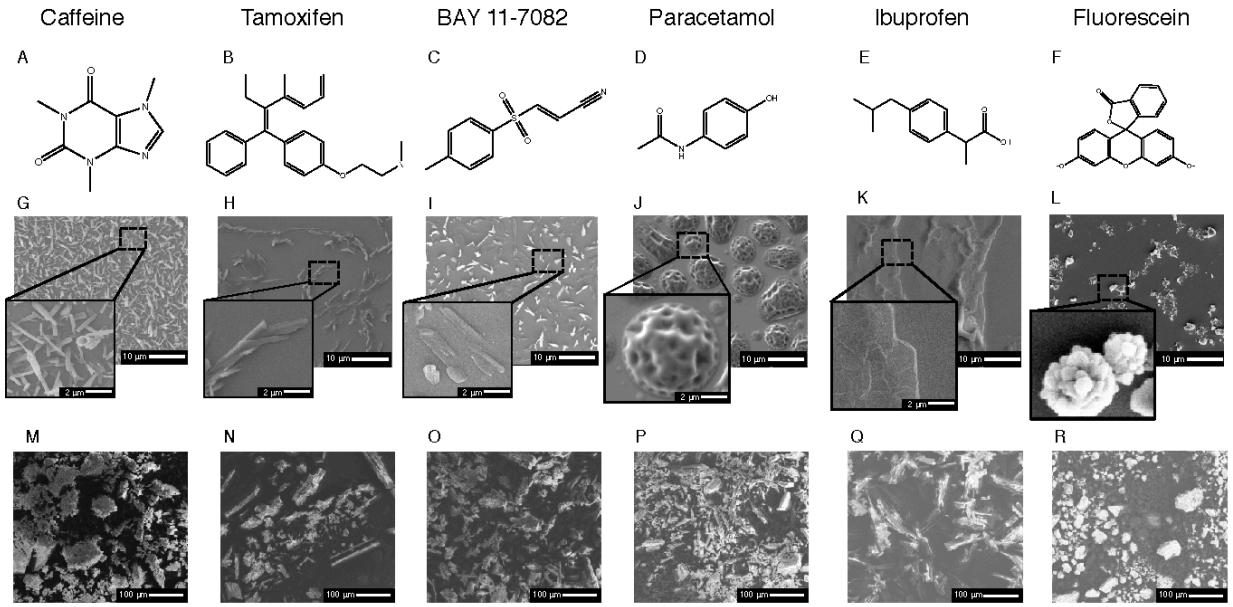

Figure 5-10 Drug films and powders microstructure

Chemical structure of: (A) Caffeine, (B) Tamoxifen, (C) BAY 11-7082, (D) Paracetamol, (E) Ibuprofen, (F) Fluorescein. Microstructure of OVJP deposited films: (G) Caffeine, (H) Tamoxifen, (I) BAY 11-7082, (J) Paracetamol, (K) Ibuprofen, (L) Fluorescein. Microstructure of original powder of: (M) Caffeine, (N) Tamoxifen, (O) BAY 11-7082, (P) Paracetamol, (Q) Ibuprofen, (R) Fluorescein.

5.5.2 Chemical characterization

To test the chemical stability of deposited substances, Fourier transform infrared spectroscopy (FTIR) was performed on BAY 11-7082 in film form and original drug form. Absorption spectra of BAY 11-7082 film and original powder showed similar peaks (**Fig. 5-11**), assuring that no material degradation occurred due deposition.

To further test the deposited substances, drug films were dissolved in methanol and analyzed by Ultra Performance Liquid Chromatography (UPLC), for comparison to as-received API powder. Similar retention times and peak structures were obtained for deposited films and the original powder samples, (**Fig. 5-12a-d**) suggesting that the OVJP process did not alter the chemical structure of API.

To determine the concentration of analyte, and to screen for degradation or impurities, drug powders and films were dissolved in methanol and run on a Waters Acquity H Class UPLC equipped with a Waters Acquity UPLC C18 column (2.1 x 100 mm). Drug powders were used as standards in all cases, and were diluted such that film samples fell within the range of standards. For all molecules the mobile phase was pumped at 0.3 mL/min, and consisted of A: ddH_2O + 0.1% Formic Acid and B: Methanol + 0.1% Formic Acid. The detection wavelength was set to 280 nm. Caffeine and Paracetemol were run isocratic at 100% B, while Tamoxifen and BAY had a gradient elution starting at A/B: 75/25, to 25/75 at 0.5 mins, steady through 5 mins, then returned to 75:25.

5.5.3 Structural characterization

Importantly for pharmaceutical applications, polymorphism can change drug effectiveness and functionality (*43, 44*). For this reason, the crystal structure of the API films was studied using synchrotron x-ray diffraction and compared to the structure of the original powder. Surface X-ray diffraction measurements of the films were performed at Sector 13-BM-C at the Advanced Photon Source, Argonne National Laboratory using a Newport 6-circle kappa diffractometer. Theta-2theta measurements were performed using a monochromatic X-ray beam of 15 keV and the diffracted intensity was collected using a Dectris Pilatus 100K pixel array detector. All measurements were performed in a helium rich environment to prevent rapid degradation of the

organic films. Diffraction measurements of powders were performed with Rigaku rotating anode XRD using monochromatic Cu-K-alpha x-ray source.

The diffraction patterns of films were in very good agreement with those of bulk powder used in the evaporation source, indicating that OVJP did not change the crystal structure / polymorph composition of the API (**Fig. 5-12e-h**). The average size of the crystallites, calculated using the Scherrer equation (*45*), was an order of magnitude smaller in the printed films (nanometers) than in the original powder (tens of nanometers), as shown in **Fig. 5-13**. We attribute this reduction upon printing to vapor supersaturation above the substrate, reducing the critical nucleus size in the formation of new crystallites throughout the deposition process.

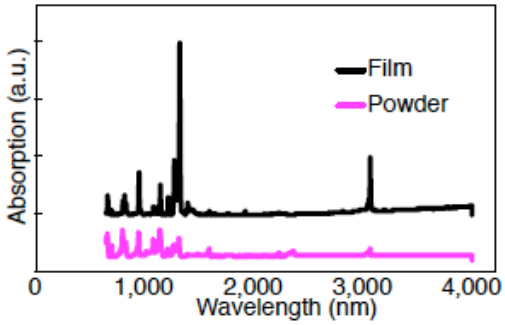

Figure 5-11 BAY 11-7082 film and powder FTIR absorption spectra

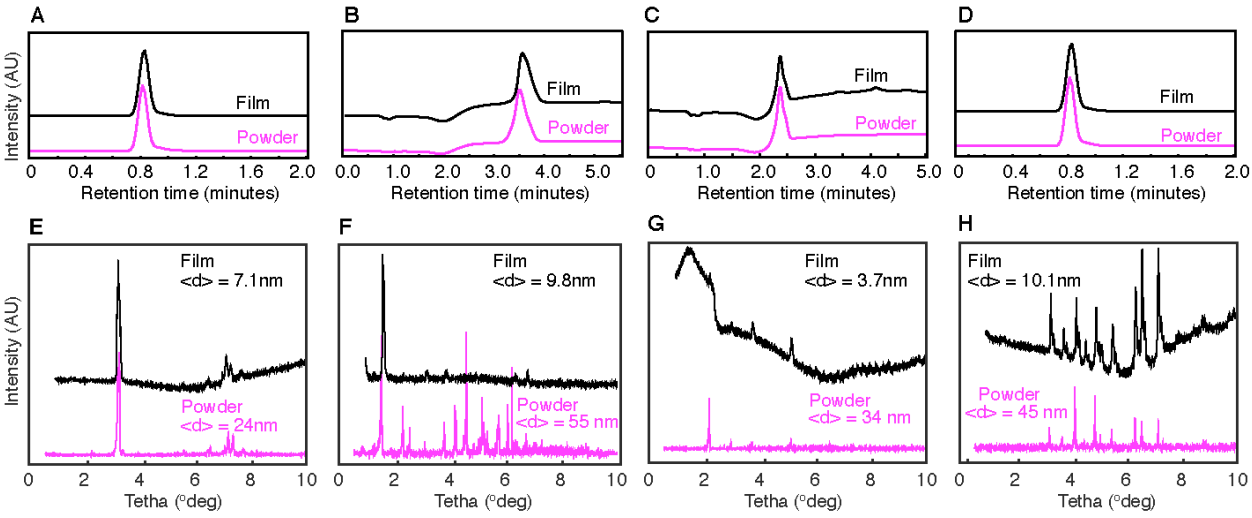

Figure 5-12 Drug films and powders chemical and structural characterization
UPLC of: (A) Caffeine, (B) Tamoxifen, (C) BAY 11-7082, (D) Paracetamol. XRD of : (E) Caffeine, (F) Tamoxifen, (G) BAY 11-7082, (H) Paracetamol.

To resolve the symmetry of the organic films, high-resolution Grazing-Incidence Wide-Angle X-ray Scattering (GIWAXS) measurements were performed. Using a PILATUS 100K area detector (*46, 47*), the intensity distribution was measured in a series of single scans along the out-of-plane direction as a set of two-dimensional reciprocal space slices. These were then used to reconstruct 3D reciprocal space maps (RSMs) (*48*). For each sample, the GIWAXS patterns were recorded at an angle of incidence of 0.1° and taken over a 2θ range of 5° to 45° (**Fig. 5-13, 5-14**).

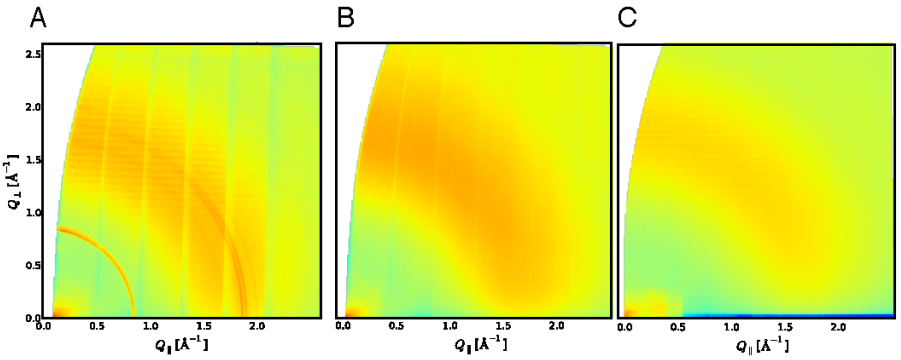

Figure 5-13 GIWAX patterns of different APIs deposited on glass substrates
GIWAXS patterns of (A) caffeine, (B) paracetamol and (C) ibuprofen films deposited on glass substrates. All films show nearly isotropic orientation with extremely broad and nearly uniform distribution of intensity for all rings in plane and out of plane. The broad rings suggest that caffeine, paracetamol and ibuprofen have a polycrystalline crystal structure when deposited on glass substrates. Qualitatively, caffeine films show the sharpest rings and are therefore more ordered than paracetamol and ibuprofen when deposited on glass.

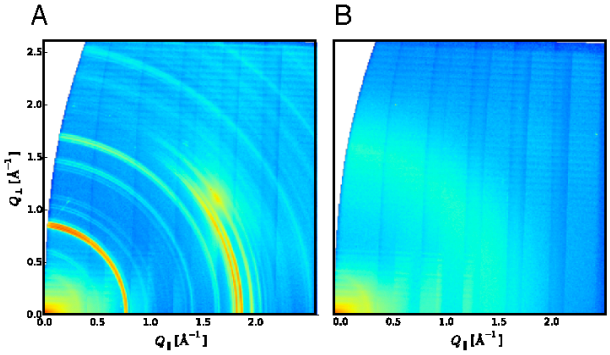

Figure 5-14 GIWAX patterns of different APIs deposited on silicon substrates
GIWAXS patterns of (A) caffeine and (B) paracetamol films deposited on silicon substrates. In the low $Q_{||}$ range, the caffeine film shows fairly isotropic orientation with slight preferential ordering out of plane but a mostly uniform distribution of intensity along powder rings. Preferential texturing is observed in plane at $Q_{||} = 1.8$ Å^{-1} with ring stacks oriented along an axis parallel to the substrate and no observed texturing along the direction perpendicular to the substrate. The caffeine film exhibits sharper and thinner polycrystalline rings than the paracetamol and ibuprofen films, indicating more texturing. The paracetamol film shows a broader powder ring than the caffeine film with uniform distribution of intensity, suggesting that the paracetamol films deposited on silicon are less ordered than the caffeine films.

FTIR spectra of BAY 11-7082 film and the original powder is demonstrated in

5.6 Dissolution studies

The theory of dissolution process was described in section *5.1.6*, Eq, 5.1. Since fluid motion near the surface, degree of agitation and viscosity of the fluid will have an effect on boundary layer thickness, δ, standardized dissolution system need to be used in order to characterize the dissolution process. The most common one is rotating disk system (*49*). In this setup the powder is compressed into a pellet at a force just high enough to mechanically lock the particles to prevent pellet disintegration during the dissolution test. The disk is rotated at defined speed and solution temperature.

5.6.1 Boundary layer thickness of rotating disk

Schematic picture of rotating disk and flow structure above rotating disk is shown in **Fig. 5-15**.

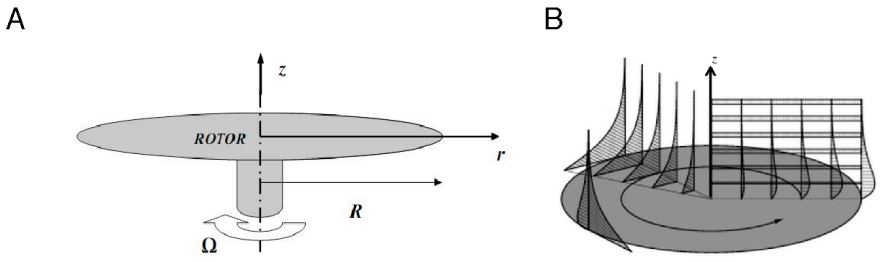

Figure 5-15 Flow structure near rotating disk

The nature of the flow over a rotating disk is related to local Reynolds number Re_r:

$$\mathrm{Re}_r = \frac{\Omega r}{\upsilon} \quad (5.6)$$

where Ω is the rotational speed (1/sec), r (m) - radial distance from disk center and υ ($m^2\,sec^{-1}$) is liquid kinematic viscosity. The flow becomes unstable when the rotational velocity and/or radius over the disk are high enough. At conditions used in dissolution of drugs tests at the edge of disk of radius 5 mm rotating at 100 rpm (10.5 rad/sec) in water, Re_r is ~500, therefore the flow regime is laminar at disk edge (*50*).

Velocity profile at cylindrical coordinates can be written as:

$$\delta = 1.61 D^{1/3} \Omega^{-1/2} \upsilon^{1/6} \quad (5.7)$$

At the disk surface (z=0), v_r=0, v_z=0 and v_Φ=Ωr. This implies that the solution is dragged along the disk surface at angular velocity Ω. This problem was treated by Von Karman and Cochran (*51*) yielding a hydrodynamic boundary layer thickness which represents the thickness of layer of liquid dragged by the rotating disk:

$$y_h = 3.6\sqrt{(\upsilon / \Omega)} \quad (5.8)$$

For water at 100 rpm y_h would be ~1mm. Once velocity profile is known, convective-diffusion equation can be solved (2nd Fick's law):

$$\frac{\partial C_j}{\partial t} = D_j \nabla^2 C_j - v \cdot \nabla C_j \quad (5.9)$$

At steady state, and due to symmetry the equation can be simplified, leading to analytical solution, and boundary layer thickness is given by Levich equation (*52*):

$$\delta = 1.61 D^{1/3} \Omega^{-1/2} \upsilon^{1/6} \quad (5.10)$$

5.6.2 Dissolution of loose powder

In case of loose powder or disintegrating tablet with various additives, the situation is more complex than dissolution from compressed powder pellet and no analytical solution exists. The Hixson and Crowell model (*53*) is a simplified solution to Eq. 5.11, often used for characterizing powder dissolution kinetics (also called a "cubic law"):

$$C = \frac{N}{V}\left[Mp_0 - \left(Mp_0^{1/3} - \left(\left(\frac{4\pi}{3\rho^2} \right)^{1/3} \frac{DC_s}{3\delta} \right)^3 t \right) \right] \quad (5.11)$$

where N is the number of powder particles, Mp_0 is particles' initial weight, ρ is solute density. H-C model includes only change in particle surface area; active contact area in powder dissolution which is changing during the process, affected by changing particle size and shape, wettability and tendency to agglomerate are not included in the model (*54*). Therefore the model is only appropriate for estimating initial dissolution rates, before agglomeration or substantial change in particle size and shape occurs.

Weibull (1951) (*55*) proposed an empirical model to analyze the dissolution behavior. Higuchi (*56*) developed several theoretical models to study the release of water soluble and low soluble drugs incorporated in semi-solid and/or solid matrixes based on Fick's 1st law of diffusion. Additional models were summarized by Costa et *al. (57)*.

5.7 Dissolution of OVJP printed films

Dissolution setup for films is shown in **Fig. 5-16**. In case of dissolution from film, the glass substrate was attached to substrate holder (**Fig. 5-16c**). The substrate holder is attached to rotating rod. In case of compressed powder pellet, 1.57 mm diameter pellet was compressed at 50 ± 2 psi for ~10 seconds into a holder having same size as disk substrate holder (**Fig. 5-16b**). In case of loose powder, the weighed powder was demonstrated into solution and stirred with

blank substrate holder at 100 rpm. In all cases the same vessel and solution volume of 10ml was used (**Fig. 5-16a**). Testing temperature was room temperature - 20±1 °C.

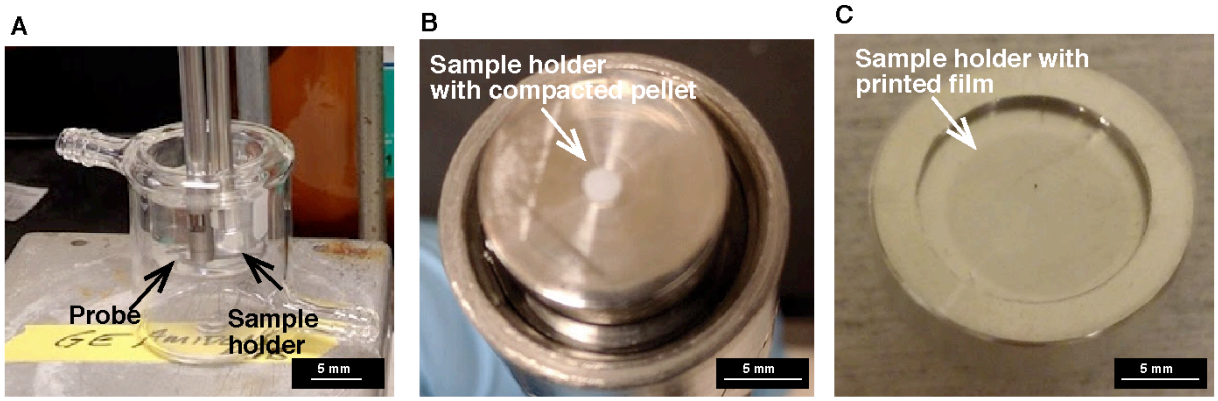

Figure 5-16 Experimental setup used in API dissolution rate studies
(A) Dissolution vessel with optical probe and sample holder. The rod is rotating at 100 rpm speed. (B) Sample holder for miniaturized compressed powder pellet (C) Sample holder for circular substrate with printed film.

Drug dissolution was monitored by *in-situ* UV-VIS Ocean Optics USB +2000 spectrometer with T300-UV-VIS transmission dip probe, with a 10 mm optical path. Solution absorbance was recorded with frequency of 2-60 sec^{-1} for duration of 20 min - 12 hours (depending on substance dissolution rate- fast dissolution rate was recorded at higher frequencies).

OVJP enables the small molecular API to be formed as a continuous film. Although the surface profile may indeed exhibit nano-scale roughness, this fine scale roughness serves mostly to more quickly establish a "virtual surface" - i.e. a concentration boundary layer, which remains relatively constant throughout the dissolution process, and therefore opens a new, simplified way of controlling and studying the dissolution process of a drug. For OVJP-deposited API films, Eq. 5.4 therefore simplifies to:

$$C = C_s(1 - \exp^{-\frac{DAt}{V\delta}}) \quad (5.12)$$

For the "sink" condition ($C<<C_s$), the dissolution rate becomes essentially constant, precisely controlled by the film's projected area. (**Fig. 5-18d.**)

Below, we will compare the dissolution kinetics of APIs in powder form to those of films printed by OVJP. We will use the equations above to fit the dissolution data, and discuss the key differences, showing that for drugs printed as films these limitations do not exist. We then go on to show how this outcome can be beneficial in the dosing of poorly soluble drugs in a biological system.

The dissolution kinetics of three materials having relatively poor aqueous solubility were studied: fluorescein in deionized water (*58*), ibuprofen in aqueous hydrochloride (HCl) buffer (pH=1.2) solution (*59*), and tamoxifen in aqueous acetate buffer solution (*60*) (pH=4.9).

First, the solubility of these compounds in corresponding solvents was measured at 20±1 $^{\circ}$C solution temperature. Solutions with excess concentration (at least 100 μg/ml of solid) were shaken at ~1000 rpm for 48 hours, followed by solution filtration with 0.4 μm filter after 24 hrs. Filtered solutions concentrations were then measured using UV-VIS spectrometry, calibrated with known solutions concentrations. 5 different concentrations for calibration were used in each test. The concentrations used were as follows: for fluorescein in dionized water - 1, 2, 3, 4, 5 μg/ml, ibuprofen in HCl pH 1.2 buffer: 2, 4, 6, 8, 10 μg/ml, tamoxifen in acetate buffer pH 4.9: 1, 2, 4, 6, 10 μg/ml, BAY in buffer pH 7.4: 2, 4, 6, 10, 20 μg/ml.

The saturation limit for fluorescein in deionized water was measured to be 10±0.5 μg/ml, for ibuprofen in HCl 22.5±0.5 μg/ml, and for tamoxifen in acetate 23.6±0.5 μg/ml. To measure dissolution kinetics, a rotating disk dissolution apparatus (**Fig. 5-16**) was used with rotational speed of 100 rpm. Concentration was monitored using a UV-VIS spectrometer equipped with a dip probe. The compounds were tested both in powder form (compressed into pellets for rotating

disk dissolution) and in film form. The intrinsic dissolution rate (*IDR*) of the films was compared to the dissolution rate of powder compressed into 1.57 mm diameter pellets of ~4 mm thickness (*61*) (**Fig. 5-16b**), while the printed films comprised 9 mm diameter circles on borosilicate glass disks (**Fig. 5-16c**[6]). [7]Film weights were in the range 5-80 μg. Identical rotation rod and sample attachments were used (**Fig. 5-16a**)**,** assuring that hydrodynamic boundary layer thickness is same for compressed powder and deposited film. Solution volume remained constant in all experiments, 10 ml, and temperature was 20±1 $^{\circ}$C. In all cases intrinsic dissolution of films was comparable to one of compressed pellets ($3\cdot10^{-5} \pm 5\cdot10^{-6}$ for fluorescein, $1\cdot10^{-3} \pm 3\cdot10^{-4}$ for ibuprofen, $6\cdot10^{-4} \pm 1\cdot10^{-4}$ for tamoxifen, all values in (μg sec^{-1} mm^{-2}))). The *IDR* is defined as:

$$IDR = \frac{(dm/dt)_{\max}}{A} \quad (5.13)$$

where m is the dissolved solute mass, and $(dm/dt)_{max}$ is the maximum slope in the dissolution curve, plotting the amount of material in the solution versus time, typically evaluated at the start of dissolution process where the concentration driving force is highest. *IDR* is an intrinsic property of a dissolving material, which depends on the material's degree of crystallinity, crystalline and chemical structures. In case of printed films, IDR is essentially unaltered, indicating that material chemical and structural form was not altered either, corroborating XRD and UPLC results.

Figure 5-17 demonstrates how the dissolution rate of films can be controlled *via* film thickness and deposit area. For example, keeping film area constant, while varying the thickness of the fluorescein film (**Fig. 5-17a**), we observe identical IDRs, while the saturation concentration increases linearly with film thickness; this is confirmed by plotting the right hand side (RHS) of Eq. 5.12 in **Fig. 5-17c**. **Figure 5-17b** shows how concentration varies with deposit area, while keeping the thickness constant. The concentration evolves essentially linearly with time, with the

slope proportional to the deposit area, as indicated by a linear fit in **Fig. 5-17d**, from which the IDR can be extracted. The dissolution rate scales linearly with film area, as predicted by Eq. 5.12.

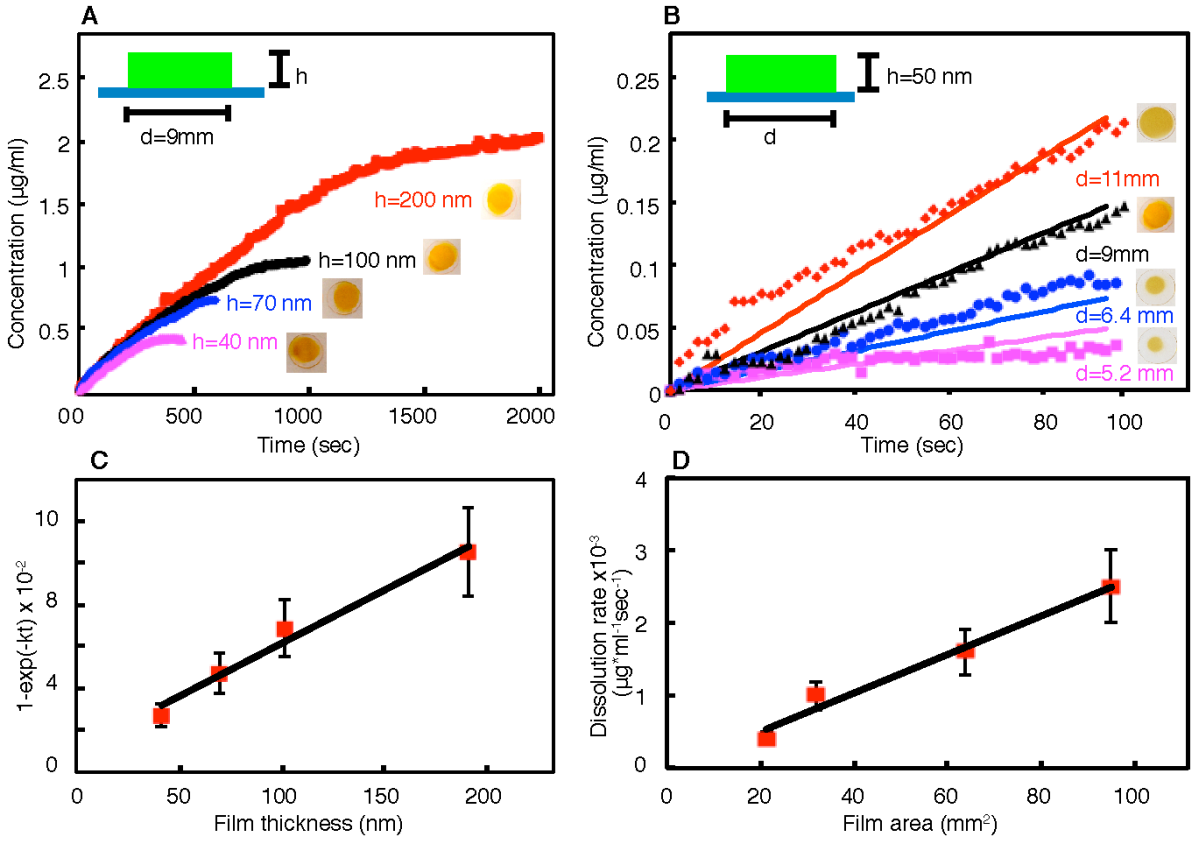

Figure 5-17 Example of controlled dissolution in fluorescein films
Effect of varying film thickness (A) or film area (B) on dissolution profiles of fluorescein films in deionized water. (C) Dependence of (*1-exp(-kt)*) (Eq. 5.2) on film thickness. Numbers were extracted from data in plot (A). (D) Films dissolution rate vs. film area. The rates were extracted from data in plot (B). Error bars correspond to measurement of average (n=3) ± STDEV.

As-received powder-form materials having the same weight as the films also were introduced into 10 ml solutions without any prior treatment, and stirred using rotation rod with same shape and diameter as the one used for film dissolution. **Figures 5-18a-c** demonstrate the dissolution behavior of films versus original loose powders, clearly showing that the initial dissolution rates in films is very rapid and constant up to ~80% of the film being dissolved. The dissolution rate is

diminished for the remaining material mainly due to reduction in film area (i.e. loss of complete coverage due to material that has dissolved). The initial dissolution rates observed for film-form materials versus loose powders are enhanced ten-fold for fluorescein, thirty-fold for ibuprofen, and ten-fold for tamoxifen. As hypothesized, the initial enhancement in dissolution rate is attributed mainly to the enhancement of surface area of the film, while the IDR or ultimate solubility remain constant. The order of enhancement is in good agreement with the order of enhancement of surface area relative to that of powders. Importantly, film dissolution accurately follows predictions until almost complete dissolution, whereas in the case of powders, the dissolution rate is less predictable due to changes in particle shape and agglomeration (*27*) over time, clearly present for example in the dissolution of ibuprofen powder (**Fig. 5-18b**). **Figure 5-18d** schematically represents the dissolution process differences between the film and a powder, focusing on the important difference between the actual surface area of the material, the surface area of the material that is projected (i.e. when viewed from the "top"), and a virtual surface of the material corresponding to the concentration boundary layer. As represented in the concentration profiles in **Fig. 5-18d**, it is likely that the very high surface area of the vapor deposited films leads to relatively fast establishment of an equilibrium-limited concentration in the boundary layer above the surface, maximizing the driving force for dissolution.

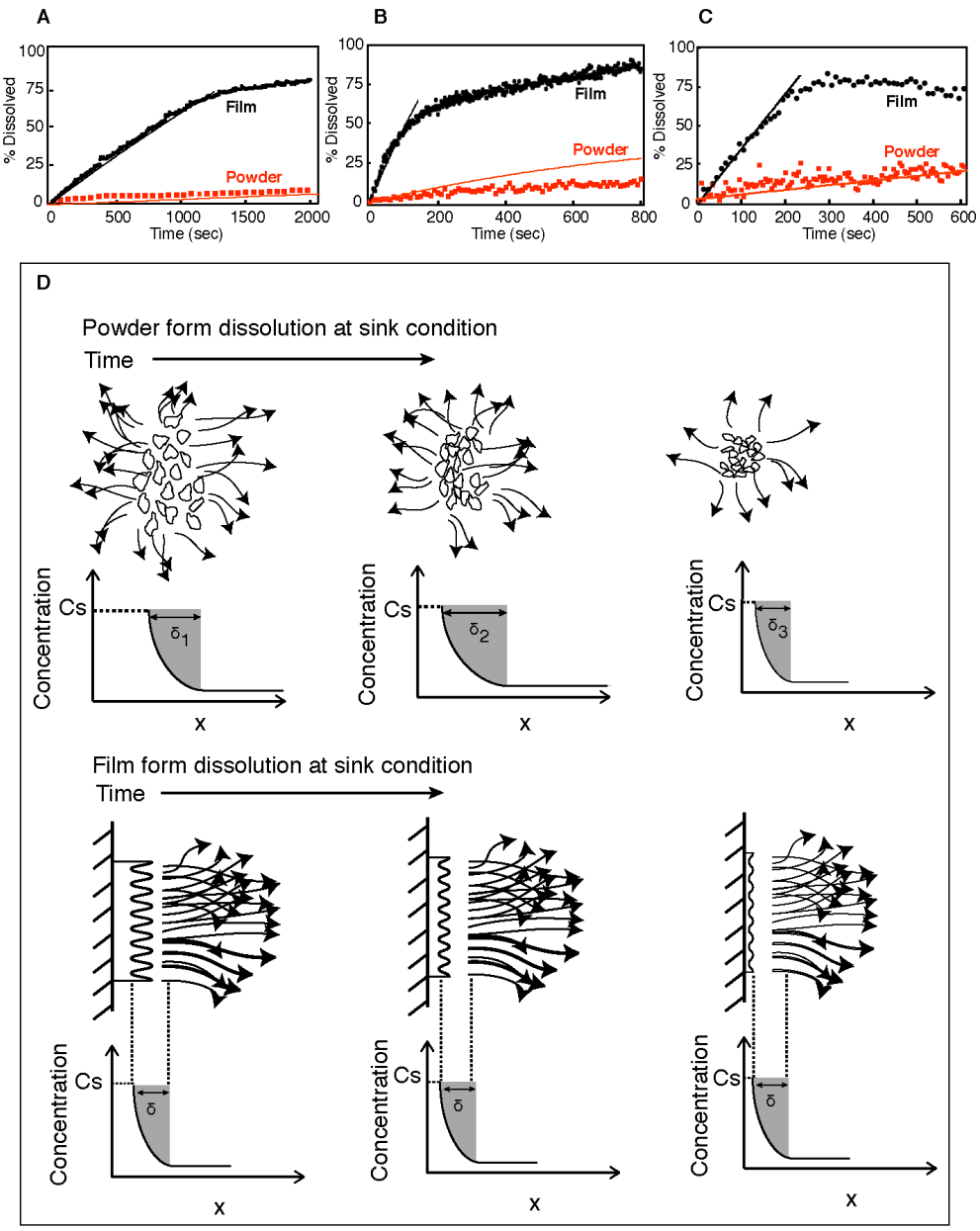

Figure 5-18 Dissolution profiles of films and powders

Dissolution profiles of films and original powders (dotted line - experimental values. Solid lines - theoretical prediction according to Eq. 5.2 for film and Eq. 5.3 for powder): (A) Fluorescein in deionized water- 25 µg weight. (B) Ibuprofen in aqueous HCl buffer pH 1.2. - 70 µg weight. (C) Tamoxifen acetate buffer pH 4.9 - 6 µg weight. (D) Schematic representation of dissolution of a powder form and film form of a drug. In case of powder, the surface area and diffusion boundary layer thickness (δ) are changing during dissolution time, therefore the flux of dissolved molecules into solution is not constant. In case of a film, only film thickness is changing, while the area of a film and boundary layer thickness remain constant. No powder agglomeration occurs during dissolution and dissolved material flux is constant.

To determine in a controlled manner whether enhanced API dissolution rates translate effectively to the API's action on live cells, two different cancer cell lines (ovarian carcinoma, OVCAR3, and breast carcinoma, MCF7) in growth medium were exposed to tamoxifen films and BAY-11-7082 films printed on glass slides (**Fig. 5-19**).

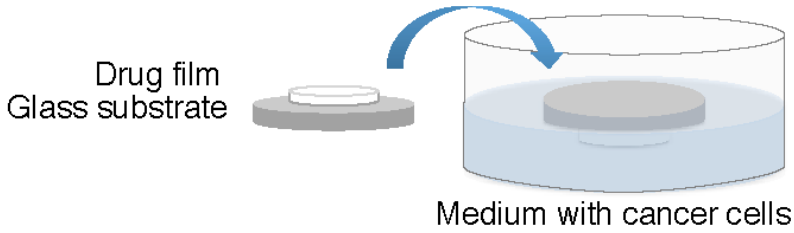

Figure 5-19 Schematic of drug application for cancer cell growth study.
Films printed on glass substrates were immersed into cell growth medium. After 1 hour of agitation, the glass film was removed.

The cells were plated onto 12-well tissue culture dishes, and allowed to adhere and grow for 24 hours in 2.5 ml of 10% fetal bovine serum-supplemented growth medium. Tamoxifen and BAY-11-7082 films were inverted and placed onto the surface of the growth media, and released from the substrate *via* gentle, intermittent manual agitation over the course of 1 hour. Slides were removed following this initial period, and live cell counts were determined using trypan blue exclusion using a hemocytometer at 1, 4, 8, 12, 24 and 48 hours following film treatment. At least 3 samples were tested at each time point. Growth inhibition curves were also generated using the following controls: i) Clean glass slides with no deposited drug film as a sham control; ii) 5 µM tamoxifen or 500 nM BAY-11-7082 dissolved in dimethyl sulfoxide (DMSO; conventional drug dose); iii) tamoxifen or BAY powders dissolved directly in sterile supplemented growth medium. In all cases, the amount of the introduced drug was calculated such that the nominal concentration of the treatment was 5 µM (1.8 µg/ml) for tamoxifen (4.5 µg per film) and 500 nM (0.1 µg/ml) for BAY 11-7082 (0.25 µg per film).

Figure 5-20 demonstrates cancer cell count curves treated with the different drug forms. All data points in the plots are an average of at least three film samples. In both cases, cells treated with film-form drug showed significantly reduced viability, comparable to when the drug was predissolved in DMSO. MCF7 cancer cells' viability after 48 hours was 58% for film form and 79% for powder form treatment (**Fig. 5-20a**), and OVCAR3 cancer cells' viability after 48 hours was 44% for film form and 68% for powder form treatment (**Fig. 5-20b**). BAY-11-7082 films exhibited similar effectiveness as the powdered drug dissolved in growth medium (**Fig. 5-20c,d**).

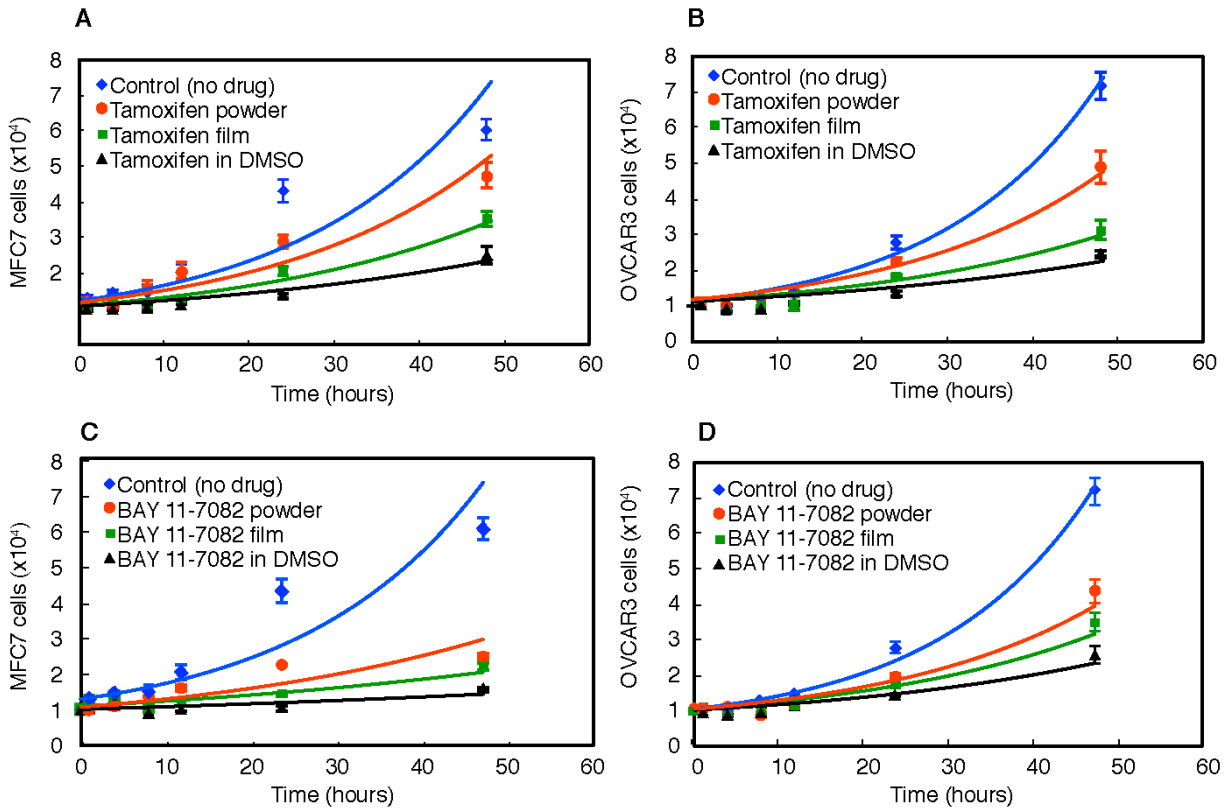

Figure 5-20 Cell growth studies
Cell growth profile (solid line - eye guide): (**A**) MCF7 cells treated tamoxifen, (**B**) OVCAR3 cells treated with tamoxifen, (**C**) MCF7 cells treated with BAY 11-7082, (**D**) OVCAR3 cells treated with BAY 11-7082.

The lower effectiveness of powder-form dosing in tamoxifen is attributed to a lower powder dissolution rate, which results in a much lower effective concentration of drug relative to what is

obtained from the film form[8]. Example of micrographs used for cancer cell population counts used in determining the growth curves is shown in **Fig. 5-21**.

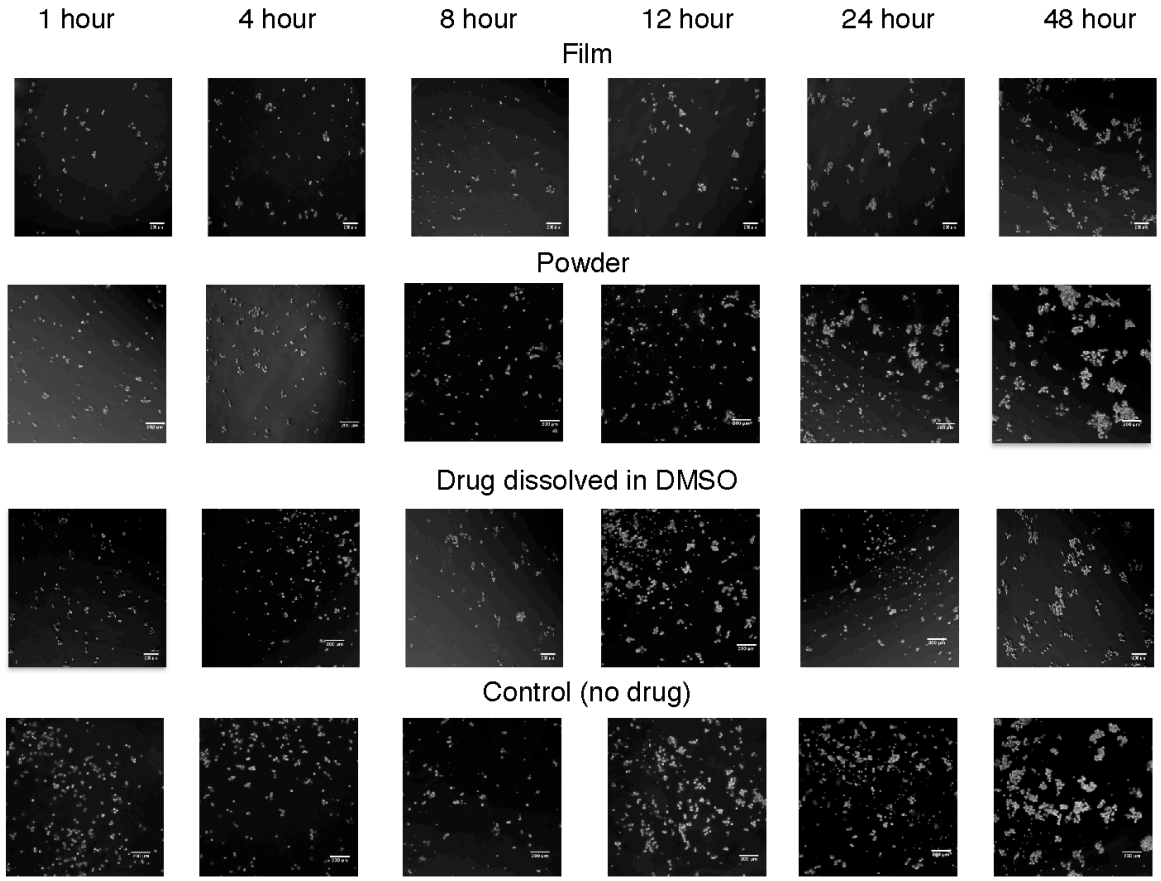

Figure 5-21 MCF7 cancer cells treated with different forms of tamoxifen.
After 48 hours cancer cell growth is clearly more effectively inhibited by film form drug than by drug in original powder form.

5.8 Summary

In conclusion, we report on the ability to print, without solvents, small molecular pharmaceutical ingredients to obtain high surface area films having nanocrystalline morphology. These printed films exhibit substantially enhanced dissolution kinetics compared with their bulk powder form. Drug films printed in this manner (shown here for tamoxifen and BAY-11-7082) exhibit enhanced cancer cell-killing properties *in vitro* without having to predissolve them in organic

solvents, such as DMSO. While amorphous dispersions have been used to increase the APIs' solubility, their stability remains questionable (*62*), while the polycrystalline nature of the printed films suggests a promising avenue for breaking the trade-off between stability and dissolution rates. More generally, the capabilities demonstrated here potentially allow for the determination of more realistic effectiveness of poorly soluble drugs prior to *in vivo* studies. The ability to deposit small molecular drugs from their pure form, as films and without the use of solvents, opens a new approach to drug screening and manufacturing, where accurate dosage, chemical and structural stability, and processing flexibility are needed without hindering drug functionality. We therefore anticipate benefits for: (a) early stage drug discovery - enabling eliminating the need for organic solvents for poorly soluble drugs during screening processes, (b) development of drug delivery vehicles - e.g., films for transdermal drug delivery, directly coated patches, microneedles, encapsulated dissolvable films or implants, and (c) administration of high potency APIs (HPAPIs) with accurate and individualized dosing and nanogram-level accuracy without compromising safety during manufacturing. The technique demonstrated here also enables continuous manufacturing, where films and polymers can be alternately deposited (*63, 64*) to obtain desired dosage availability, and versatile formulation, eliminating the need for mixing and powder preparation.

5.9 References

1. M. S. Kinch, A. Haynesworth, S. L. Kinch, D. Hoyer, An overview of FDA-approved new molecular entities: 1827–2013. *Drug Discovery Today* **19**, 1033 (2014).
2. http://www.fda.gov/ForPatients/Approvals/Drugs/default.htm
3. J. Samanen, Similarities and differences in the discovery and use of biopharmaceuticals and small-molecule chemotherapeutics. *Introduction to biological and small molecule drug research and development, theory and case studies*, 161 (2013).
4. K. T. Savjani, A. K. Gajjar, J. K. Savjani, Drug solubility: importance and enhancement techniques. *ISRN pharmaceutics* **2012**, (2012).
5. E. M. Hoffmann, A. Breitenbach, J. Breitkreutz, Advances in orodispersible films for drug delivery. *Expert Opinion on Drug Delivery* **8**, 299 (2011).

6. J. B. Wolinsky, Y. L. Colson, M. W. Grinstaff, Local drug delivery strategies for cancer treatment: Gels, nanoparticles, polymeric films, rods, and wafers. *Journal of Controlled Release* **159**, 14 (2012).
7. M. Rathbone, S. Senel, I. Pather, *Oral Mucosal Drug Delivery and Therapy*. Springer US (2015).
8. L. A. Felton, S. C. Porter, An update on pharmaceutical film coating for drug delivery. *Expert Opinion on Drug Delivery* **10**, 421 (2013).
9. A. Adamo *et al*., On-demand continuous-flow production of pharmaceuticals in a compact, reconfigurable system. *Science* **352**, 61 (2016).
10. S. Mascia *et al*., End-to-End Continuous Manufacturing of Pharmaceuticals: Integrated Synthesis, Purification, and Final Dosage Formation. *Angewandte Chemie International Edition* **52**, 12359 (2013).
11. I. Kola, J. Landis, Can the pharmaceutical industry reduce attrition rates? *Nature Reviews Drug Discovery* **3**, 711 (2004).
12. L. Hutchinson, R. Kirk, High drug attrition rates - where are we going wrong? *Nature Reviews Clinical Oncology* **8**, 189 (2011).
13. J. DiMasi, H. Grabowski, R. Hansen, Cost to develop and win marketing approval for a new drug is $2.6 billion. *Tufts Center for the Study of Drug Development* **18**, (2014).
14. M. Matthews, The high cost of inventing new drugs—and of not inventing them. *Innovative Insights on Today's Policy Debates*, (2015).
15. W. Bains, Failure rates in drug discovery and development-will we ever get any better? *Drug Discovery World* **5**, 9 (2004).
16. M. Kakran, L. Li, R. H. Müller, Overcoming the challenge of poor drug solubility. *Pharm Eng* **32**, 1 (2012).
17. C. A. Lipinski, F. Lombardo, B. W. Dominy, P. J. Feeney, In Vitro Models for Selection of Development Candidates Experimental and computational approaches to estimate solubility and permeability in drug discovery and development settings. *Advanced Drug Delivery Reviews* **23**, 3 (1997).
18. G. L. Amidon, H. Lennernäs, V. P. Shah, J. R. Crison, A Theoretical Basis for a Biopharmaceutic Drug Classification: The Correlation of in Vitro Drug Product Dissolution and in Vivo Bioavailability. *Pharmaceutical Research* **12**, 413 (1995).
19. H. D. Williams *et al*., Strategies to Address Low Drug Solubility in Discovery and Development. *Pharmacological Reviews* **65**, 315 (2013).
20. D. E. Wurster, P. W. Taylor, Dissolution rates. *Journal of Pharmaceutical Sciences* **54**, 169 (1965).
21. A. A. Noyes, W. R. Whitney, The rate of solution of solid substances in their own solutions. *Journal of the American Chemical Society* **19**, 930 (1897).
22. N. Blagden, M. de Matas, P. T. Gavan, P. York, Crystal engineering of active pharmaceutical ingredients to improve solubility and dissolution rates. *Advanced Drug Delivery Reviews* **59**, 617 (2007).
23. J.-U. A. H. Junghanns, R. H. Müller, Nanocrystal technology, drug delivery and clinical applications. *International Journal of Nanomedicine* **3**, 295 (2008).
24. R. Mauludin, R. H. Müller, C. M. Keck, Kinetic solubility and dissolution velocity of rutin nanocrystals. *European Journal of Pharmaceutical Sciences* **36**, 502 (2009).

25. B. Van Eerdenbrugh, G. Van den Mooter, P. Augustijns, Top-down production of drug nanocrystals: Nanosuspension stabilization, miniaturization and transformation into solid products. *International Journal of Pharmaceutics* **364**, 64 (2008).
26. L. Wu, J. Zhang, W. Watanabe, Physical and chemical stability of drug nanoparticles. *Advanced Drug Delivery Reviews* **63**, 456 (2011).
27. K. M. Karry-Rivera, Flexible continuous manufacturing platforms for solid dispersion formulations, Thesis, Rutgers University-Graduate School-New Brunswick (2015).
28. S. M. Krull *et al*., Polymer strip films as a robust, surfactant-free platform for delivery of BCS Class II drug nanoparticles. *International Journal of Pharmaceutics* **489**, 45 (2015).
29. K. Ita, Transdermal Delivery of Drugs with Microneedles—Potential and Challenges. *Pharmaceutics* **7**, 90 (2015).
30. V. F. Patel, F. Liu, M. B. Brown, Advances in oral transmucosal drug delivery. *Journal of Controlled Release* **153**, 106 (2011).
31. Y. Sudhakar, K. Kuotsu, A. K. Bandyopadhyay, Buccal bioadhesive drug delivery — A promising option for orally less efficient drugs. *Journal of Controlled Release* **114**, 15 (2006).
32. S. Bose, R. H. Bogner, Solventless Pharmaceutical Coating Processes: A Review. *Pharmaceutical Development and Technology* **12**, 115 (2007).
33. Particle Sciences - Technical Brief. **3**, 1 (2010).
34. R. Daly, T. S. Harrington, G. D. Martin, I. M. Hutchings, Inkjet printing for pharmaceutics – A review of research and manufacturing. *International Journal of Pharmaceutics* **494**, 554 (2015).
35. B. Derby, Inkjet Printing of Functional and Structural Materials: Fluid Property Requirements, Feature Stability, and Resolution. *Annual Review of Materials Research* **40**, 395 (2010).
36. C. R. Ganellin, R. Jefferis, S. M. Roberts, *Introduction to Biological and Small Molecule Drug Research and Development: theory and case studies*. Elsevier Science (2013).
37. H. Chen, C. Khemtong, X. Yang, X. Chang, J. Gao, Nanonization strategies for poorly water-soluble drugs. *Drug Discovery Today* **16**, 354 (2011).
38. P. Li, L. Zhao, Developing early formulations: Practice and perspective. *International Journal of Pharmaceutics* **341**, 1 (2007).
39. V. C. Jordan, Tamoxifen: a most unlikely pioneering medicine. *Nat Rev Drug Discov* **2**, 205 (2003).
40. O. Shalev *et al*., Growth and modelling of spherical crystalline morphologies of molecular materials. *Nat Commun* **5**, (2014).
41. H. Khan, P. Mehta, H. Msallam, D. Armitage, Z. Ahmad, Smart microneedle coatings for controlled delivery and biomedical analysis. *Journal of Drug Targeting* **22**, 790 (2014).
42. Y. Ma, H. S. Gill, Coating Solid Dispersions on Microneedles via a Molten Dip‐Coating Method: Development and In Vitro Evaluation for Transdermal Delivery of a Water‐Insoluble Drug. *Journal of Pharmaceutical Sciences* **103**, 3621 (2014).
43. R. Censi, P. Di Martino, Polymorph Impact on the Bioavailability and Stability of Poorly Soluble Drugs. *Molecules* **20**, 18759 (2015).
44. N. Rodríguez-hornedo, D. Murphy, Significance of controlling crystallization mechanisms and kinetics in pharmaceutical systems. *Journal of Pharmaceutical Sciences* **88**, 651 (1999).
45. B. E. Warren, *X-ray Diffraction*. Dover Publications (1969).

46. C. M. Schleputz *et al*., Improved data acquisition in grazing-incidence X-ray scattering experiments using a pixel detector. *Acta Crystallographica Section A* **61**, 418 (2005).
47. P. Kraft *et al*., Performance of single-photon-counting PILATUS detector modules. *Journal of Synchrotron Radiation* **16**, 368 (2009).
48. C. M. Schleputz, S. O. Mariager, S. A. Pauli, R. Feidenhans'l, P. R. Willmott, Angle calculations for a (2+3)-type diffractometer: focus on area detectors. *Journal of Applied Crystallography* **44**, 73 (2011).
49. Intrinsic dissolution. *US Pharmacopeia National Formulary* **29**, 2923 (2006).
50. S. Harmand, J. Pellé, S. Poncet, I. V. Shevchuk, Review of fluid flow and convective heat transfer within rotating disk cavities with impinging jet. *International Journal of Thermal Sciences* **67**, 1 (2013).
51. W. G. Cochran, The flow due to a rotating disc. *Mathematical Proceedings of the Cambridge Philosophical Society* **30**, 365 (1934).
52. V. G. Levich, *Physicochemical hydrodynamics: (by) veniamin G. Levich. Transl. by scripta technica, inc*. Prentice-Hall (1962).
53. A. W. Hixson, J. H. Crowell, Dependence of Reaction Velocity upon Surface and Agitation. *Industrial & Engineering Chemistry* **23**, 1160 (1931).
54. Y. Wang, B. Abrahamsson, L. Lindfors, J. G. Brasseur, Comparison and Analysis of Theoretical Models for Diffusion-Controlled Dissolution. *Molecular Pharmaceutics* **9**, 1052 (2012).
55. F. Langenbucher, Letters to the Editor: Linearization of dissolution rate curves by the Weibull distribution. *Journal of Pharmacy and Pharmacology* **24**, 979 (1972).
56. T. Higuchi, Rate of Release of Medicaments from Ointment Bases Containing Drugs in Suspension. *Journal of Pharmaceutical Sciences* **50**, 874 (1961).
57. P. Costa, J. M. Sousa Lobo, Modeling and comparison of dissolution profiles. *European Journal of Pharmaceutical Sciences* **13**, 123 (2001).
58. W. M. Dehn, Comparative solubilities in water, in pyridine and in aqueous pyridine. *Journal of the American Chemical Society* **39**, 1399 (1917).
59. L. R. Shaw, W. J. Irwin, T. J. Grattan, B. R. Conway, The Effect of Selected Water-Soluble Excipients on the Dissolution of Paracetamol and Ibuprofen. *Drug Development and Industrial Pharmacy* **31**, 515 (2005).
60. C. M. Buchanan *et al*., Solubilization and dissolution of tamoxifen-hydroxybutenyl cyclodextrin complexes. *Journal of Pharmaceutical Sciences* **95**, 2246 (2006).
61. Y.-C. Tseng, M. Patel, Y. Zhao, Determination of intrinsic dissolution rate using miniaturized rotating and stationary disk systems. *Dissolution Technologies* **21**, 24 (2014).
62. S. Baghel, H. Cathcart, N. J. O'Reilly, Polymeric Amorphous Solid Dispersions: A Review of Amorphization, Crystallization, Stabilization, Solid-State Characterization, and Aqueous Solubilization of Biopharmaceutical Classification System Class II Drugs. *Journal of Pharmaceutical Sciences*.
63. Y. Sun, M. Shtein, S. R. Forrest, Direct patterning of organic light-emitting devices by organic-vapor jet printing. *Applied Physics Letters* **86**, 113504 (2005).
64. U. Han, Y. Seo, J. Hong, Effect of pH on the structure and drug release profiles of layer-by-layer assembled films containing polyelectrolyte, micelles, and graphene oxide. *Scientific Reports* **6**, 24158 (2016).

Chapter 6
Conclusions and Future Work

6.1 Conclusions

This doctoral thesis aspires to optimize OVJP system performance and explore new fields for applications of deposition of small organic molecules from vapor phase.

As was described in **Chapter 1**, OVJP is compact, inexpensive and scalable system with minimal material wastage and extremely high local deposition rates, as opposed to existing high vacuum - based evaporation systems which use shadow masking for patterning. The processing parameters used to control morphology in VTE are usually limited to substrate temperature and rate of deposition of the organics, whereas OVJP has more than six control parameters enabling precise control of deposition rate, deposit shape, structure and surface morphology. In order to fully map OVJP process parameters and enable prediction of deposited film properties, thermophysical properties of small molecular organic electronic materials were studied (**Chapter 2**). Langmuir relation was applied to analyze the sublimation behavior of small molecular organic compounds, enabling the use of thermogravimetry as a rapid, simple, and reliable method for estimating the vapor pressure and the sublimation enthalpy of small molecular organic compounds. The obtained data, and the general testing approach are useful in designing deposition apparatus and developing new vapor-based deposition processes. The strong

correlation between evaporation parameters and crystal density enables estimation of properties of new materials or those that have not been fully characterized (*1*).

Chapter 3 was dedicated to study the trade-offs in OVJP and GF-OVJP systems and possible routes to circumvent them. Effects of deposition duration, system geometry, carrier and guard flow gas types and rates on deposits shape, spread and materials utilization efficiency was demonstrated. For instance, increasing the guard flow rate doubles the deposition rate, focusing the diverging organic molecules onto the substrate, but also introducing turbulence at the perimeter of the deposit. The strongest focusing is observed for CO_2 as guard flow gas, due to its both highest molecular weight and larger collision cross-section compared to Ar and N_2. Full simulation of OVJP and GF-OVJP setup was built in order to further optimize system parameters. Microns-scale resolution was demonstrated by miniaturizing system size and introducing exhaust OVJP with curved nozzle geometry (*2*).

In **Chapter 4** growth of films in OVJP was studied. New spheroidal crystalline ("lobe"-like) microstructures comprised of small organic molecules were discovered, with controllable and scalable sizes (100 nm - 1 μm). A model was developed for surface evolution that can be applied for the prediction and quantitative understanding of small molecular-based film morphologies obtained via different growth techniques and conditions (*3*).

In **Chapter 5** new approach to enhance bioavailability and dissolution rate of small molecular pharmaceuticals via deposition from vapor phase was demonstrated. By using OVJP as a tool, six different pure small molecular medicines were deposited onto different medical grade surfaces in a form of continuous nanostructured crystalline films. Controlled drug release rate and ultra-accurate dosage of pure film form pharmaceuticals were shown, providing enhanced bioavailability to poorly soluble cancer treatment drugs. The approach for small molecular

pharmaceutical deposition from vapor phase was demonstrated for a first time and opens a pathway to new era of research, development and manufacturing of small molecular pharmaceuticals. (*4*)

6.2 Future directions

OVJP technique and it's underlying principle of carrying the organic molecule in a controllable manner to specific site and without use of liquid solvents can potentially be beneficial in many fields where small organic molecules are used. In this paragraph a number of possible OVJP system uses will be demonstrated.

6.2.1 Control of bulk and interfacial morphologies in organic electronic devices

Zimmerman et al. (*5*) have demonstrated use of solvent vapor annealing to independently control the interface and bulk thin-film morphologies, thereby modifying charge transport and exciton dissociation in these structures. Annealing of diphenyl-functionalized squaraine (DPSQ)/C60 following to C60 deposition locked in interface disorder found in unannealed junctions while improving order in the thin-film bulk. This resulted in an increase in short circuit current by >30% while maintaining the open circuit voltage of the as-cast heterojunction device. In other words, order in a film bulk provides improvement of exciton and charge transport, while disorder at the interface decreases the parasitic polaron- pair recombination rate at the donor- acceptor (D-A) interface of organic photovoltaic cell. Using same principle, combination of OVJP and VTE processes can be used to deposit controlled crystallinity bulk films combined with amorphous structures at the interface, as shown in **Fig. 6.1**. Here the bulk SubPc donor layer is first

deposited with OVJP or OVPD, followed by deposition of thin (1-3 nm) interface layer with VTE.

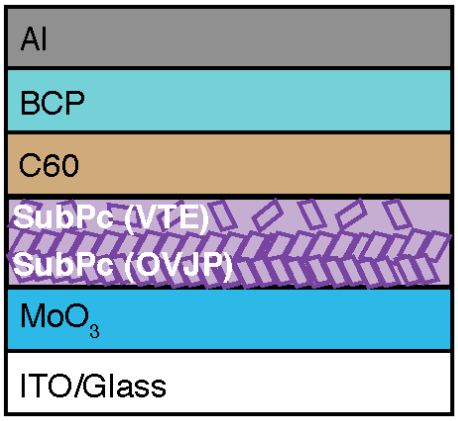

Figure 6-1 Example for controlled morphology via combined VTE and OVJP deposition
Example of organic photovoltaic cell with mixed SubPc donor layer. Bulk film is printed with OVJP (or OVPD) process to achieve crystallinity and interface is deposited with VTE process to achieve amorphous structure.

6.2.2 OVJP for rapid dissolution of small molecular compounds in fluids

Solutions of small molecular organic compounds are used extensively in many industries: food, cosmetics / perfume, pharmaceuticals, organic electronics, printing and paints. To achieve a given concentration of organic solute in original powder form, the required amount of powder is immersed directly in the solvent and being dissolved until all powder particles are separated into solvated molecules (as described in **Chapter 1**). This process is especially challenging for low solubility substances with high crystal energy, where dissolution rate is very slow. To enhance dissolution rates, powder particle size is reduced (via milling or other methods), and solution is usually heated. This approach can be time- and energy- consuming, as well as potentially damaging to the solvent. An additional drawback of direct immersion of powder solute in the solvent is when the actual needed concentration of a compound or solution volume is very low. For instance, if needed concentration is on the order of micromolar, and needed volume is 10 ml,

the needed weight of 200 gr/mole material would be on the order of micrograms. This weight is not feasible to measure accurately for a precursor powder, therefore higher concentration of solution is made with subsequent dilution with additional amount of solvent. This process is undesirable from both economical and safety standpoint (when dealing with organic solvent).

By using OVJP, evaporated molecules can be jetted directly into a fluid with highly controlled deposition rate, and consequently accurate, sub-micromolar concentration. In such setup, molecule removal from the crystal lattice (discussed in **Chapter 5)** occurs at evaporation stage, resulting in lower energy needed for dissolution. An example of fluorescein (Mw 332 gr/mole) jetted into phosphate buffer saline (PBS) solution with micromolar concentrations is shown in **Fig. 6-2**.

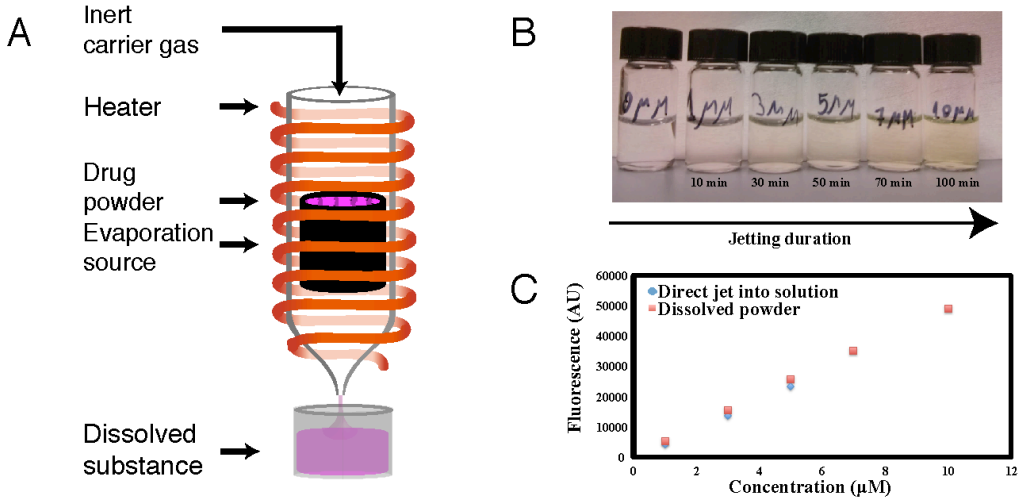

Figure 6-2 OVJP for direct dissolution in fluids
(A) Schematic of rapid dissolution system. (B), (C). Example of fluorescein jetted into phosphate buffer saline solution of 2ml. Jetting conditions: Carrier gas: nitrogen. Carrier gas flow rate: 200 sccm. Source temperature: 300°C, substrate temperature: 20°C, nozzle tip inner diameter: 0.5 mm, nozzle tip-liquid surface separation distance: 20 mm. The concentration was varied via jetting duration. Concentration was measured by fluorescence spectroscopy calibrated with dissolved fluorescein powder.

6.2.3 Reaction assisted OVJP

The concept of reactive vapor phase deposition was demonstrated by Biswas et al. (*6*) for deposition of passivating parylene films in ambient air atmosphere. Vaporization and pyrolysis of the *di-p-xylylene* (parylene dimer) occurred in a single compact nozzle, producing a jet of monomer that polymerizes into a film upon contact with the substrate at room temperature. This approach can be utilized further, enabling reaction of evaporating precursors while travelling through the nozzle. Iron pyrite (FeS_2) films, for instance, largely used in battery and solar applications, can be patterned onto substrates by reaction of precursors Tris(acetylacetonato) iron(III) ($Fe(acac)_3$) and tert-butyl disulfide (TBDS) and using argon or helium as carrier gases (7). Another example is deposition of metals, where evaporating precursor agent, such as metal halide can be jetted onto heated substrate to produce pure metal coating. Using reactive carrier gases (such as nitrogen) same approach can be used to obtain ceramic coatings.

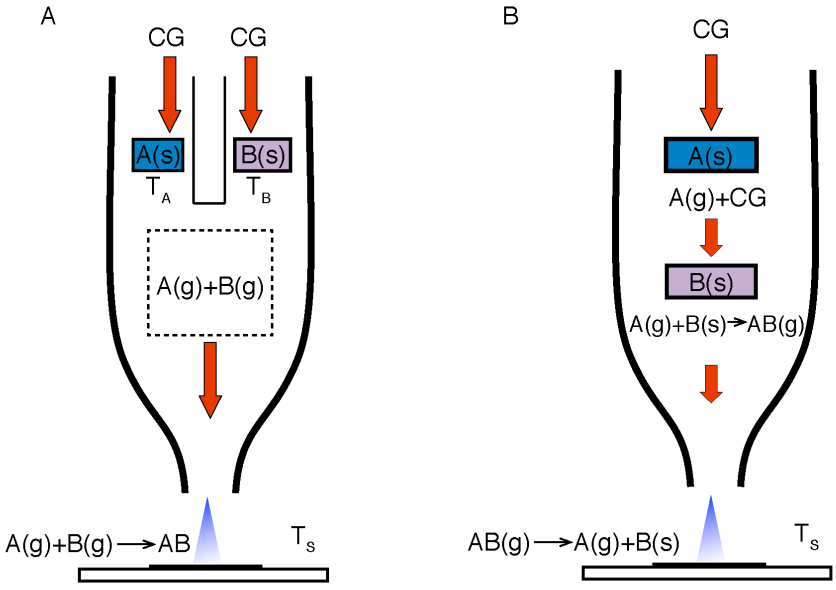

Figure 6-3 Various modes of reaction assisted vapor jet deposition
(A)Reacting precursors are evaporated and react on the substrate surface (for instance $Fe(acac)_3$ +TBDS to form FeS_2) (B) Example for metal coatings setup - evaporating

halide (A) and metal substance (B) reacting to form volatile metal halide AB. Upon reaching the substrate halide decomposes back into solid metal and volatile halide.

6.2.4 Co-crystallization and in-situ crystal growth studies of pharmaceuticals

As discussed in **Chapter 5** solubility is affected by crystal lattice energy. One of the recently developed techniques to solid-solid interactions modification is co-crystallization (*8*). Co-crystals contain two or more molecules arranged in a new crystal form with properties often superior to those of each of the separate entities (**Fig. 6-4**).

Co-crystals are also attractive to pharmaceutical scientists because they can substantially increase the number of crystal forms that exist for a particular active pharmaceutical ingredient (API), and might improve physical properties of clinical relevance. Cocrystal approach especially used to enhance the specific properties of pharmaceutical solids such as dissolution rate of poorly water soluble API and the physical stability of moisture liable APIs.

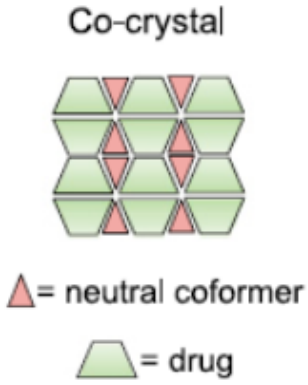

Figure 6-4 Schematic diagram of cocrystal (*9*)
Cocrystals consist of drug and a cocrystal former (coformer), which interact primarily via hydrogen bonds

Common co-crystallization techniques usually involve predissolution of substances, followed by mixing and solvent evaporation. Co-crystallization from vapor phase has not been done yet and can enable controlled crystallization of two or more substances in a controlled manner. Since OVJP was demonstrated to obtain highly nano-crystalline films, due to molecular kinetics, this tool can potentially produce fine cocrystals of different small molecular pharmaceuticals. In this case the system would be similar to the one in **Fig. 6-3a**, potentially with additional carrier gas for dilution. The system would first be calibrated to obtain drug/coformer needed stoichiometric ratio. The mixture would be deposited on a substrate with controlled temperature. Due to high surface mobility the molecules can potentially be cocrystallized upon arrival to the substrate surface.

Further studies of OVJP applications to pharmaceuticals will include effects of deposition conditions on crystal size and degree of crystallinity, *in-situ* crystallization studies during nucleation and growth of medicinal compounds.

Animal model studies to learn how deposited films interact with different biological tissues (skin, eyes, etc.) will provide a full picture of printed nanostructured crystalline films applications to pharmaceuticals and cosmetics.

6.3 Summary

The versatility of OVJP technique with its wide range of independently controllable processing parameters makes it uniquely suited not only for semiconductor material deposition, but also for a variety of applications in pharmaceutical, cosmetics, food, color and other industries. The tool can be scaled up to have multiple nozzles in an array for fabricating multilayered structure of different known materials, or large area deposits of a single materials, as well as performing rapid, combinatorial studies of new materials.

This thesis is a start of a new era for OVJP and related vapor phase deposition techniques.

6.4 References

1. O. Shalev, M. Shtein, Effect of crystal density on sublimation properties of molecular organic semiconductors. *Organic Electronics* **14**, 94 (2013).
2. S. Forrest, M. Shtein, O. Shalev, S. Biswas, Guard Flow OVJP Implementation, Patent, US Appln: 62/011,785 (2014).
3. O. Shalev *et al*., Growth and modelling of spherical crystalline morphologies of molecular materials. *Nature Communications* **5**, (2014).
4. O. Shalev *et al*., Novel Approach to Small Molecular Medicines Printing Using Deposition from Vapor Phase. *In Preparation*, (2016).
5. J. D. Zimmerman *et al*., Independent Control of Bulk and Interfacial Morphologies of Small Molecular Weight Organic Heterojunction Solar Cells. *Nano Letters* **12**, 4366 (2012).
6. S. Biswas, O. Shalev, K. P. Pipe, M. Shtein, Chemical Vapor Jet Deposition of Parylene Polymer Films in Air. *Macromolecules* **48**, 5550 (2015).
7. N. Berry *et al*., Atmospheric-Pressure Chemical Vapor Deposition of Iron Pyrite Thin Films. *Advanced Energy Materials* **2**, 1124 (2012).
8. R. V. Prasad *et al*., Pharmaceutical cocrystallization: a review. *Int J Pharm Chem Sci* **1**, 725 (2012).
9. H. D. Williams *et al*., Strategies to Address Low Drug Solubility in Discovery and Development. *Pharmacological Reviews* **65**, 315 (2013).